

UCLA

UCLA Electronic Theses and Dissertations

Title

Novel Hydrostatic Fluid Power Actuators

Permalink

<https://escholarship.org/uc/item/1fm496hv>

Author

Simonelli, James Michael

Publication Date

2017

Peer reviewed|Thesis/dissertation

UNIVERSITY OF CALIFORNIA
Los Angeles

Novel Hydrostatic Fluid Power Actuators

A dissertation submitted in partial satisfaction
of the requirements for the degree
Doctor of Philosophy in Aerospace Engineering

by

James Michael Simonelli

2017

© Copyright by
James Michael Simonelli
2017

ABSTRACT OF THE DISSERTATION

Novel Hydrostatic Fluid Power Actuators

by

James Michael Simonelli

Doctor of Philosophy in Aerospace Engineering

University of California, Los Angeles, 2017

Professor Tsu-Chin Tsao, Chair

Hydrostatic fluid power actuators are versatile tools that have wide and varied applications to real-world engineering problems. Their high stiffness, haptic feedback, and force/displacement scaling can be harnessed to solve issues other actuators struggle with. This research presents the creation of two novel actuators and their applications: a piezo-hydraulic fast tool servo (FTS) and a Magnetic Resonance (MR) compatible actuator for remote robotic interventions. The FTS device, featuring motion amplification of the piezoelectric displacement, was designed and modeled, then fabricated and controlled to track a non-circular engine piston profile by Iterative Learning Control and Repetitive Control. The actuators for the MR robotic system—featuring back-drivable motion and force transmission over a significant distance—are designed, fabricated, and characterized to show many desirable properties. These actuators are the basis for a 1DOF stage for the emulation of respiratory motion in-bore, which was characterized, controlled, and shown to track recorded motion with acceptable error. These actuators were then used to realize co-robotic control of a 1DOF manipulator, demonstrating multiple modes of collaboration. Finally, a master-slave pair comprised part of a hardware-in-the-loop simulation of closed-loop control under MR image feedback using adaptive control. Results were analyzed to provide recommendations for a time when the full system, complete with image feedback, can be assembled.

The dissertation of James Michael Simonelli is approved.

Holden Wu

Robert M'Closkey

Steven Gibson

Tsu-Chin Tsao, Committee Chair

University of California, Los Angeles

2017

TABLE OF CONTENTS

1	Introduction	1
I	Piezohydraulic Fast-Tool Servo	5
2	Introduction to the Fast Tool Servo Application	6
2.1	Previous Works	7
3	Design & Fabrication of a Piezohydraulic Fast Tool Servo	9
4	Modeling of a Piezohydraulic Fast Tool Servo	15
5	Verification of the Completed Device	20
5.1	Lumped Model Verification	22
6	System Identification and Control of a Piezohydraulic FTS	26
6.1	System Description	26
6.2	System Identification and Controller Description	27
6.2.1	LQGi Design	29
6.2.2	ILC Design	31
6.2.3	Repetitive Controller Design	32
6.3	Experimental Results and Analysis	33
7	Conclusions	40
II	MR-Compatible Fluid Actuators for Robotic Interventions	41

8	Introduction to MR Robotics	42
	8.0.1 Previous Work	45
9	Design of MR-compatible Linear Actuators	50
	9.1 Diaphragm Design	50
	9.2 Single-Acting Diaphragm Actuator	51
	9.3 Double-Acting Diaphragm Actuator, First Iteration	54
	9.4 Double-Acting Diaphragm Actuator, Second Iteration	58
10	Application: An MR-Compatible Stage for Respiratory Motion Emulation	66
	10.1 Introduction	66
	10.2 System Design	68
	10.2.1 Slave Side— Phantom Platform	69
	10.2.2 Master Side	71
	10.3 Experimental Setup and Control Implementation	72
	10.3.1 Experimental Setup	73
	10.3.2 Control Implementation	74
	10.4 Experimental Results	76
	10.4.1 Actuator and System Verification	76
	10.4.2 Tracking Results	76
	10.5 Conclusions	84
11	Fluid Networks and Control	85
	11.1 Fluid Network Theory	85
	11.2 Fluid Network Demonstration	88
	11.3 Fully-Autonomous Robotic Operation	90

11.3.1	Controller Design	92
11.3.2	Adaptive Controller Characterization	94
12	Conclusions and Recommendations	105
	References	107

LIST OF FIGURES

1.1	Basic Types of Hydraulic Actuators	2
2.1	A Brief Survey of Relevant Literature	7
3.1	Amplifier Device Section View	9
3.2	Amplifier Device Exploded View	10
3.3	Metal Diaphragm Schematic	11
3.4	Deflection of Rear Diaphragm: With and Without Spreader	13
4.1	System Schematic	15
5.1	Structured System ID Results [Volts to mm]	21
5.2	Static Stiffness Results	23
5.3	Experimental Response from Cutting Force to Displacement	23
5.4	System Diagram (Verification Model)	24
5.5	Frequency Response When Displaying Early Resonance	25
6.1	System Diagram, Experimental Setup	26
6.2	Fast Tool Servo Experimental Setup Photo	27
6.3	Sine Sweep Results, Open Loop Plant [Volts to Volts]	28
6.4	Experimental Results, Dead Zone	29
6.5	Target Piston Profile	30
6.6	ILC Controller Structure	31
6.7	Block Diagram, Proposed Controller	32
6.8	Multiplicative Uncertainty Model	32
6.9	Sensitivity Analysis	34

6.10	Robust Stability Analysis	34
6.11	Experimental Results: LQGi Inner Loop Only	35
6.12	Experimental Results: LQGi + Repetitive Control	36
6.13	Experimental Results: LQGi + ILC	37
6.14	Experimental Results: LQGi Inner Loop + ILC + Repetitive	38
6.15	Experimental Results: Error Spectrum	39
8.1	MR Robotics System Schematic	44
8.2	MR Robotics, First Iteration Tracking Results [Yas14]	46
8.3	MR Robotics, First Iteration Comparison to Model [Yas14]	46
8.4	MR Robotics, First Iteration	47
8.5	Glass Syringe Prototype	48
9.1	Custom Diaphragms and Tooling	51
9.2	Single-Acting Diaphragm Actuator Design, Section	52
9.3	Single-Acting Diaphragm Actuator, as Manufactured	52
9.4	Stiffness Experiment Results, Single-acting Actuator	53
9.5	Double-Acting Diaphragm Actuator Design—First Iteration, Section	54
9.6	Double-Acting Diaphragm Actuator Design—First Iteration, as Manufactured	55
9.7	Stiffness Experiment Results, Double-Acting Diaphragm Actuator—First Iteration	56
9.8	Failure Mode of Custom Reinforced Diaphragms	56
9.9	Input-Output Displacement, Double-Acting Diaphragm Actuator—First Iteration	57
9.10	Double-Acting Diaphragm Actuator Design—Second Iteration, Section	58
9.11	Double-Acting Diaphragm Actuator Design—Second Iteration, as Manufactured	59

9.12 Characterization Experimental Setup	60
9.13 Stiffness Experiment Results, Double-Acting Diaphragm Actuator—Second Iteration	61
9.14 Input-Output Displacement, Double-Acting Diaphragm Actuator—Second It- eration	62
9.15 Hysteresis Loop, Double-Acting Diaphragm Actuator—Second Iteration . . .	63
9.16 Input-Output Delay Estimate, Double-Acting Diaphragm Actuator—Second Iteration	64
9.17 Force Transmission, Double-Acting Diaphragm Actuator—Second Iteration .	65
10.1 System Schematic	69
10.2 System participating in a Needle Targeting Experiment	70
10.3 Bolt-on Mechanical Amplifier	71
10.4 Master Unit Design Schematic	72
10.5 Sample Abdominal MR Image for Tracking	73
10.6 Tracking Experimental Setup	73
10.7 Feed-Forward Controller Structure	74
10.8 ILC Controller Structure	75
10.9 MR-compatibility of Bore-side System	77
10.10 Master-side PI tracking Results	78
10.11 Feed-forward Inversion Tracking Results	79
10.12 Inversion-based ILC Tracking Results	80
10.13 ILC Convergence Plot	80
10.14 Additional Profiles Tracked	81
10.15 Preliminary ILC Results for Amplified System	83

11.1 Fluid Network Concept	86
11.2 Motion Scaling Experimental Results	89
11.3 Frequency Crossover Experimental Results	89
11.4 Virtual Wall Experimental Results	90
11.5 Example Recorded Breathing Trajectory	91
11.6 Adaptive Feed-Forward Controller Structure	92
11.7 Adaptive Feedback Controller Structure	93
11.8 Adaptive Feedback/Feedforward Controller Structure	94
11.9 Experimental Setup, Closed-Loop Control Experiments	95
11.10 Robotic Manipulator System Identification	96
11.11 Effect of Filter Order on Feedforward Controller Performance	97
11.12 Effect of Filter Order on Feedback Controller Performance	98
11.13 Effect of Filter Order on Combined Controller Performance	99
11.14 Benchtop Tracking Results	100
11.15 Benchtop Tracking Error Spectrum	100
11.16 Benchtop Experiment Summary: Quantization	102
11.17 Benchtop Experiment Summary: Delay	103
11.18 Benchtop Experiment Summary: Sampling Rate	103

LIST OF TABLES

4.1	List of Symbols	19
5.1	Comparison of Selected Parameters in White-box and Grey-box Models . . .	22
6.1	Summary of Control Results	39
10.1	MR-compatibility of Finished System	82
10.2	Summary of Control Results	82

ACKNOWLEDGMENTS

I would first like to thank my advisor, Professor T-C Tsao, for his patience and guidance, and for always pushing me to do better. He took in a guy who came into his office babbling about machines and turned me into a well-rounded engineer, and for that I am very grateful. I'd also like to thank my committee, Professors Steve Gibson, Robert M'Closkey, and Holden Wu for your guidance, support, and great ideas. I would also like to thank the MR Research Labs for providing me with a great application and even greater collaborators.

To everyone in the lab, who put up with my nonsense and somehow managed to make the basement of Boelter into somewhere I could look forward to coming to, thank you; I don't know that I would have made it if you were jerks. To Stephen, thank you for teaching me the finer points of building plants and being the "plant guy." To Chris, thanks for your advice, friendship, and late-night antics. To Sandeep, thank you for sharing your knowledge (and controllers) with me, and for always keeping me honest. To Martin, who has the (mis)fortune of inheriting my project, I can think of no better hands to leave it in. To Miguel, Ben, and everyone in the Shops—thank you for your expertise and your willingness to drop whatever you were doing to help me. I can confidently say that this work would be vastly inferior but for your help, so thank you.

To my friends, who were a constant source of support, encouragement, and things to do instead of my research, thank you. To Diana, for being patient with the long hours and the times that I smelled strongly of machinery, and for your unwavering faith in me, I am forever grateful.

Finally, I would like to thank my family, for inspiring and encouraging me at every turn, and most especially my parents, for thirty years of believing wholeheartedly that I could do anything—and making sure that I knew it—I appreciate it far more than you can know.

VITA

- 2009 B.S. (Mechanical Engineering), University of California, Irvine,
Irvine, CA.
- 2009 B.S. (Aerospace Engineering), University of California, Irvine,
Irvine, CA.
- 2011 M.S. (Aerospace Engineering), University of California, Los An-
geles (UCLA), Los Angeles, CA.
- 2009-2017 Teaching Assistant, Mechanical and Aerospace Engineering De-
partment, University of California, Los Angeles (UCLA), Los
Angeles, CA
- 2015-2017 Graduate Student Researcher, Mechanical and Aerospace En-
gineering Department, University of California, Los Angeles
(UCLA), Los Angeles, CA

CHAPTER 1

Introduction

Fluid Actuators harness desirable properties of a working fluid to transmit or amplify motion and force across distances great and small. They can serve a variety of useful engineering purposes, such as providing force or displacement scaling by mismatched input and output effective areas, or transmitting motion and force over a distance without the use of electricity, magnetism, or complicated mechanisms, all while giving transparent haptic feedback to the operator.

Linear fluid actuators fall into one of two categories, illustrated in Figure 1.1: Single-Acting and Double-Acting. In Single-Acting actuators, the fluid can build intense pressure in the direction of expanding the output cylinder, but can only generate a pressure differential of one atmosphere in the other direction without the help of a return spring. Double-Acting actuators solve this issue by making the pressure differential be between two hydraulic lines, which can be preloaded to pressures limited only by the cylinder and hose materials, instead of a hydraulic line and the ambient air. Double-Acting designs tend to be more linear and symmetric in their push-pull operation, and offer better haptic feedback potential (due to their lack of a preload spring), but are typically bulkier than their Single-Acting counterparts. Hydrostatic actuators specifically involve no pumps or valves, which does not interrupt the fluid flow, generally providing a more linear input-output relation.

Fluid actuators can be combined into a fluid network to seamlessly blend inputs at the hardware level and thus enable collaborative control of an output actuator between several general input units, which can be controlled completely manually, completely autonomously, or some combination thereof. This hardware blending can also provide for displacement and force modulation across master units. Whereas most electromagnetic actuators are com-

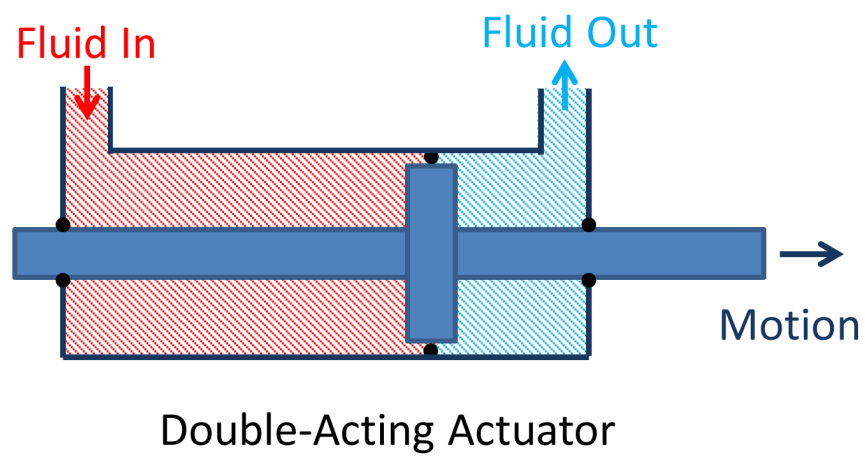
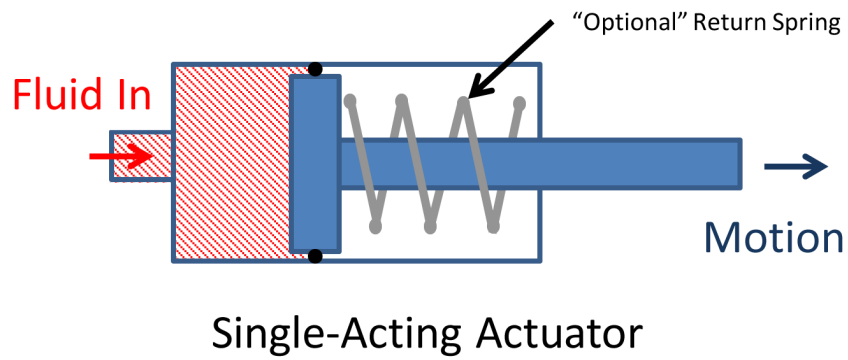


Figure 1.1: Basic Types of Hydraulic Actuators

prised of similar materials, fluid actuators allow the designer to customize the material of the actuator and the fluid to each specific application, which is useful in applications where metals, electricity, or magnetic fields can be detrimental. Fluid actuators also present their own challenges that traditional actuators do not, however. Fluid leakage is an additional failure mode that must be accounted for, and force asymmetry between push and pull directions can be an issue. Transmission line effects can introduce additional dynamics over the lines, and care must be taken in designing actuators to minimize friction, especially when haptic feedback is a design goal. Despite these additional challenges, fluid actuators can be invaluable in the right application.

In this work, Fluid Actuators will be applied to two applications: a Fast Tool Servo for precision turning of eccentric profiles, and toward a strictly MR-compatible robotic system for remote target tracking, with an emphasis on liver biopsy. The Fast Tool Servo device takes advantage of the mechanical advantage offered by mismatched input and output areas to amplify the stroke of a Piezoelectric actuator while maintaining bandwidth, while the MR application makes use of the nonmagnetic, non-electric transmission capabilities to actuate devices within the MR bore with no apparent effect on the imagery obtained while doing so.

The main contributions of this work are the development of several fluid-actuated devices: a piezo-hydraulic Fast Tool Servo, and a family of linear hydrostatic actuators. The Fast Tool Servo system is designed, manufactured, and shown to track a real-world piston profile with similar performance to commercially-available devices. The hydrostatic actuators are leveraged to power a strictly MR-compatible linear stage and a 1DOF robotic system for biopsy needle driving, both of our own design. These systems are demonstrated to accurately reproduce recorded respiratory motion and precisely target even small lesion analogues in gel phantom studies, respectively.

The remainder of this dissertation is organized as follows:

Part I describes the application of Fluid Actuators to the machining application. Chapter 2 introduces the Fast Tool Servo problem and reviews existing work on the subject. Chapter 3 covers the design and fabrication of the Fast Tool Servo device presented herein, and

Chapter 4 discusses the modeling of the device. The performance of the completed device is verified Chapter 5, and System ID and Control results are presented in Chapter 6. Chapter 7 concludes the Fast Tool Servo application.

Part II details the application of Fluid Actuators to the MR robotics application. Chapter 8 introduces the application and summarizes the state of the art. Chapter 9 details the design process and history of the MR-compatible fluid actuators, and Chapter 10 details the application of the developed actuators to construct a 1DOF MR-compatible linear stage for the purpose of respiratory motion emulation. Chapter 11 demonstrates the collaborative hardware blending ability of the fluid network and gives preliminary results toward closed-loop control with an MR image-feedback algorithm. Chapter 12 concludes the MR application and provides recommendations for the project going forward.

Part I

Piezohydraulic Fast-Tool Servo

CHAPTER 2

Introduction to the Fast Tool Servo Application

Fast-tool Servos (FTS) are widely researched and have applications in optical fabrication [TL07], wrist pin boring for internal combustion engines [Cse03], and active chatter suppression [TOM94], to name a few. To go with these many applications, there are several challenges presented by the problem, the greatest of which can be succinctly described as inertia—the challenge lies in designing a device with a tool holder robust enough to cut, but light enough so that the usable bandwidth of the system is acceptable. Bandwidth is extremely important, as FTS are capable of turning or boring general non-circular patterns, but to do so, must move the tool through a repeating sequence whose frequency is twice the spindle speed and amplitude is the total runout of the finished pattern. This sets a lower bound on both the stroke of the actuator and its bandwidth, and owing to their importance, these two criteria will be used extensively in comparing FTS designs.

Fast-tool Servo designs can be loosely broken down in to two categories: those that attach a tool to an actuator at its rated stroke, and those who attempt to amplify the stroke of an actuator through another subsystem. In general, the former category tends to be devices based on piezoelectronic transducers (PZT), which have extremely high bandwidth, but stroke in the dozens of microns; few devices from the former category leave the micron-range stroke band. Conversely, the latter category is more varied in both composition and performance—the only unifying factor to be found is that nearly all of these devices employ either a leverage- or rotation-based amplification scheme, which are both susceptible to Abbe error as the displacement of the tip is almost always inferred from the either a measured angle or a measured displacement closer to the center of rotation.

This work consists of a novel FTS design based on a $60\mu m$ -stroke PZT coupled to a

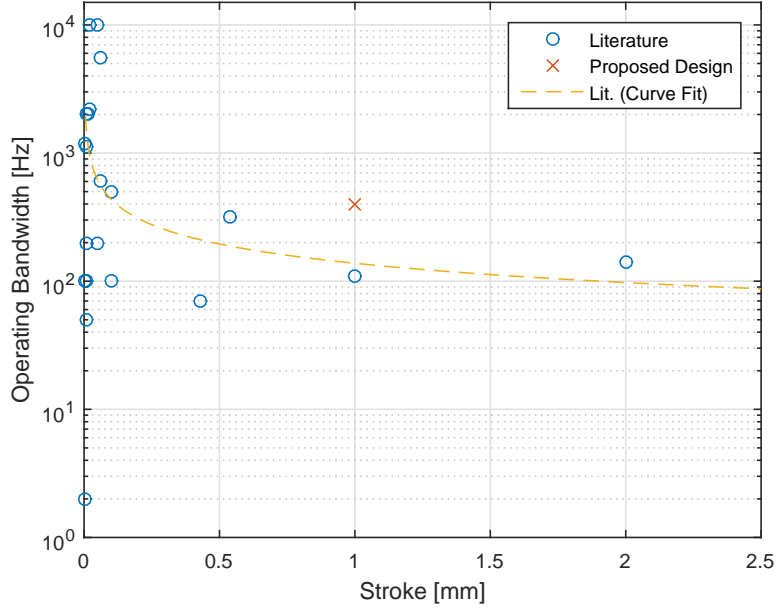


Figure 2.1: A Brief Survey of Relevant Literature

hydraulic amplification scheme whose design stroke and bandwidth are 1mm and 400Hz, respectively. Advantages of this design include axial amplification which reduces susceptibility to Abbe error, compact amplifier design, and high bandwidth-to-stroke ratio, as shown in Figure 2.1. This figure is a comparison of achieved bandwidth and stroke across surveyed literature; the grouping to the far left are devices that do not attempt to amplify their actuator's stroke.

The remainder of this section is presented as follows: Chapter 2 continues and summarizes the state of the field. Chapter 3 discusses the design and manufacturing of the stroke amplifier device. Chapter 4 covers the white-box modeling of the assembled system. Chapter 5 describes the model verification process and addresses validity of the white-box model. Chapter 7 will summarize the results and examine future directions.

2.1 Previous Works

The current literature can be broadly classified into four basic categories, mechanically speaking: direct drive, where the tooltip is directly attached to the driving actuator; axial flexures,

which encompasses compliant mechanisms and metal diaphragms that only add stiffness or constrain the motion of the tooltip without attempting to amplify the stroke of the driving actuator; leverage-based flexures, which attempt to amplify the driving actuator's stroke by applying force closer to the flexure's joint than the tooltip mounting location; and true rotary designs whose driving actuator imparts not a linear force but a torque to the system.

The variation seen in the mechanical setup cannot be seen in the choice of driving actuator, which are almost exclusively PZTs. Their high bandwidth and force potential are ideal for FTS applications, but in many cases, something must be done to compensate for their stroke, which is typically in the dozens of microns. It should be noted that not all of the work reviewed here attempts to amplify the actuator's stroke; some applications require less than a hundred microns of peak-to-peak travel.

Crudele, et al. developed a direct-drive FTS based on a PZT to improve surface finish quality in diamond-turning applications [CK03]. It achieved 60 microns of stroke at 5.5kHz working bandwidth, sufficient for its goal of surface finish improvement. Model-based direct digital control design was contrasted with Zero Phase Error Tracking Control (ZPETC) with Repetitive Control, finding that Repetitive Control improved surface finish over the direct design method. Cuttino, et al. developed a direct-drive FTS which was also based on a PZT, but whose goal was to turn asymmetric surfaces on a diamond-turning machine [CMS99]. Their design achieved 100 microns at 100Hz bandwidth. Simple PID control was used for tracking, but a nonlinear hysteresis compensator gain was used to minimize hysteretic inaccuracies.

CHAPTER 3

Design & Fabrication of a Piezohydraulic Fast Tool Servo

A sectioned view of the amplifier is given in Figure 3.1, which will be referred to throughout this section.

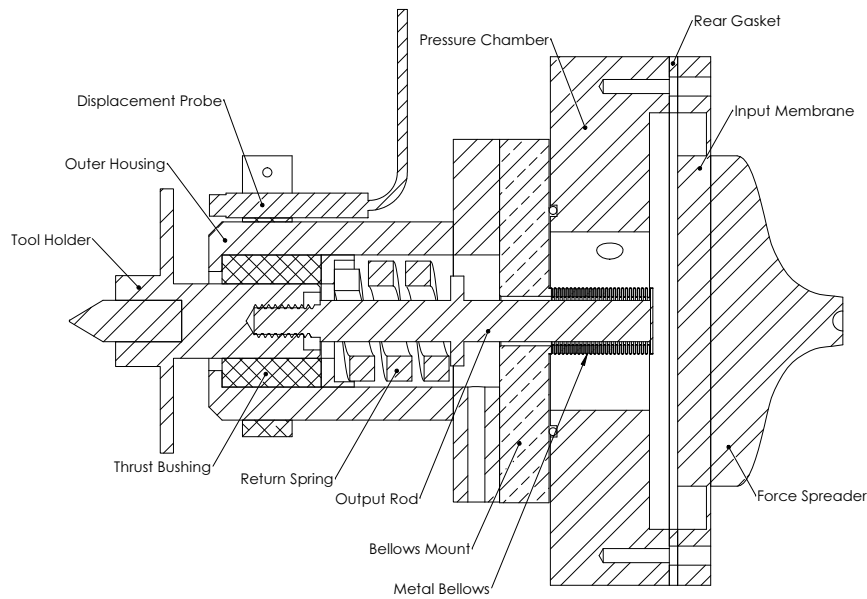


Figure 3.1: Amplifier Device Section View

The primary design considerations for the stroke amplifier were: an amplification ratio of at least 17 (to amplify the 60-micron PZT stroke to 1 mm), a bandwidth of 400Hz, compact packaging, and that the amplified output be axial with respect to the input. Owing to the high amplification requirement combined with compactness, a hydrostatic amplifier design

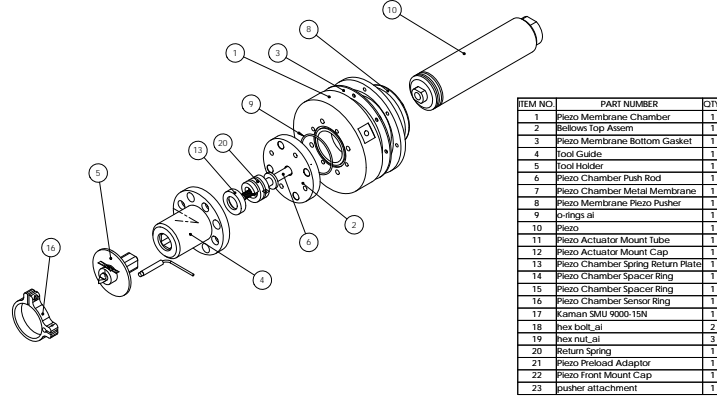


Figure 3.2: Amplifier Device Exploded View

was chosen. Whereas leverage- and rotation-based designs amplify linearly with their length dimension, a hydrostatic device's amplification ratio is that of the *area* of the input plate to the area of the output plate, which scales with l^2 . One consideration with a hydrostatic design is the stiffness of the working fluid, which is given by

$$k_{fluid} = \frac{B}{V_0}$$

where B is the bulk modulus of the fluid and V_0 is the volume of fluid at rest. As the hydraulic oil's bulk modulus is quite high, and the working volume of fluid is in the range of a few cubic centimeters, this is not a concern; the fluid is in actuality the stiffest "component" in the amplifier.

The issue turns to sealing the fluid, whose pressure will exceed 300 psi during normal operation, while allowing the output side to move in excess of 1 mm. To accomplish this, the output side was fitted with a metal bellows to allow for large stroke without the need for an o-ring/piston design and the friction that accompanies it. To minimize stroke lost to bulging of the bellows, it was mounted inverted in the fluid and the output rod diameter was set at the inside diameter of the bellows to resist inward deflection. The bellows was then welded to a brass plate for mounting, which was bolted to the pressure chamber and sealed with an o-ring.

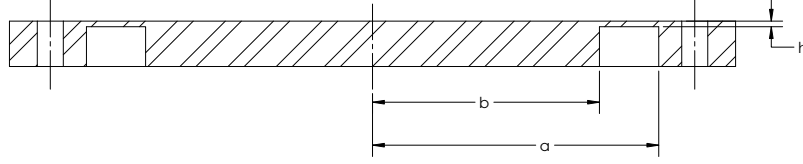


Figure 3.3: Metal Diaphragm Schematic

The input side required far less stroke capability, so a metal diaphragm was chosen for its ease of sealing and lack of moving parts. We used a flat diaphragm design for convenience of manufacture and modeling. The diaphragm was designed so that its stiffness kept its natural frequency (both with and without the lumped mass of the force spreader) well outside the target operating bandwidth, but was also soft enough to be well below the stiffness of the PZT— the PZT, while forceful, does have a practical limit to its output force. The major design equations, derived from work in [Di 82], are given in Equations 3.1 and 3.2, where E is Young’s Modulus, μ is Poisson’s Ratio, and a , b , and h are as depicted in Figure 3.3. To seal the rear of the device, a custom laser-cut gasket was made, and the diaphragm — as with all components in contact with the working fluid (except the brass bellows mount) — was made of AISI 316L Stainless Steel for strength and corrosion resistance.

$$k_d = \frac{\pi E b^2 h^3}{A_p a^4} \quad (3.1)$$

$$A_p = 3 \left(\frac{1 - \mu^2}{16} \right) \left(1 - \left(\frac{b}{a} \right)^4 - 4 \left(\frac{b}{a} \right)^2 \log \left(\frac{a}{b} \right) \right) \quad (3.2)$$

The device was designed so that the sealed chamber would be an atomic unit, and the seal would not need to be broken during normal disassembly. This was done due to the absolute necessity of a proper seal, both to resist outflow of fluid and to resist inflow of air, and the relative difficulty of achieving a proper seal and an acceptable level of entrained air. As this is a pumpless system, removal of entrained air was especially difficult. Due to the low hydraulic oil volume, even small amounts of air had a marked effect on the bulk modulus of the fluid, cutting the achieved bandwidth in half in the early stages of development.

With this issue in mind, a system to fill the device with a minimum of entrained air was

designed separately to be removed after filling. A single fill port/pressure tap was included in the pressure chamber, and a separate vacuum chamber was attached upstream of a valve. Through this, we were able to ensure an acceptably-degassed fluid through the following process: First, we pull vacuum on the pressure chamber and close the valve. We then fill the second chamber with hydraulic fluid and pull vacuum on that as well, bleeding the entrained air out of the fluid. This second chamber is then sealed and the valve between the chambers is opened, hard-filling the (previously evacuated) main chamber with degassed fluid. This process was key to achieving the quoted bulk modulus of the hydraulic fluid, and the resulting dynamic stiffness thereof.

In an effort to prevent any bending moment in the PZT and to avoid mounting parts directly to the bellows, all components (other than the atomic chamber unit) were held together with a preload force. This also served as a way to keep the chamber pressure positive at all times and ensure that all parts stay together during operation. Further discussion and validation of this assumption may be found in Section 5.

A downside of hydraulic systems is that they have a directional asymmetry in the amount of force they can provide— in the extension direction, the system can provide 300 psi of pressure (multiplied by the area of the output plate to obtain force), but in the retraction direction, even a full vacuum can only provide 15 psi of suction. Even if that was forceful enough to retract the tool at the design frequency (and it is not), vacuum is undesirable as it would introduce cavitation in the fluid. Thus, we must add a stiff enough return spring to provide appropriate retraction force to track higher frequencies, but how do we define “stiff enough?”

Since the tool holder assembly (tool holder, output rod, and return spring are not rigidly connected to the bellows, it is meaningful to consider the natural frequency of the subsystem alone. To find a “stiff enough” return spring, we choose a spring such that the natural frequency of the return spring/tool holder moving mass subsystem is outside the desired total system bandwidth. This ensures two things: first, since the subsystem is a second-order oscillator, the response should be flat out to the resonant peak which ensures that the spring will provide enough force to return the tool out to that frequency; and second, the

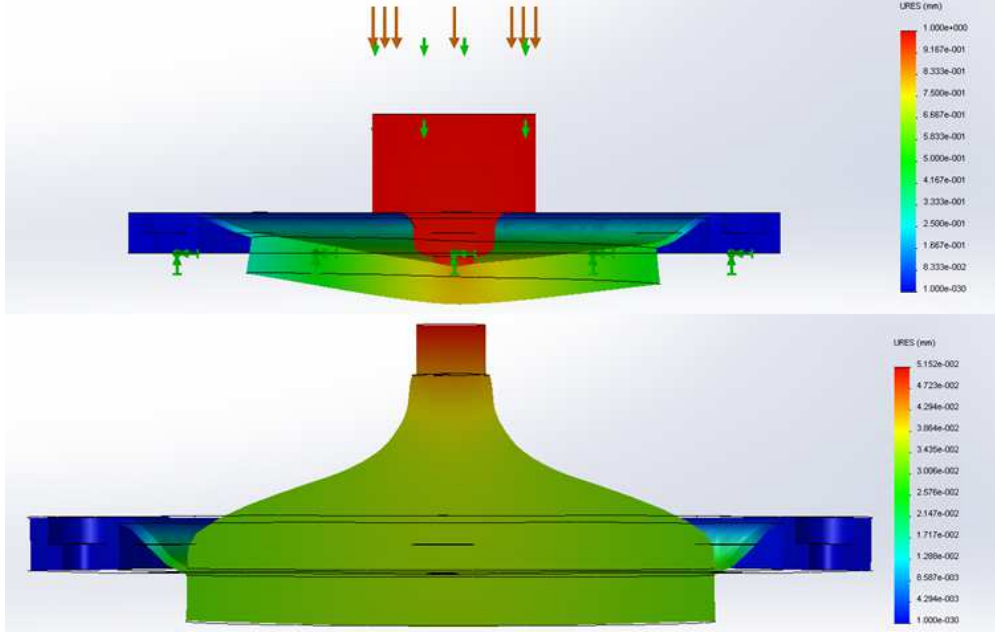


Figure 3.4: Deflection of Rear Diaphragm: With and Without Spreader

most likely frequency we expect separation between the two subsystems to occur at is the natural frequency of the tool holder system, so placing it outside the usable band obviates that as well. This is stated without proof here, but should be relatively intuitive and is again further treated in Section 5.

Finite-element studies showed that the PZT alone would produce an unacceptably nonuniform displacement of the input diaphragm (Figure 3.4) which would detract from the potential stroke achieved, so a force spreader was designed to interface between the PZT and the diaphragm. Minimizing the moving mass was important to keeping the parts preloaded together at high frequency, so the final design was conceived to shave mass from the PZT side of the spreader while maintaining uniform deflection of the diaphragm.

The two preload forces can mechanically be set independently, though careful inspection of the model shows that at steady state, they must be related by the amplification ratio. The purpose of allowing them to be semi-independently set is to control the static extension/compression of the bellows, since the system will bring the preload pressures into balance through modulating the static tool position. Adjustment is done by shimming, either by washers (on the output rod) or by changing the length of the PZT holder (not pictured

in Fig. 3.1).

The sensor chosen to measure the tool tip displacement was an eddy current sensor. Advantages of this sensor include high resolution (to 0.1% of full scale), compact packaging, high bandwidth, and non-contact sensing. Calibration of the eddy current probe was performed with a displacement probe at the maximum resolution supported ($1\mu m$).

CHAPTER 4

Modeling of a Piezohydraulic Fast Tool Servo

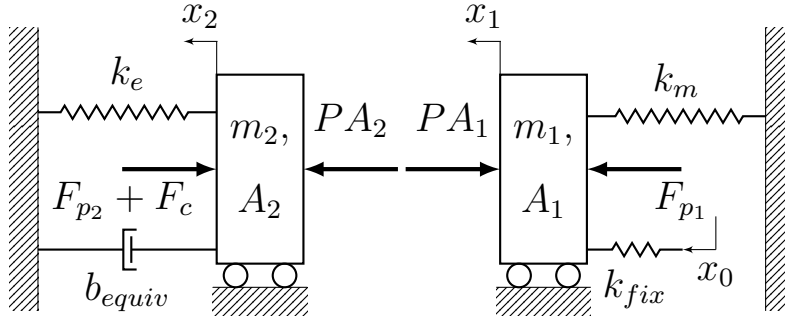


Figure 4.1: System Schematic

Figure 4.1 is an equivalent mass-spring-damper model of the final design, assuming the preload forces, F_{p1} and F_{p2} are sufficient to hold the components together. For the rest of this section, we will assume this holds; the validity of this assumption will be discussed later. A complete list of parameters can be found in Table 4.1. The fluid is modeled by the following:

$$\dot{P} = -\frac{B}{V_0}(A_2\dot{x}_2 - A_1\dot{x}_1) \quad (4.1)$$

which is a simple rearrangement of the definition of bulk modulus; the $(A_2\dot{x}_2 - A_1\dot{x}_1)$ term is simply the time derivative of the net chamber volume change due to the motion of the input and output plates.

The PZT is modeled as a second-order system from control voltage input to displacement

output using the method of [ADB00]:

$$\begin{aligned}
m\ddot{x}_0 + c\dot{x}_0 + k_0x_0 &= \Gamma_0u - k_{fix}(x_0 - x_1 + x_{p1}) \\
m &\triangleq \frac{4m_p}{\pi^2}, \quad k_0 \triangleq k_p + \frac{T_{em}^2}{C}, \quad \beta_0 \triangleq \frac{T_{em}}{C}, \\
\Gamma_0 &\triangleq \beta_0 \frac{C_e}{B_2}, \quad k_e \triangleq k_B + k_R
\end{aligned} \tag{4.2}$$

Since detailed specifications for our PZT are scarce, the lumped parameters m , k_0 , β_0 , and Γ_0 are estimated based on comparable actuators. These parameters will be identified later; for now, the model structure is all that matters. This leads to a seventh-order state-space model, given in Equation 4.3. The two preload forces have been converted to displacements by dividing out the stiffness of the return spring and housing, respectively. This converts the preloads to more measurable quantities, since we have no force sensors within the device, but it is easy to design (or shim) the length of parts to have a specified amount of interference on assembly.

The fluid could have been equivalently modeled as a spring with the aforementioned $\frac{B}{V_0}$ stiffness, but two considerations prevented this: first, modeling it this way is the cleanest way to make the amplification ratio appear in the final transfer function obtained from the model; and second, we plan to make use of a pressure transducer in the chamber as a feedback signal to control this device. Keeping pressure as a state gives a desirable \mathbf{C} matrix structure that simply outputs two states, which will be advantageous later when a structured system identification is performed.

Looking at the structure of the model, we can immediately see that the system matrices are sparse, with relatively few parameters to estimate, which will also lend itself to structured

$$\begin{aligned}
\begin{bmatrix} \dot{x}_0 \\ \ddot{x}_0 \\ \dot{x}_1 \\ \ddot{x}_1 \\ \dot{x}_2 \\ \ddot{x}_2 \\ \dot{P} \end{bmatrix} &= \begin{bmatrix} 0 & 1 & 0 & 0 & 0 & 0 & 0 \\ -\frac{k_0+k_{fix}}{m} & -\frac{c}{m} & \frac{k_{fix}}{m} & 0 & 0 & 0 & 0 \\ 0 & 0 & 0 & 1 & 0 & 0 & 0 \\ \frac{k_{fix}}{m_1} & 0 & -\frac{k_{fix}+k_m}{m_1} & 0 & 0 & 0 & -\frac{A_1}{m_1} \\ 0 & 0 & 0 & 0 & 0 & 1 & 0 \\ 0 & 0 & 0 & 0 & -\frac{k_e}{m_2} & -\frac{beq}{m_2} & \frac{A_2}{m_2} \\ 0 & 0 & 0 & \frac{BA_1}{V_0} & 0 & -\frac{BA_2}{V_0} & 0 \end{bmatrix} \begin{bmatrix} x_0 \\ \dot{x}_0 \\ x_1 \\ \dot{x}_1 \\ x_2 \\ \dot{x}_2 \\ P \end{bmatrix} + \begin{bmatrix} 0 & 0 & 0 & 0 \\ \frac{\Gamma_0}{m} & \frac{k_{fix}}{m} & 0 & 0 \\ 0 & 0 & 0 & 0 \\ 0 & \frac{k_{fix}-k_m}{m_1} & 0 & 0 \\ 0 & 0 & 0 & 0 \\ 0 & 0 & \frac{k_e}{m_2} & -\frac{1}{m_2} \\ 0 & 0 & 0 & 0 \end{bmatrix} \begin{bmatrix} u \\ x_{p1} \\ x_{p2} \\ F_c \end{bmatrix} \\
\mathbf{y} &= \begin{bmatrix} 0 & 0 & 0 & 1 & 0 & 0 & 0 \\ 0 & 0 & 0 & 0 & 0 & 0 & 1 \end{bmatrix} \mathbf{x} + 0u
\end{aligned} \tag{4.3}$$

ID. The PZT dynamics are weakly coupled to the rest of the plant dynamics, which is not immediately apparent until we recall that k_0 is approximately an order of magnitude larger than k_{fix} . Practically, this means that the system dynamics will do little to pull the natural frequency of the PZT down toward the operating bandwidth of our device, which means that we will be unlikely to see the PZT dynamics in system ID.

The first model sanity check is to form the transfer function and ensure that its DC gain at least contains the amplification ratio explicitly. We are only interested in the transfer function from control voltage (u) to tooltip displacement (x_2), so we define new \mathbf{B} and \mathbf{C} submatrices:

$$B \triangleq \begin{bmatrix} B_1 & B_2 & B_3 & B_4 \end{bmatrix}, \quad C \triangleq \begin{bmatrix} C_1 \\ C_2 \end{bmatrix} \quad (4.3)$$

and form the transfer function from u to x_2 :

$$H(s) = C_1(sI - A)^{-1}B_1 \quad (4.4)$$

which is far too lengthy to reprint here. To simplify, we will make the following assumptions for the static case:

1. Fluid is incompressible ($\frac{B}{V_0} \rightarrow \infty$)
2. Housing is stiff ($k_{fix} \gg k_i \forall i \neq 0$)
3. PZT is much stiffer than return spring ($k_0 + k_m \gg k_e$)

With these assumptions in place, the DC gain reduces to

$$H(0) = \left(\frac{A_1}{A_2} \right) \left(\frac{\Gamma_0}{k_0 + k_m} \right) \quad (4.5)$$

with the second term accounting for the transfer function being from PZT control voltage to tool tip displacement, rather than from PZT displacement. The second term is simply the DC gain from control voltage to PZT displacement.

This may seem like many assumptions, but they all hold relatively well in our device; as previously mentioned, the fluid is extremely stiff (which implies near-incompressibility),

the housing stiffness is at least two orders of magnitude larger than any stiffness other than that of the PZT itself, and the PZT is six orders of magnitude stiffer than the return spring. With the underlying assumptions validated, we expect the simplified DC gain to predict the true amplification with negligible error.

Symbol	Units	Description
m	kg	Piezo Element Mass
m_p	kg	Effective PZT Mass
c	$N \cdot s/m$	PZT Damping Coefficient
k_p	N/m	PZT Stiffness
k_0	N/m	Effective PZT Stiffness
Γ_0	N/V	Voltage to PZT Force Gain
T_{em}	-	Amplifier Transformer ratio
C	F	Piezo Capacitance
C_e	F	Piezo Amplifier Capacitance
B_2	-	Piezo Amplifier Gain
k_{fix}	N/m	Housing Stiffness
m_1	kg	Input Diaphragm Moving Mass
k_m	N/m	Diaphragm Stiffness
A_1	m^2	Input Plate Area
m_2	kg	Tool Holder Moving Mass
A_2	m^2	Output Plate Area
k_b	N/m	Bellows Stiffness
k_R	N/m	Return Spring Stiffness
B	N/m^2	Bulk modulus of Hydraulic Fluid
V_0	m^3	Nominal Chamber Volume
F_c	N	Cutting Force

Table 4.1: List of Symbols

CHAPTER 5

Verification of the Completed Device

The model derived in the previous section has an accurate structure, but many coefficients (especially those relating to the PZT dynamics) are unknown or not known to great accuracy. A first-order approach that sufficed during the design phase is to approximate these values with ballpark figures common to similar devices whose properties are better-known. This white-box approach, while passable in the mechanical design phase where safety factors are the rule, is unfit for control design and its more exacting model uncertainty requirements. This concern alone motivates a more precise modeling approach, but another benefit of the physically meaningful model is to back-check parameters of the finished system to ensure that design requirements were met.

A black-box system ID model would be good for control design, as it would capture most precisely the response of the system, but the disadvantage of that method is that the system parameters of the identified model lose physical significance. With this in mind, a hybrid grey-box modeling approach was used to estimate the least-known parameters using input-output data, while preserving the structure of the white-box model. Through this, parameter values can be checked by comparing like terms in the white-box and grey-box models. The model was matched to data taken from a sine sweep of the completed device from control input [Volts] to tool tip displacement [mm], and identified through an adaptive Gauss-Newton algorithm [WN08] with ARX parameter weighting implemented in MATLAB as System ID Toolbox function “ssest().”

All ones and zeros in the state-space matrices were clamped, and all other values were treated as free parameters. To combat the sensitivity to initial conditions and local minimum issues inherent to this nonlinear optimization, the nominal white-box model was used as the

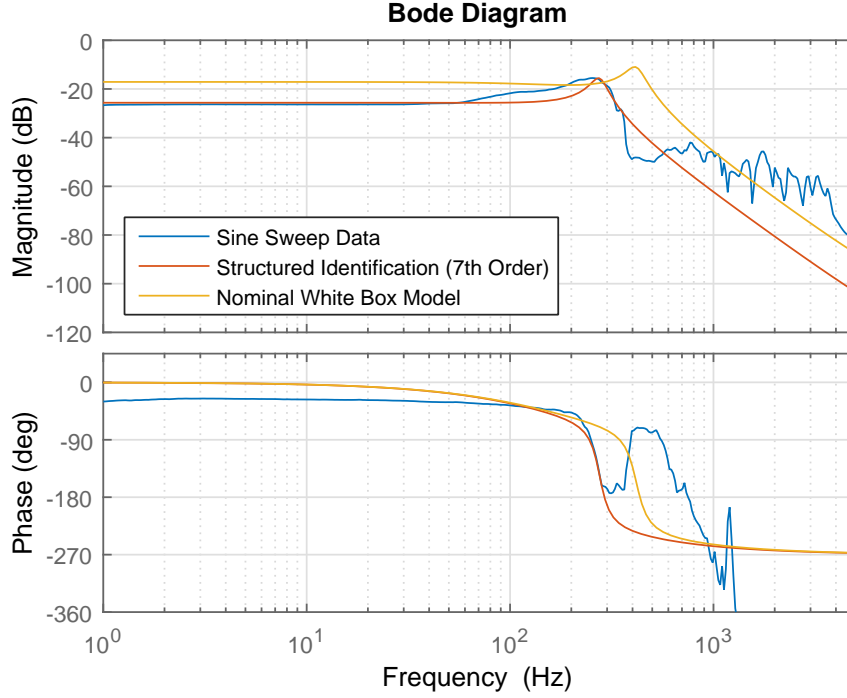


Figure 5.1: Structured System ID Results [Volts to mm]

initial conditions, and some of the free parameters were constrained to lie within general “ballpark” bounds. It is argued that these constraints were appropriate because the final optimized result does not lie at one of the constraint bounds. The results of this structured identification can be found in Figure 5.1.

Comparing like terms between the initial estimate and the final grey-box model, we confirm that most parameters were relatively accurate; a comparison of selected terms can be found in Table 5.1. The largest percentage changes can be found in the parameters we knew the least about— the frictional damping b_{eq} was included but not characterized in the white box model, the gain Γ_0 was not published by the PZT manufacturer, and the stiffness of the housing k_{fix} is subject to variations in material properties and manufacturing tolerances. Using this identified model, we find the -3dB bandwidth of the open-loop system to be approximately 350Hz. Testing the DC gain separately, we found the device to achieve 1.2 millimeters of travel at DC; this fits well with the identified DC gain.

Another quantity of interest is the cutting stiffness of the device; as its intent is to cut

Parameter	White Box	Grey Box	Percent Change
$\frac{b_{eq}}{m_2}$	230.8	281.4	21.9
$\frac{k_{fix}}{m}$	2.52×10^9	2.23×10^9	11.5
$\frac{k_{fix}}{m_1}$	6.8×10^9	5.0×10^9	25.9
$\frac{A_1}{m_1}$	1.58×10^{-2}	1.76×10^{-2}	11.1
$\frac{A_2}{m_2}$	9.4×10^{-4}	8.4×10^{-4}	11.1
$\frac{k_e}{m_2}$	7.7×10^5	6.8×10^5	11.9
$\frac{BA_1}{V_0}$	9.6×10^{10}	9.6×10^{10}	0.0
$\frac{\Gamma_0}{m}$	1.3×10^5	5.0×10^4	61.4

Table 5.1: Comparison of Selected Parameters in White-box and Grey-box Models

material, it must be verified that it is stiff enough to be relatively unaffected by the reaction forces imparted by the workpiece. To quantify static stiffness, weights were hung from the toolholder and the resultant displacement measured with a displacement probe. Results from this experiment can be found in Figure 5.2. To quantify the dynamic stiffness, an impulse hammer test was performed on the device and data taken from both the tool tip displacement and the chamber pressure transducer in addition to the force imparted by the hammer itself. Results from this experiment can be found in Figure 5.3.

5.1 Lumped Model Verification

Up to this point, the fact that the preload forces were sufficient to keep all parts from separating has been taken for granted. This assumption will now be relaxed and a simulation developed to verify it. The model of Figure 4.1 lumps masses of preloaded parts together and

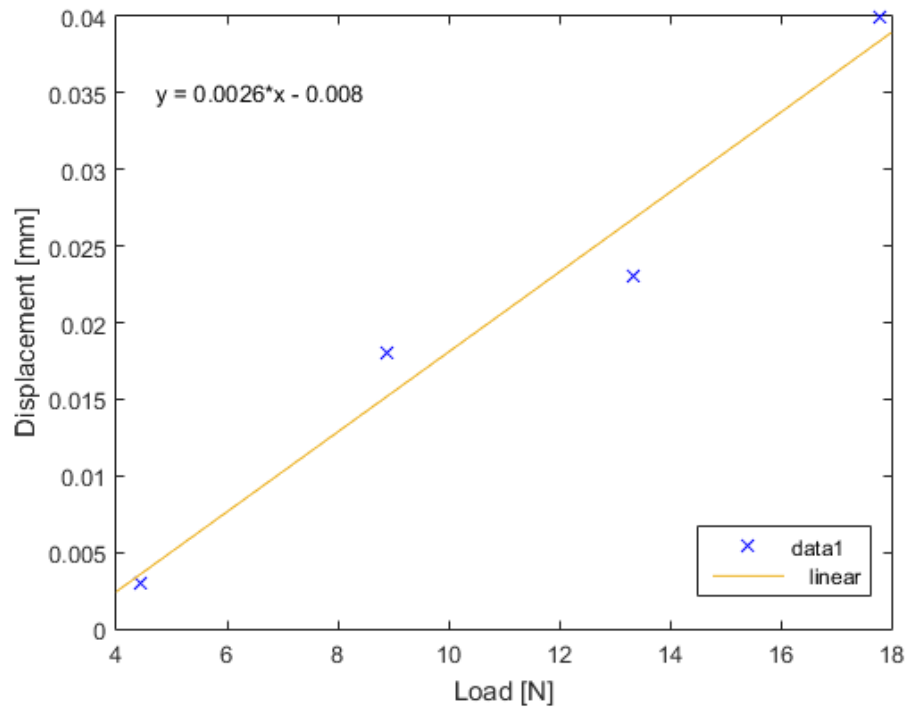


Figure 5.2: Static Stiffness Results

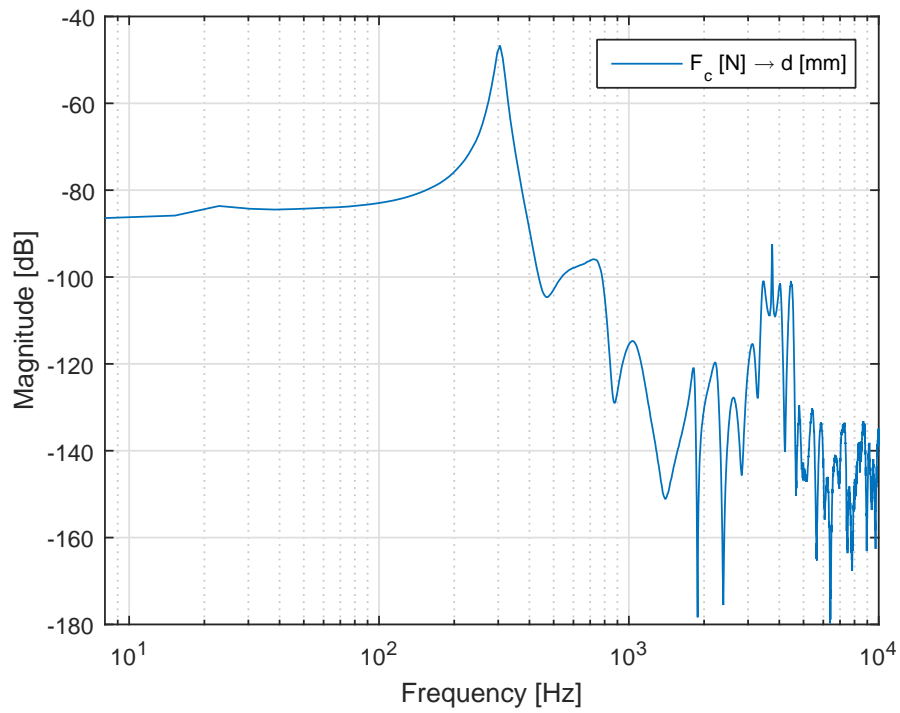


Figure 5.3: Experimental Response from Cutting Force to Displacement

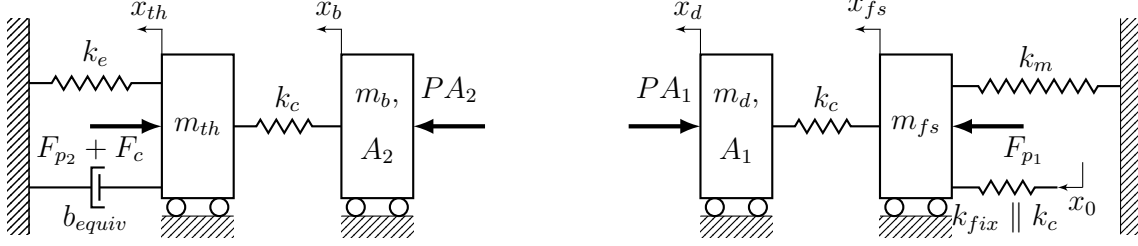


Figure 5.4: System Diagram (Verification Model)

treats them as a single entity; in Figure 5.4, we present a more detailed model that treats each part not permanently affixed to another as its own separate second-order system. In place of the assumption of lumped masses, we place a large contact stiffness between parts that are preloaded together to form the model of Fig. 5.4 and monitor the force of each virtual spring for sign changes. Zero-crossings in the force applied by the contact stiffness to a pair of parts indicate that they are separating, since the contact stiffness can only apply force in one direction.

To validate this model, we changed parameters in our Grey-box model to match an earlier design revision that had exhibited an earlier-than-expected resonance. Frequency response raw data obtained from a swept sine identification of this revision is given in Figure 5.5. Because the early resonant peak's frequency matched the calculated first mode of the tool holder subassembly, it was theorized that the early resonance observed was due to the subassembly resonating at its own separate first mode, which the lumped model should have suppressed. This pointed to separation between the tool holder assembly and the bellows, which we set out to verify using simulation.

To verify our theory, the model of Figure 5.4 was constructed in Simulink and a sine sweep was performed on it. If we began to see zero crossings at or near the first mode of the tool holder subassembly (approximately 165Hz), this would validate the contact stiffness model with as much rigor as possible without inducing more separation, which is dangerous for the metal bellows (of which we only have one). At each frequency swept, the force applied to each of the five preloaded parts by the contact stiffness was checked for sign changes before moving on to the next frequency. Using the parameters from the earlier

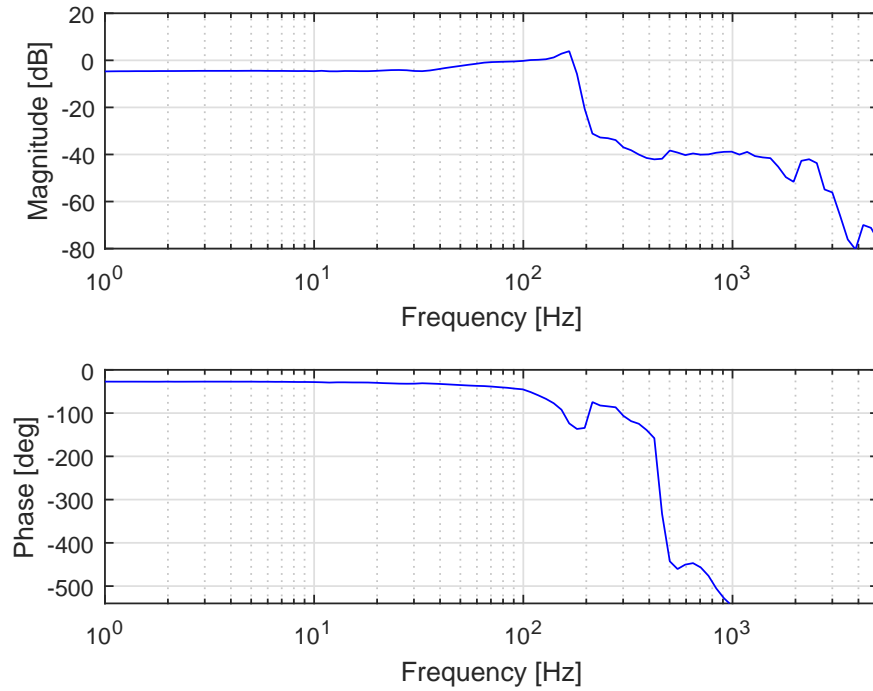


Figure 5.5: Frequency Response When Displaying Early Resonance

revision, we began to detect the onset of separation near the calculated resonant frequency of the tool holder/return spring subsystem. This matched exactly with the observations from the earlier configuration shown in Figure 5.5. With the predictive power of the higher-order model verified, we can now use it to check whether the device will separate given an arbitrary input signal.

CHAPTER 6

System Identification and Control of a Piezohydraulic FTS

This chapter will focus on the identification and control of the completed FTS device. First, the experimental setup is described in Section 6.1. Then, the system identification presented and proposed controller described in Section 6.2. Finally, experimental results and system analysis are presented in Section 6.3.

6.1 System Description

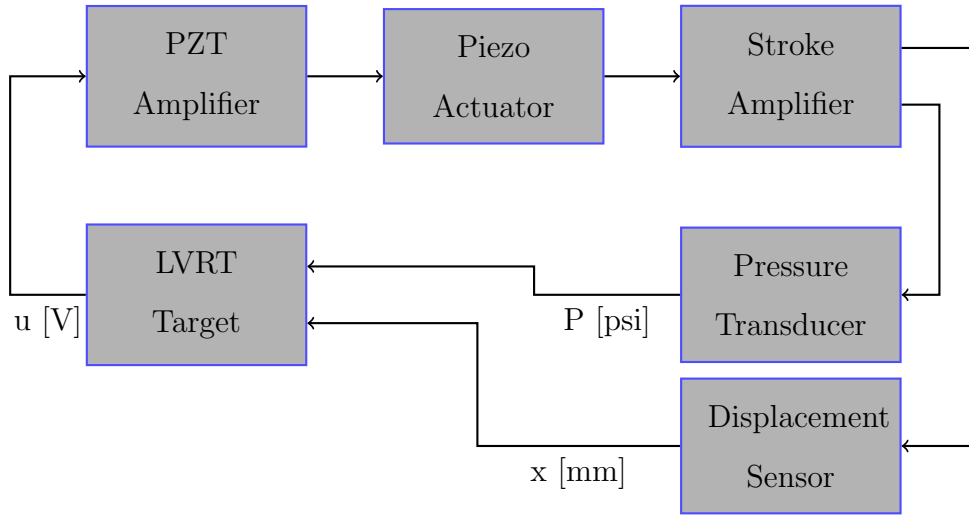


Figure 6.1: System Diagram, Experimental Setup

The experimental setup consists of the following components, shown in Figure 6.2: the FTS device itself and its associated amplifier, external signal conditioners for the pressure and displacement transducers, the real-time target, and the host computer. The real-time

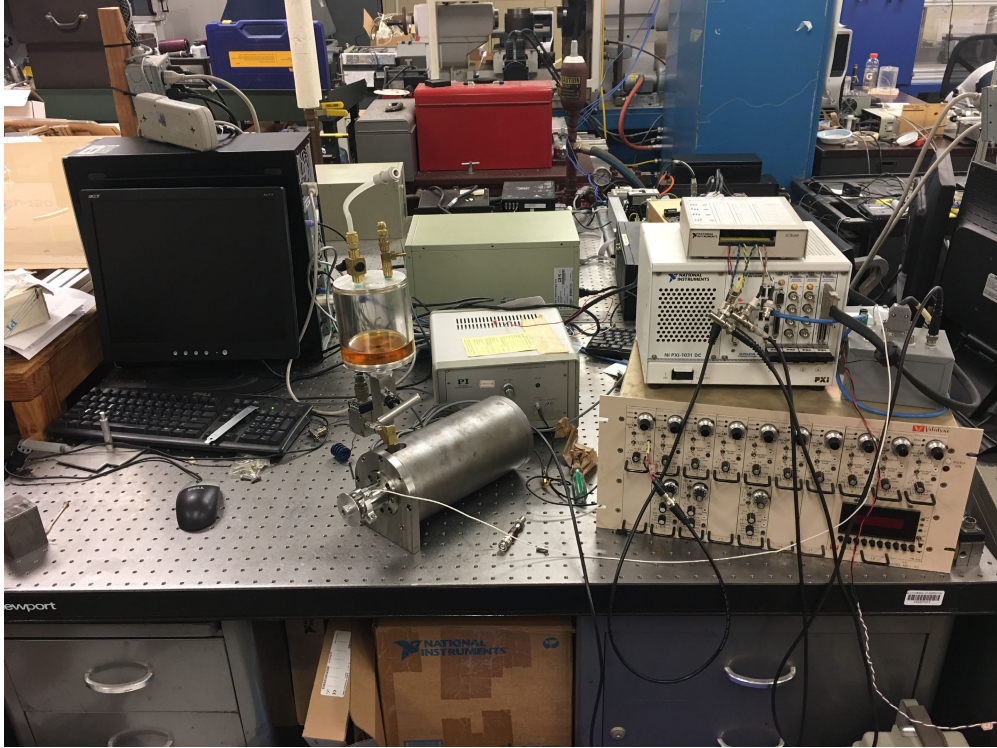


Figure 6.2: Fast Tool Servo Experimental Setup Photo

target is a National Instruments PXI chassis with a PXI-7833R Multifunction RIO data acquisition card installed. The system was sampled at 10kHz for all experiments.

6.2 System Identification and Controller Description

While the model of Chapter 5 was useful for verifying parameters and convincing oneself that design specifications indeed been met, it was decided that for high-performance control design, a black-box system ID model would be better-suited. Four swept sine identifications of the open-loop plant (Control Voltage to Tip Displacement) were performed with the Hewlett-Packard 35670A Dynamic Signal Analyzer over a frequency range of 5 Hz to 5 kHz. The only difference between the back-to-back sweeps was the input amplitude, which varied from 1 Volt (pk-pk) to 5 Volts (pk-pk). It was found that the system had a nonlinearity; the lowest-amplitude sweeps had a fundamentally different Bode diagram than the higher-amplitude sweeps. Results from this experiment are shown in Figure 6.3.

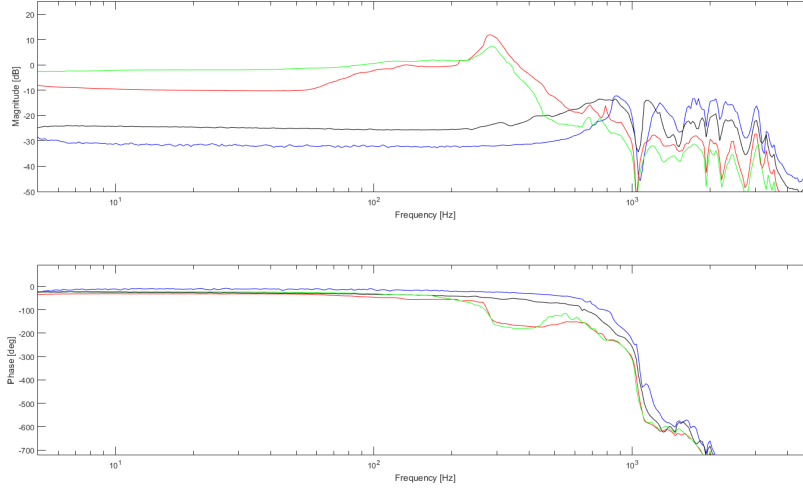


Figure 6.3: Sine Sweep Results, Open Loop Plant [Volts to Volts]

To investigate the source of this nonlinearity, a static experiment was performed where DC steps were fed into the PZT amplifier and the actual tip displacement was measured with an external sensor (Sony Magnescale probe) to eliminate the sensor as a source of nonlinearity. It was found that there existed an approximately two-volt dead zone, after which displacement was linear with control voltage. Results from this experiment are given in Figure 6.4. It was concluded that while a dead zone exists, it should not be responsible for the large variation in system transfer function, as most of the time the control signal does not enter the dead zone. We instead posit that the PZT driving electronics are responsible for this; the PZT amplifier is likely having current saturation issues due to the large load place on the PZT by the amplifier device.

To attempt to apply linear control to this plant, we will assume that the inner-loop controller can keep the control voltage in the linear region. To this effect, we will offset the target piston profile into the system's linear region. Returning to the target piston profile (Figure 6.5), it can be seen that it has a strong harmonic component, but there are repeatable but abrupt changes that need to be tracked precisely. We propose a combination of high-gain feedback (Repetitive control) [TTC89] to track the harmonic components and feed-forward Iterative Learning Control (ILC) [BTA06a] to target the repeated nonharmonic component.

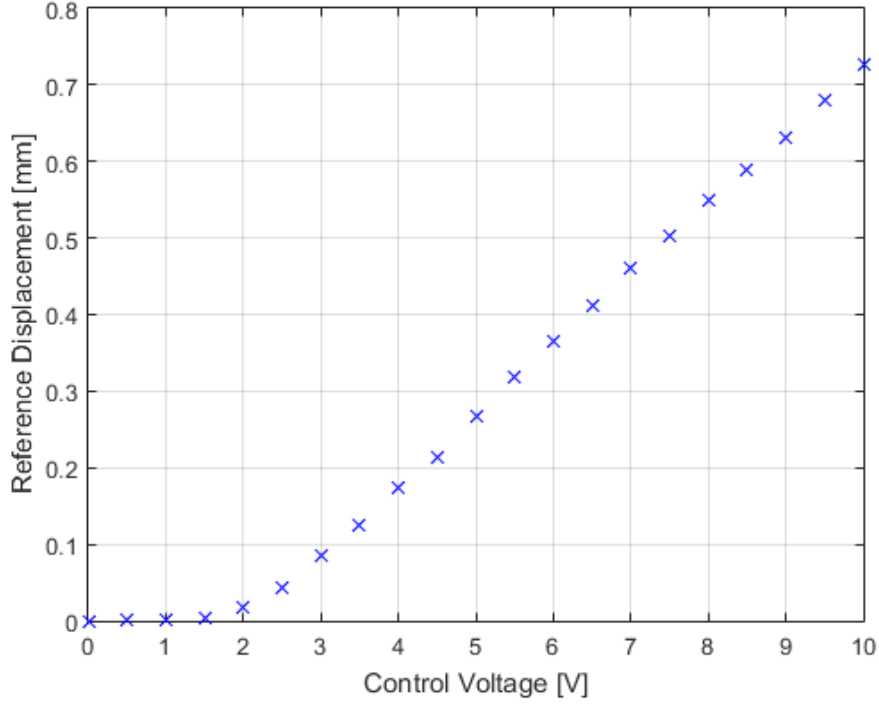


Figure 6.4: Experimental Results, Dead Zone

A Linear-Quadratic-Gaussian controller with integral action (LQGi) serves as the inner-loop controller.

6.2.1 LQGi Design

LQGi control is common in the literature, and no new methods have been developed, but the design process is included here for completeness. The system ID model is put into state-space form as in equation 6.1. The plant model is augmented with an additional state as in equation

$$P(z) = \left[\begin{array}{c|c} A_p & B_p \\ \hline C_p & 0 \end{array} \right] \quad (6.1)$$

$$A_{aug} = \left[\begin{array}{cc} A_p & 0 \\ -C_p & 1 \end{array} \right], \quad B_{aug} = \left[\begin{array}{c} B_p \\ 0 \end{array} \right], \quad C_{aug} = \left[\begin{array}{cc} C_p & 0 \end{array} \right], \quad D_{aug} = 0 \quad (6.2)$$

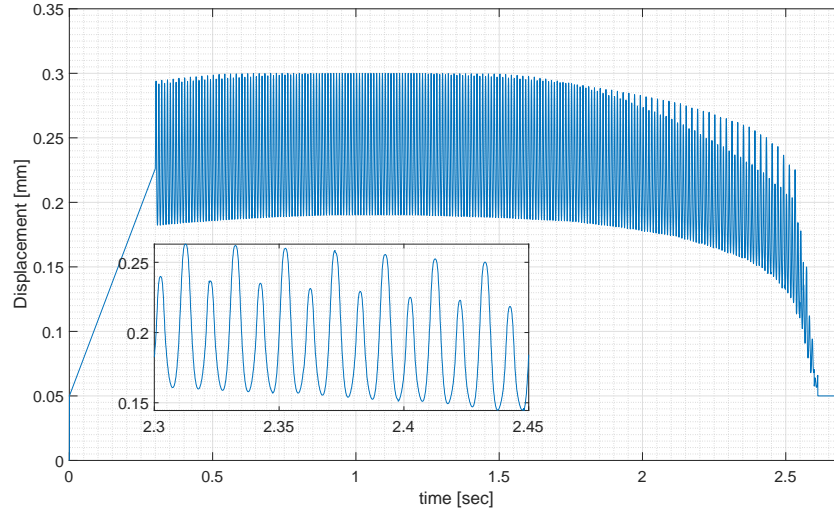


Figure 6.5: Target Piston Profile

The LQGi Controller is implemented as a MISO system as in [RCS16], whose inputs are the plant output y and the error $r - y$. The controller has the form of equation 6.3.

$$C(z) = \left[\begin{array}{cc|cc} A_p - LC_p - B_p K_x & -B_p K_i & L & 0 \\ 0 & 1 & 0 & 1 \\ \hline -K_x & -K_i & 0 & 0 \end{array} \right] \quad (6.3)$$

The controller depends on parameters K_x , K_i , and L , which are the state feedback, integrator, and observer gains, respectively. The state feedback and integrator gains are obtained by solving an algebraic Riccati Equation (ARE). To slightly abuse notation, we will refer to the solution to the discrete time ARE with weighting matrices Q and R as $dlqr(A, B, Q, R)$. With that notation, the state feedback gains are obtained as

$$[K_x K_i] = dlqr(A_{aug}, B_{aug}, Q_k, R_k) \quad (6.4)$$

where the weighting matrices Q_k and R_k are parameterized as in equation 6.5

$$Q_k = \begin{bmatrix} \alpha I & 0 \\ 0 & \beta \end{bmatrix}, \quad R_k = 1 \quad (6.5)$$

This allows us to parameterize the LQGi controller with only two parameters: one controlling the state-feedback portion, and the other controlling the integrators.

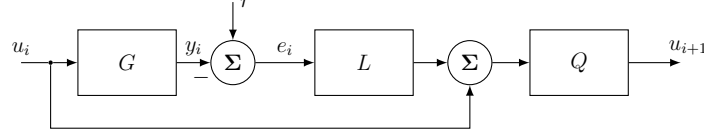


Figure 6.6: ILC Controller Structure

The observer gains are obtained in a similar manner, by solving the ARE

$$L^T = dlqr(A_p^T, C_p^T, Q_o, R_o) \quad (6.6)$$

with weighting matrices Q_o and R_o used as tuning parameters.

6.2.2 ILC Design

First, the ILC is allowed to converge to a final feed-forward input sequence, according to the update law in Equation 6.8 and Figure 6.6. Q is a linear phase low-pass filter as in equation 6.7, with order 6 and serves to reduce the effect of poorly-modeled high frequency system dynamics. L is an inversion of the closed-loop plant G , obtained through Zero Phase Error Tracking Control (ZPETC) [Tom87]. During the learning process, the Repetitive Controller is left disconnected and not allowed to interfere. This allows the ILC and Repetitive controllers to be designed separately. The iterative nature of the learning process allows a more aggressive Q filter, by setting a small learning gain to ensure that each successive iteration differs minimally from the previous. This allows us to venture further into the high-frequency region than a high-gain feedback type controller like Repetitive.

$$Q = \left(\frac{z + 2 + z^{-1}}{4} \right)^{N_q} \quad (6.7)$$

$$u_{ILC}(k+1) = Q[u_{ILC}(k) + \mu Le(k)] \quad (6.8)$$

After ILC has converged to a steady-state feed-forward input, adaptation is halted and ILC behaves as a static feed-forward filter. At this point, the Repetitive Controller is connected and attenuates any remaining harmonics of its design fundamental frequency in the error.

6.2.3 Repetitive Controller Design

A block diagram of the full controller is given in Figure 6.7; in this diagram, Q is again a zero-phase low pass filter as in equation 6.7, but of order 10, and F is identical to the filter used as the learning filter in the ILC formulation.

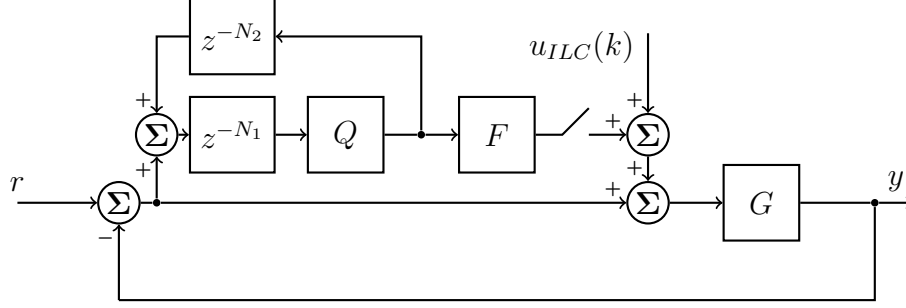


Figure 6.7: Block Diagram, Proposed Controller

With the plant inversion already obtained, the main variable in the Repetitive Control design was the Q filter, whose order was optimized to ensure Robust Stability. Robust stability and Sensitivity analysis was performed on the LQGi closed loop with the Repetitive plug-in controller, and a multiplicative plant uncertainty was assumed as shown in Figure 6.8. An uncertainty bound was calculated by the difference between the control design model and the raw frequency response data used to obtain it. From small gain theorem, a sufficient condition for robust stability is

$$|TW_r| < 1 \quad (6.9)$$

where T is the complementary sensitivity function and W_r is the uncertainty bound obtained earlier. To calculate the sensitivity and complementary sensitivity functions, the loop gain

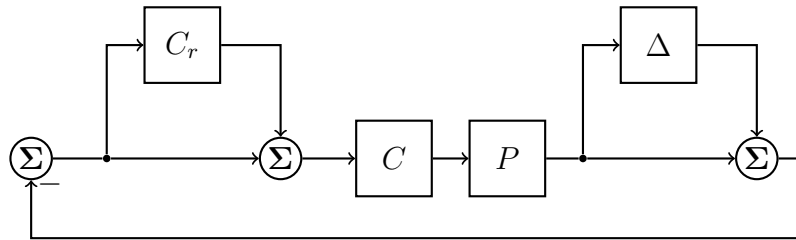


Figure 6.8: Multiplicative Uncertainty Model

must be obtained. When the reference is assumed zero, the MISO LQGi controller can be reduced to a SISO controller $C = C_2 - C_1$, where C_1 is the transfer function of the MISO controller from plant output to control (the state feedback portion), and C_2 is the transfer function from error to control (the integrator(s)). With this simplification, the loop gain can be shown to be

$$L = (1 + C_r(z))(C_2(z) - C_1(z))P(z) \quad (6.10)$$

$$C_r = \frac{Q(z)F(z)z^{-N_1+N_q}}{1 - Q(z)z^{-N_1-N_2+N_q}} \quad (6.11)$$

with C_r representing the Repetitive Controller and defined as in equation 6.11. Once the loop gain is obtained, the sensitivity and complementary sensitivity functions can be easily computed from textbook formulas.

A graphical method of verifying the condition of equation 6.9 is to plot the magnitude of both functions and ensure that T is below W_r over the entire frequency band; this method is shown in Figure 6.10. The complementary sensitivity function is plotted for both the LQGi-only case and the case with the plug-in repetitive controller switched on. To achieve robust stability, the low-pass filter Q in the repetitive formulation must be tuned to cut off the high-frequency peaks in the complementary sensitivity function due to repetitive targeting all harmonics of the fundamental repetitive frequency. This sacrifices performance for robustness, as can be seen in the sensitivity function, plotted in Figure 6.9. The normally-deep repetitive notches in the sensitivity function are only down 40dB at maximum, due to the effects of the Q filter to achieve robust stability.

6.3 Experimental Results and Analysis

The first experiment performed was to track the piston profile using only the inner-loop LQGi controller. Results are given in Figure 6.11, and it is clear from the tracking results that while the inner-loop controller performs reasonably well tracking the amplitude of the

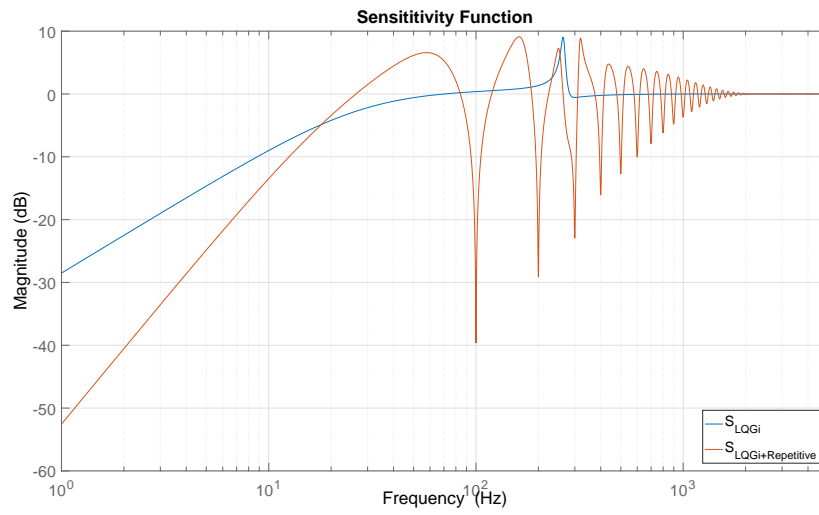


Figure 6.9: Sensitivity Analysis

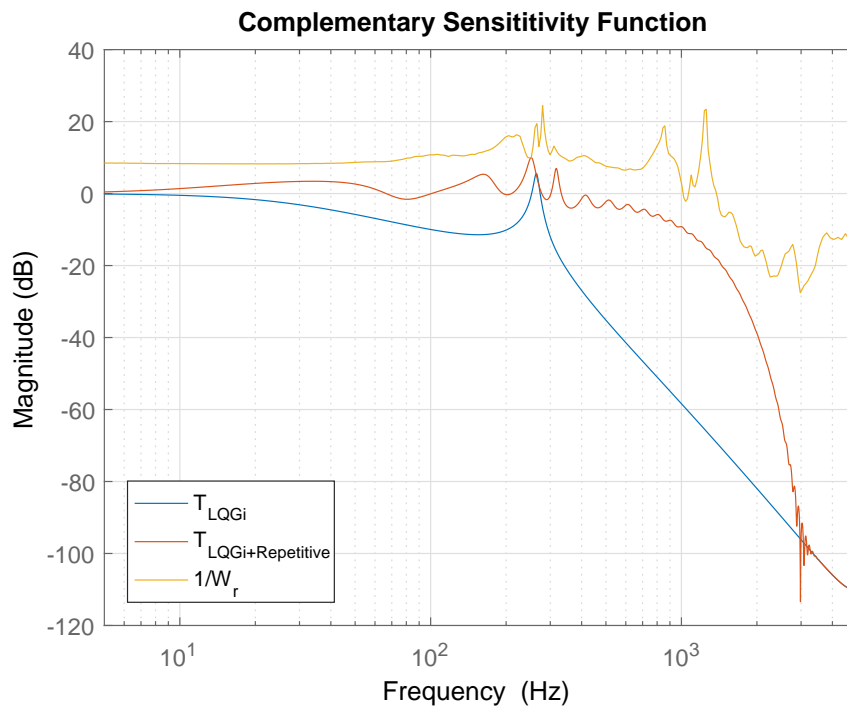


Figure 6.10: Robust Stability Analysis

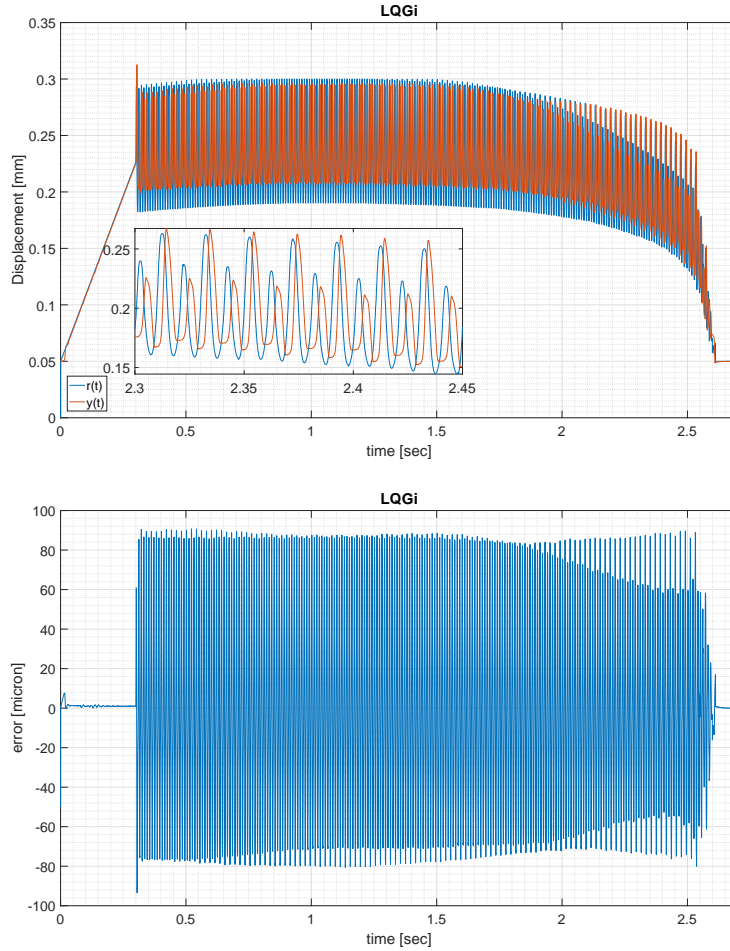


Figure 6.11: Experimental Results: LQGi Inner Loop Only

mostly-harmonic section (inset), the phase delay is large. This contributes to its worst overall tracking performance, with 52.9 microns RMS error. To attempt to reduce the phase error, the Repetitive Controller is switched on in addition to the LQGi inner loop. Results are given in Figure 6.12. Though Repetitive Control corrects the phase error, it fails to completely track the reference, especially near the direction changes, and exhibits a large transient in the transition between the ramp and the actual profile. The Repetitive Controller tracks the reference better than LQGi alone, reducing the tracking error to 10.5 microns RMS. For the third test case, ILC is enabled (after converging to steady-state) in conjunction with the inner-loop LQGi controller. As expected, this produces the best overall tracking performance thus far, also compensating for the phase delay in the large-amplitude section (inset).

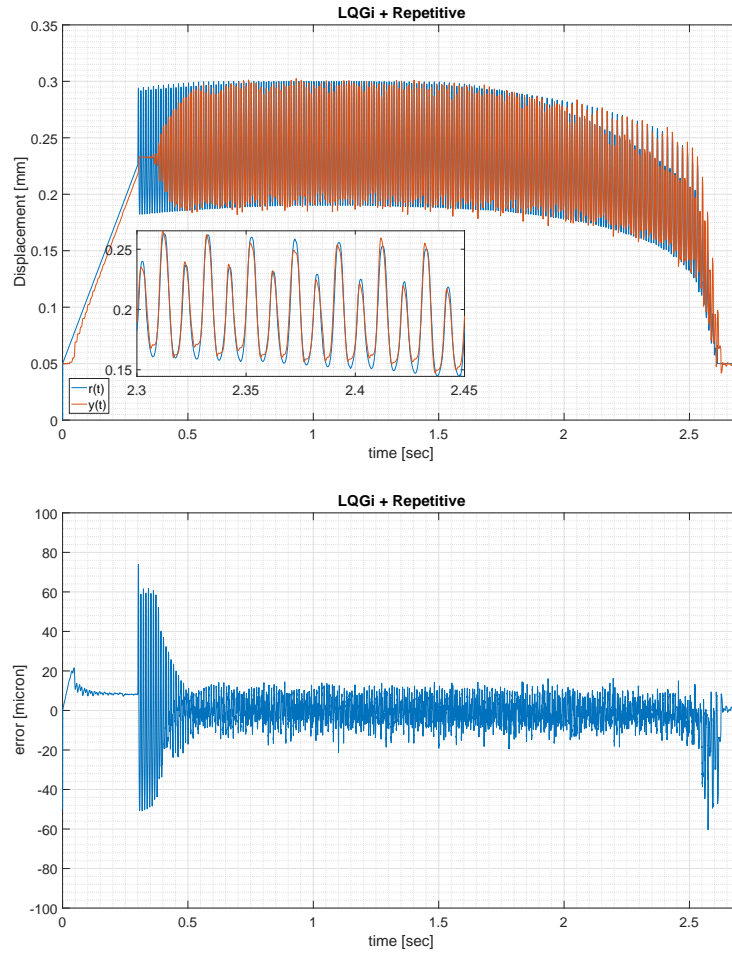


Figure 6.12: Experimental Results: LQGi + Repetitive Control

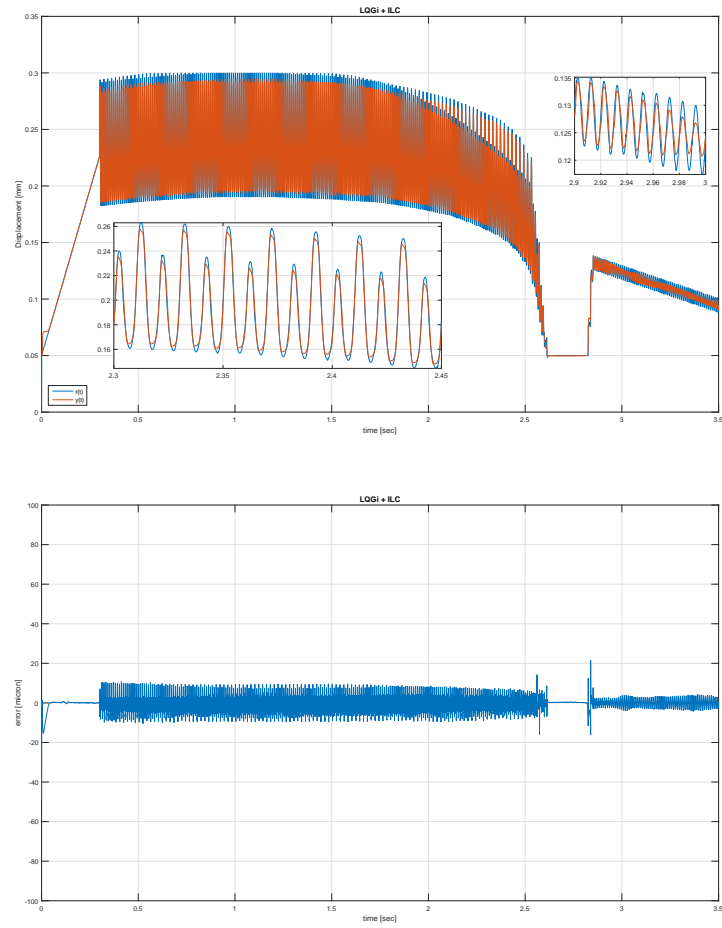


Figure 6.13: Experimental Results: LQGi + ILC

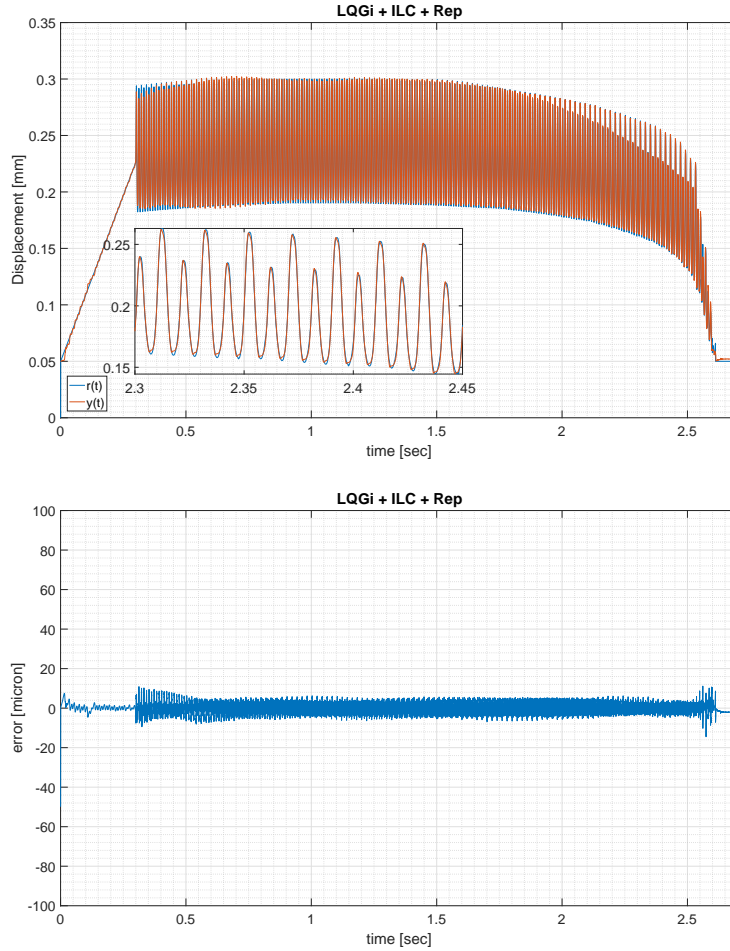


Figure 6.14: Experimental Results: LQGi Inner Loop + ILC + Repetitive

However, these tests are under ideal conditions, with no disturbance force imparted to the toolholder as there would be had it been cutting metal. The addition of the Repetitive controller adds disturbance rejection capability and also increases the performance somewhat. Results from the combination controller are given in Figure 6.14, which shows that the addition of the Repetitive controller results in the best tracking performance of all controllers tested at 2.8 microns RMS error. Tracking results are summarized in Table 6.1. Looking at the results spectrally, Figure 6.15 shows that at the main harmonic component of the profile (100Hz), Repetitive control alone provided roughly 40dB of error reduction, ILC alone provided nearly 60dB, and the combination controller reduced that harmonic in the error signal by 70dB.

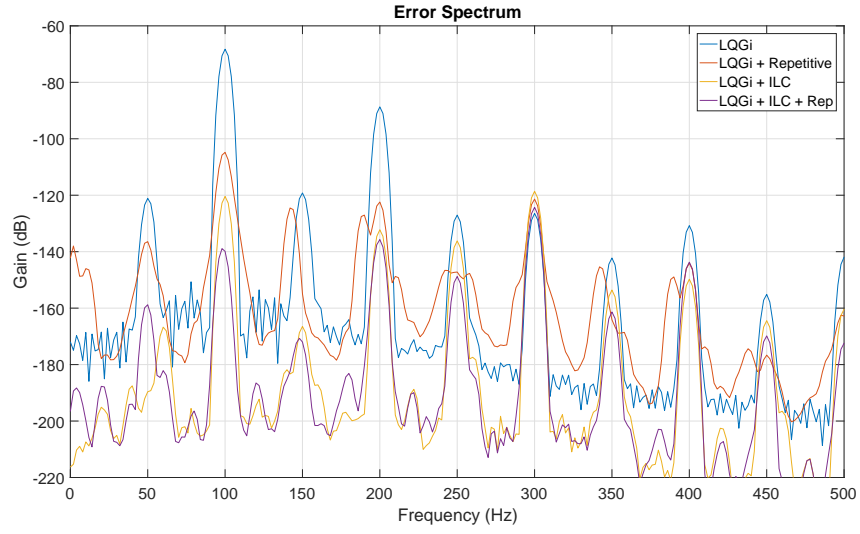


Figure 6.15: Experimental Results: Error Spectrum

Controller	RMS Error [μm]
LQG with Integral Action (LQGi)	52.9
LQGi with Repetitive	10.5
LQGi with ILC	4.2
LQGi with Repetitive and ILC	2.1

Table 6.1: Summary of Control Results

CHAPTER 7

Conclusions

In this research, we have developed a novel piezo-hydraulic Fast Tool Servo design that achieves a 1.2-mm DC stroke and 350Hz of open-loop bandwidth. We have derived a white-box model from first principles and estimated parameters of our system to populate it. We have then performed a black-box system identification and combined our previously-derived model and our input-output data to obtain a grey-box model whose parameters are physically significant. This model and data was then used to verify the performance of our system and show that design specifications were met. A higher-order, nonlinear model to predict separation of the preloaded components was developed and tested against real-world observations and can be used to reliably show that the final design iteration will not separate through its usable bandwidth.

A black-box system identification was performed and a control design model obtained. System nonlinearity was investigated and characterized, and an inner-loop controller designed to minimize its effect. A combination feedback and feed-forward outer-loop controller was designed and implemented on the physical system, and a real-world test pattern was tracked. Experiments were performed to verify that the combination control strategy exhibited the lowest tracking error of all controller permutations.

Part II

MR-Compatible Fluid Actuators for Robotic Interventions

CHAPTER 8

Introduction to MR Robotics

Magnetic Resonance (MR) Image-based techniques have shown great promise in the field of interventional oncology. MR imaging offers the best combination of detection capability and real-time imagery out of the available imaging options. In addition to lesions which are invisible to other imaging methods, MRI can detect other tissue structures, such as blood vessels and bile ducts, which must be avoided for a successful procedure. It also delivers no radiation dose to the patient, enabling imagery to be gathered continuously throughout the procedure. This is especially important in the abdominal region, where breathing motion renders most lesions non-stationary. It is not without its limitations, however—current scanner technology provides very limited access to the abdominal region of the patient during imaging, and real-time MR imagery suffers from appreciable latency and low frame rate. Current strategies for image-based interventions include step-and-shoot methods and/or manual manipulation of the instrument while the patient is still in the scanner bore [KGM15], but both of these strategies are inherently limited in their accuracy and reproducibility. A robotic system, placed in the scanner bore with the patient, has the potential to remedy these issues by removing the accessibility concern entirely and by mitigating accuracy and target motion concerns through closed-loop target tracking—either in an assistive or fully-autonomous capacity.

While it is clear that robotic systems can help to mitigate many of the issues associated with MR-guided interventions, the MR environment itself poses substantial challenges to the implementation of such systems. Due to the high magnetic fields present at all times in the scanner bore—between 1.5 and 3T—any ferromagnetic components, or electromagnetic actuators and sensors are prohibited due to safety concerns. In addition to the safety issues,

they also introduce artifacts that degrade the imagery obtained from the scanner. These concerns alone eliminate the most common actuation/sensing modalities and engineering materials out-of-hand, complicating design of the robotic system—to ensure compatibility across a variety of scanners, devices must be designed from the ground up with compatibility as a priority [GMB06].

Several alternatives to traditional electromagnetic actuation have been investigated. Piezo-ceramic actuators have been shown to work in the MR environment safely, but the voltages required to obtain meaningful actuation degrade signal-to-noise ratio (SNR) and leave artifacts on the imagery obtained [MGR08, KSC13, SZC11, TCO08, EZR08]. Steps can be taken to reduce the effects of the actuators on the imagery, but the authors prefer to circumvent that issue entirely. Purely mechanical transmissions suffer from backlash and are comparatively complicated to implement [ETH08, GYC06]. Pneumatics are the most widely-used actuation system in the literature, but are typically high-pressure systems with pumps and valves, and can present difficulties in implementing position control [MGR08, BZJ08, GYC06, YTM11]. High-pressure operation can be a safety concern with the system so close to the patient; pumps or valves compromise native haptic feedback/backdrivability, and increase maintenance complexity and system cost. Stoianovici, et al demonstrated a pneumatic stepper motor for MR-compatible applications, but their system is designed strictly for control, with no haptic feedback capability [SPP07]. Directly comparing pneumatic and hydrodynamic actuators, Yu et. al found hydrodynamic actuators preferable when positioning accuracy was more important than overall bandwidth [YHB08].

We propose a hydrostatic actuation concept that offers native haptic feedback, inherent backdrivability, and completely MR-compatible transmission of force and displacement. Further, in our concept, actuators can be easily connected to form a low-pressure, multi-master “fluid network” architecture to enable co-robotic operation—collaborative control of the end-effector by several master units—which can be completely human-controlled, completely robotic, or somewhere in between. In this collaborative framework, the inputs of the various master units are blended naturally in the hardware, allowing a wide range of switchable modes of operation (e.g. master-slave, co-robotic, and fully autonomous) to be

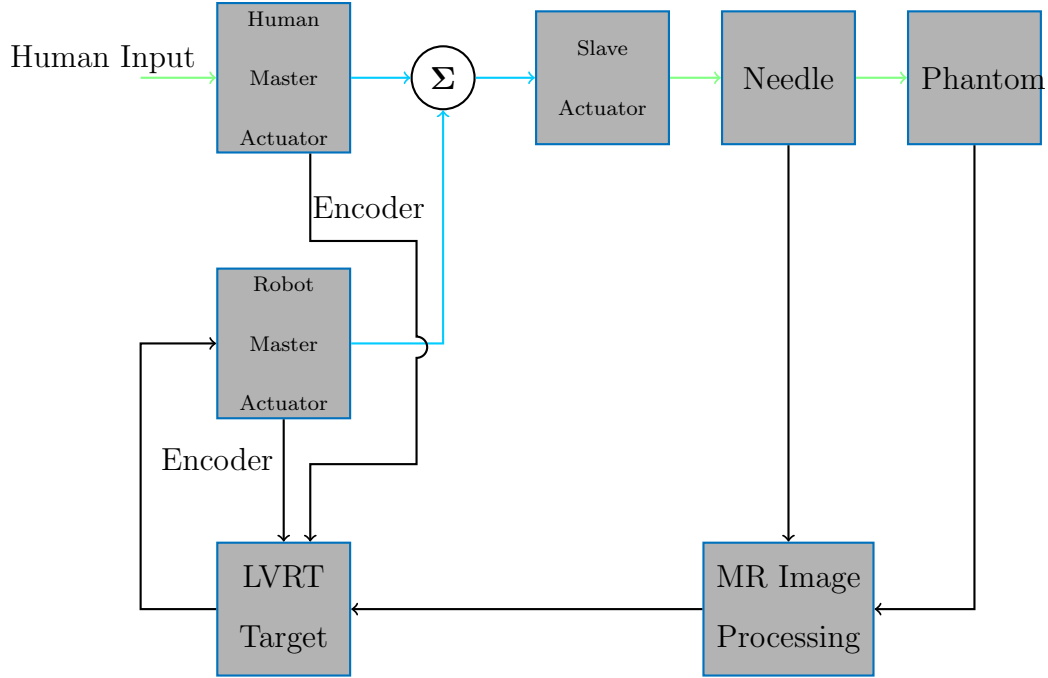


Figure 8.1: MR Robotics System Schematic

realized.

Co-robot (multi-master) operation is the concept of multiple master units, under varying degrees of human and computer control, collaboratively controlling the output of a single slave unit. The hydrostatic system is a closed system, so it can be seen that the net volumetric displacement of the master units will be the negative of the volumetric displacement of the slave unit; that is, the slave will sum the inputs of all of the connected masters. This allows for interesting collaborative schemes, such as input scaling—where the robot sets its input such that slave’s output is a scaled version of the human’s input, frequency crossover—where the human and robot each are responsible for some frequency band, and virtual wall—where the robot does not interfere with the human, until the slave unit is about to cross into a restricted zone, and then negates the human’s input as long as the human attempts to move into that zone. Haptic feedback can be provided to users through the fluid pressure—shared across all units—or through electromechanical actuators attached to individual master units.

Figure 8.1 gives an overview of the proposed closed-loop system. In this diagram, black lines denote signals, blue lines fluid transmission lines, and green lines physical contact and

manipulation. Because of the anticipated low data rate from the MR Image Processing algorithm, we have a data fusion problem where the slave position is extrapolated from the master units' encoders at the control loop rate, and is updated periodically by the lower-rate measurement from the MR Image Processing algorithm.

8.0.1 Previous Work

The first iteration of the MR Robotics device was a two degree-of-freedom planar gimbal mechanism, actuated by two sets of medical-grade plastic syringes, oriented back-to-back to form a double-acting hydraulic piston [Yas14]. Syringes were chosen as the prototype's hydraulic pistons because MR-compatible pistons are not easily commercially available, and are difficult to manufacture in-house. This design was successful in positioning a needle in two angles [YMS14], but precise positioning was made difficult by the backlash in the mechanism and by the stiction in the syringes. Results from this iteration are given in Figures 8.2 and 8.3. It was clear that the syringes, while easily available and fully compatible, would need to be replaced.

This original mechanism was then modified, retrofitted with a third syringe-piston to add a third, linear degree of freedom to the unit. This design was tested for MR-compatibility and feasibility of targeting using real-time MR image feedback [MYR15]. A control scan of a stock MRI test target was done without the robotic system, and its signal-to-noise ratio (SNR) was computed. The scan was repeated with the robotic system in the bore along with the test target, and a difference of 2.2 percent was found. A custom MR phantom was made of gelatin with a bead suspended inside to act as a target for positioning testing, and an operator manipulated the 3DOF system using real-time MR image feedback. When the operator was satisfied, a high-resolution 3D scan of the phantom and robotic system was performed and the error between the needle tip and bead location was computed. The system achieved an average needle-tip error of 1.34mm.

This iteration had also piloted the usage of a ground glass syringe as a piston, instead of the plastic-body-with-rubber-wipers type used in previous iterations. Having found during

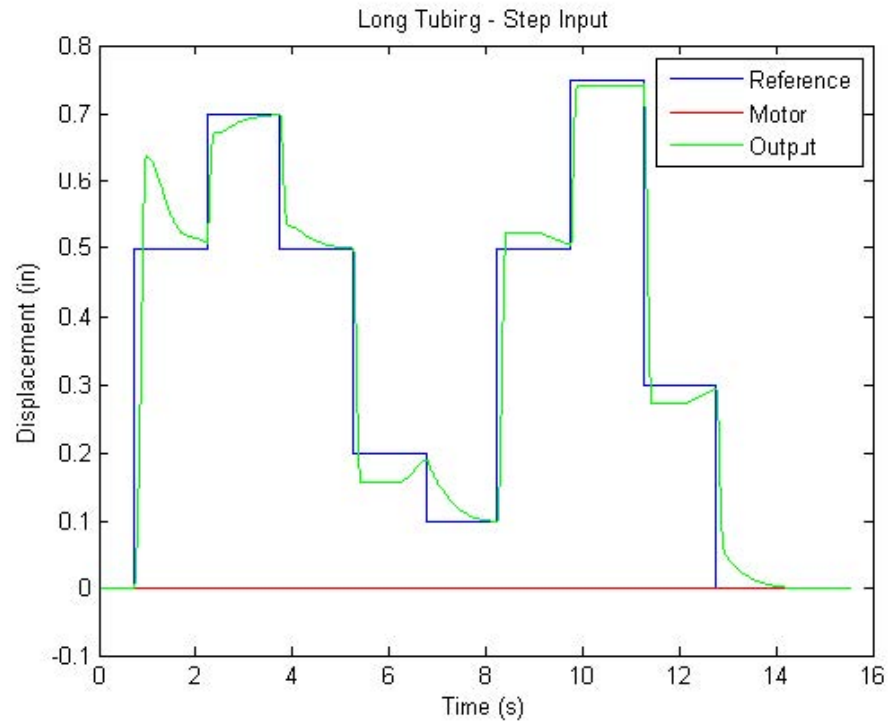


Figure 8.2: MR Robotics, First Iteration Tracking Results [Yas14]

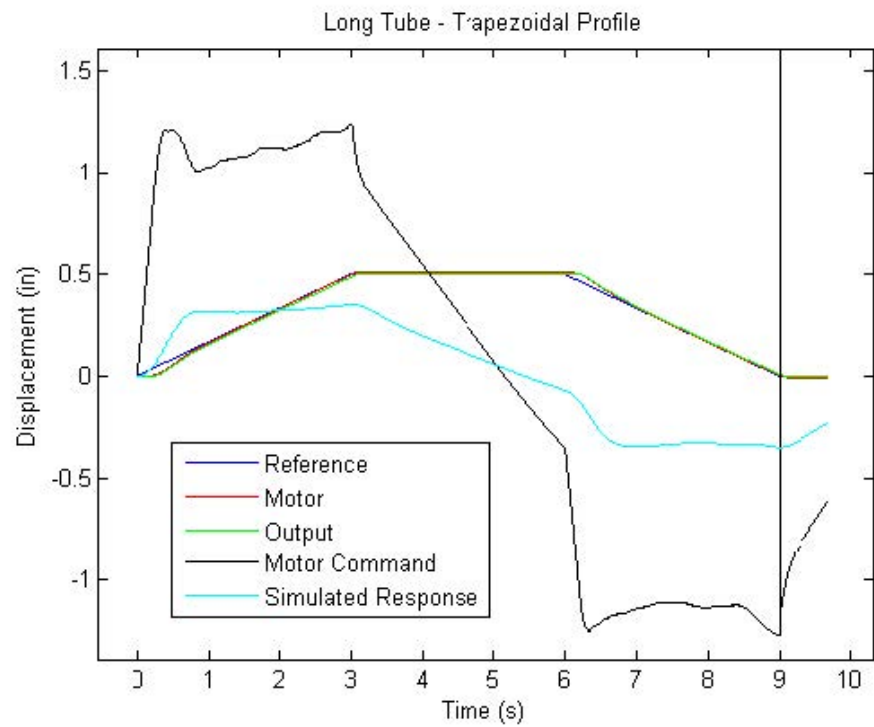


Figure 8.3: MR Robotics, First Iteration Comparison to Model [Yas14]

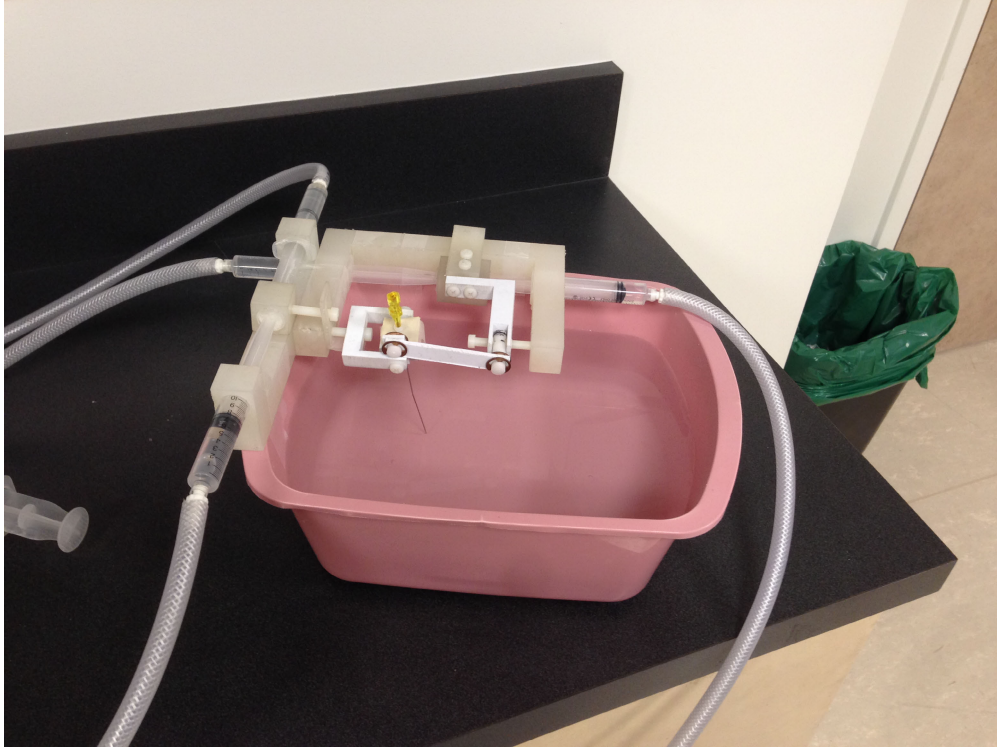


Figure 8.4: MR Robotics, First Iteration

the experiment that the third DOF that used the glass syringe was easier to manipulate and less prone to stiction, the mechanism was retrofitted with all glass syringes. Though superior to their plastic counterparts in stiction performance, the glass syringes led to their own issues: glass syringes tolerate far less concentricity errors in the double-acting piston construction than the plastic syringes, and the seal between plunger and cylinder is not meant to be pressurized. To absorb concentricity errors, wave springs were placed between the ends of each plunger and the output block connecting them, but this required preloading the springs through pressurization of the fluid, which led to unacceptable leakage from the syringes, and the additional springs created more backlash in the mechanism. This led to the abandonment of syringes as hydraulic piston stand-ins, and of the piston-cylinder design in general, having found that it forced a tradeoff of friction/stiction and sealing performance.

Having abandoned the traditional piston-seal-cylinder design, we sought a new method of sealing that had low friction, high stiffness, medium-high stroke potential, and that did not trade friction for sealing performance. The two designs we found to satisfy those criteria

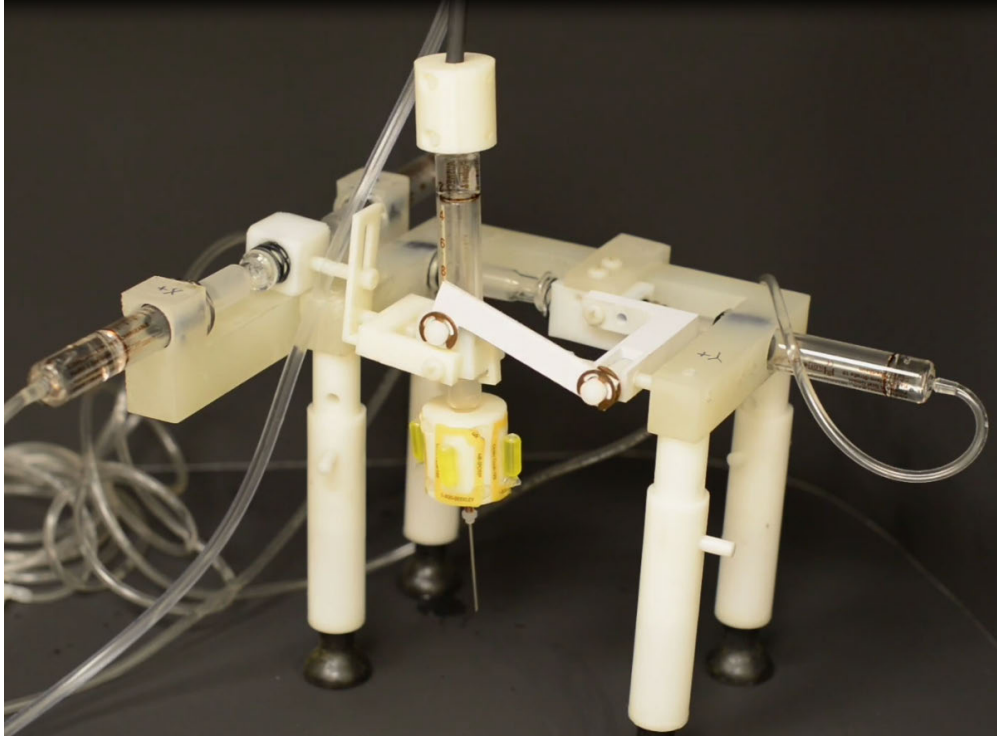


Figure 8.5: Glass Syringe Prototype

were the bellows and the rolling diaphragm, and since the way to make a bellows stiff enough while remaining MR-compatible was not obvious, the rolling diaphragm served as the base of a new actuator design. It was at this point that the focus of this project switched to the development of the actuator, rather than the system as a whole.

Whitney, et al. developed a robot based on the rolling diaphragm actuator and demonstrated the actuator’s desirable properties, but while they noted that MR would be a good potential application of the technology, their actuator was not designed to be compatible [WGB14]. Whitney showed a double-acting rotary fluid actuator with high stiffness and very low stiction and backlash that ran with both air and water as a working fluid. They noted that “This fluid-based transmission could also be used for building an MRI-compatible robot, especially if maintaining backdrivability is desired. [...] The high stiffness and high force bandwidth allow haptic-quality direct force feedback to the operator.” With this in mind, we set out to design an MR-compatible actuator from the ground up, but found that inherent MR-compatibility was not the only advantage that this mechanism could of-

fer to the application. Whereas the existing work focused on master-slave operation, our work exploits the hardware input blending capability of the hydrostatic actuator to implement native collaborative control of a slave actuator by multiple master units. We have also converged on what we believe to be a better way to connect the two pistons in the double-acting arrangement—Whitney’s double-acting actuator uses external elements (such as timing belts) to connect the two pistons, where in our design, the two pistons are one piece. This eliminates a source of compliance and reduces mechanical complexity.

CHAPTER 9

Design of MR-compatible Linear Actuators

9.1 Diaphragm Design

The first problem to address after the switch to the rolling diaphragm was the limited commercial availability of the diaphragms themselves. Unable to find a manufacturer willing to source small quantities of diaphragms, we resolved to design and manufacture our own. Using publicly available specifications from one of the larger manufacturers, we designed our first diaphragm, at 0.5-inch stroke and 0.5-inch diameter. The diaphragm has a fairly complex shape, but the draft angle that allows it to roll on itself also lends itself to molding, so a two-part mold was designed to manufacture the diaphragms.

Both mold halves were milled from billet aluminum and were designed so that each would be a 2.5D part capable of being produced on a 3-axis CNC with minimal fixturing. Care was taken to making the finished mold surface as smooth as possible to reduce transfer to the molded part, but scallops from the surfacing process are still visible on the finished parts. We do not believe this has an effect on diaphragm performance. The mold gate was placed coincident with a hole required for bolt-through of the diaphragm to the piston, so all sealing surfaces would be smooth and free of runners.

Silicone was chosen as the diaphragm material due to its availability, non-toxicity, and room-temperature cure. The degassed liquid rubber was injected into the mold using a standard syringe until rubber flowed out of the gates on the top side of the mold, and was then left to cure. Fabric reinforced diaphragms were also produced using the same technique; creating them required an additional step of stretching a fabric mesh over the male part of the mold prior to the assembly of the mold. Figure 9.1 shows the custom tooling for making



Figure 9.1: Custom Diaphragms and Tooling

diaphragms and examples of unreinforced and reinforced diaphragms made using the process developed here.

9.2 Single-Acting Diaphragm Actuator

With the first-generation diaphragms completed, a single-acting diaphragm actuator was designed to test the proof of concept. Figure 9.2 is a sectioned view of the single-acting design, and Figure 9.3 shows the final manufactured actuator. Designed to be MR-compatible first and foremost, metals were foregone where possible; all components were made of various plastics (Delrin, Delrin AF, Nylon), except for the output rod, which was made of Brass. We were forced to use Brass instead of plastic due to two concerns: first, Brass is more rigid and resistant to side-force in the aspect ratio necessitated by the design than plastics, and second, Delrin AF is designed to be a journal bearing material for metal shafts, so Brass has better friction properties when coupled with a Delrin AF bushing. The journal in the Lower

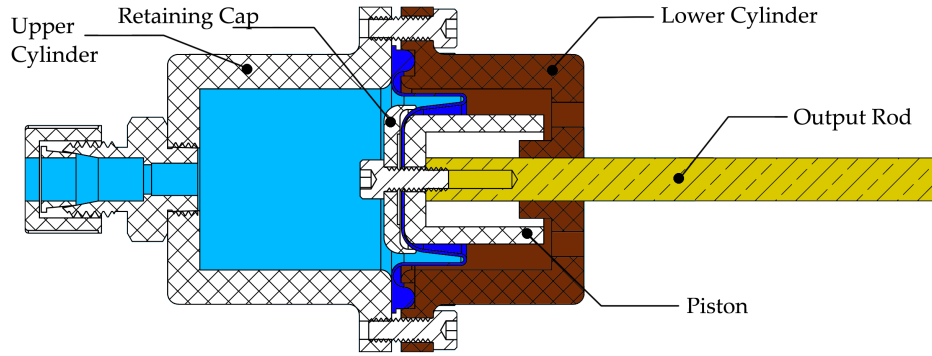


Figure 9.2: Single-Acting Diaphragm Actuator Design, Section



Figure 9.3: Single-Acting Diaphragm Actuator, as Manufactured

Cylinder serves to stabilize the piston-diaphragm system against buckling, and should be subject to little side-force (and consequently friction) during normal operation. The Lower Cylinder was also made of Delrin AF for its better friction properties. All other parts (Piston, Retaining Cap, and Upper Cylinder) were made of Delrin for its easy machinability and intrinsic MR-compatibility. The bolt-through-flange design was chosen because it is simple and allows for rapid dis- and re-assembly, which is important while testing different diaphragms and for when they fail. The Piston was made hollow due to the long piston skirt length specified by the diaphragm design manual and the limited availability of long, Nylon cap screws. The Retaining Cap serves two purposes: to form a seal against the top side of the diaphragm, and to keep the diaphragm (which must be inverted prior to assembly) from returning to its as-molded state and jamming the mechanism.

Initial experiments proved that a small preload pressure was necessary in addition to

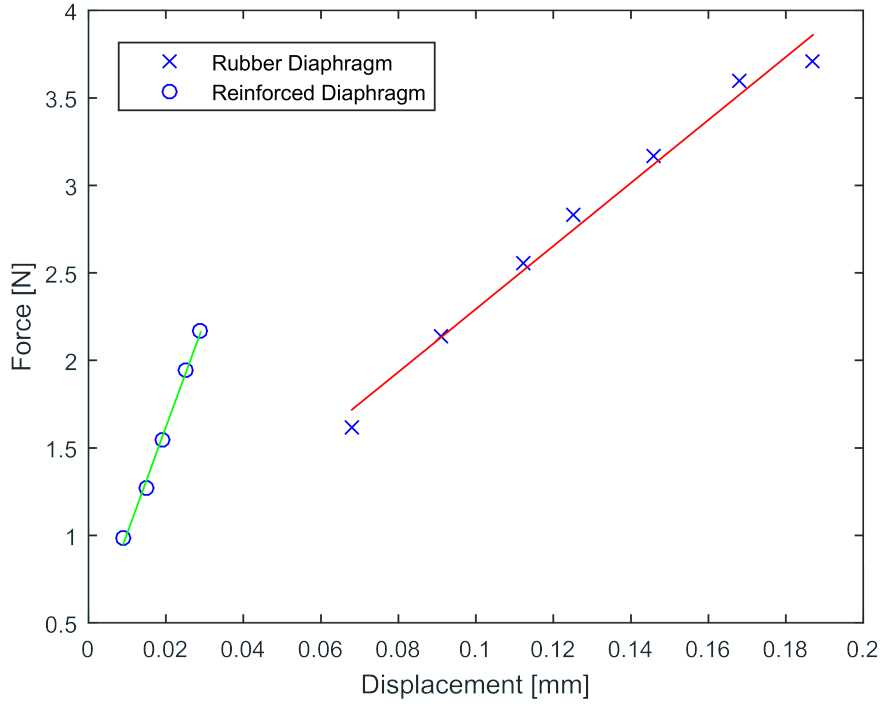


Figure 9.4: Stiffness Experiment Results, Single-acting Actuator

the retaining cap to keep the diaphragm from interfering with itself, and to keep it sliding freely through its range of motion. This helps maintain the convolution in the diaphragm, allowing it to roll on both the cylinder wall and the piston skirt. The first experiment sought to quantify the effect of fabric reinforcement, and to determine whether reinforcement was necessary for our relatively low-pressure application.

The experiment consisted of a pair of single-acting actuators connected back-to-back by a fluid line. One actuator had its Output Rod held constant, while the other actuator was manipulated. This end had its displacement measured by a laser encoder system (resolution approximately $0.6\mu\text{m}$ per count, post quadrature) and the applied force measured by a force gage. Multiple force-displacement pairs were obtained and a line of best fit calculated, whose slope gave the stiffness of the diaphragm system. Figure 9.4 summarizes the results of this experiment. We found that the fabric reinforcement tripled the stiffness (18kN/m unreinforced vs. 60 kN/m reinforced), and all further tests were done with reinforced diaphragms.

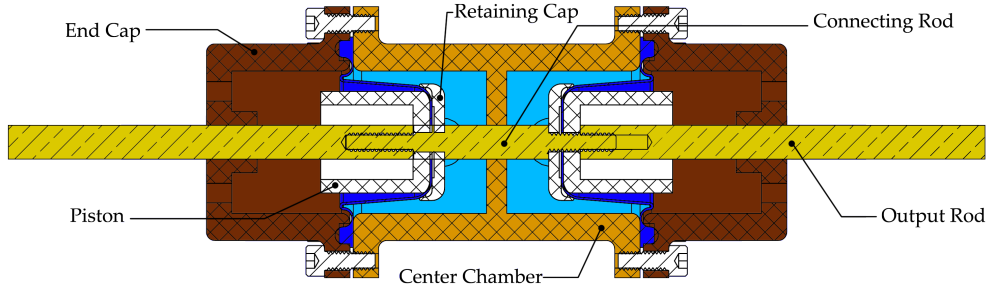


Figure 9.5: Double-Acting Diaphragm Actuator Design—First Iteration, Section

9.3 Double-Acting Diaphragm Actuator, First Iteration

With the independent diaphragm and actuator designs proved, and the necessity of the reinforcement process confirmed, we saw little use in continuing to develop the single-acting actuator, as our proposed application would require both push and pull force from the actuator, linear plastic springs are not readily available, and the inclusion of a return spring would compromise the natural haptic feedback offered by the system. Thus, work began on a double-acting actuator design.

The primary design consideration for the double-acting design was once again MR-compatibility, but other goals—such as compact packaging, haptic feedback, and no leakage—were also taken into account. The double-acting design would require two separate pistons, rigidly connected to each other to operate in tandem, and we desired an axial output. This overriding desire for axial output would later prove unhelpful, but that would not be known until after this design underwent testing. The final design consisted of a Center Chamber, consisting of back-to-back Upper Cylinders, with a center journal connecting them for the Connecting Rod to pass through to connect the two pistons. Two End Caps, loosely based on the Lower Cylinder part from the Single-Acting design again stabilized the Output Rods against buckling and side-force. A full schematic of the design is provided in Figure 9.5, and the realized design is shown in Figure 9.6.

The stiffness characterization was done identically to the Single-Acting design, with a blocked output rod, a laser encoder, and a force gage providing force-displacement data, from which the stiffness of the system was calculated. Full results from this experiment



Figure 9.6: Double-Acting Diaphragm Actuator Design—First Iteration, as Manufactured

are provided in Figure 9.7. This experiment showed a system stiffness somewhere between the unreinforced Single-Acting system and the reinforced Single-Acting system, despite reinforced diaphragms being used in the Double-Acting design. The working theory was the pressure difference developed between the two chambers during the stiffness test was forcing fluid through the central journal connecting the chambers, which was nominally blocked by the connecting rod, but high pressure fluid finds a way. It was also during this test that we discovered the primary failure mode of our custom reinforced diaphragms. When exposed to high pressure, the rubber delaminates from the mesh reinforcement, creating an unreinforced region (a tumor, if you will) that ruptures on the next application of the pressure load. This failure is illustrated in Figure 9.8. Despite being lower than expected, this stiffness (33kN/m) was sufficient for our application, so further testing proceeded.

The experimental setup was modified to include a second laser encoder and the second actuator's output rod was freed. The displacement of both the input actuator and the output actuator were concurrently measured, while the input actuator was put through its range of motion. The results of this experiment are given in Figure 9.9. This experiment shows a roughly one-to-one correspondence between the input actuator position and output actuator position, and little to no hysteresis in the system. With these basic tests accomplished, it was time to test the haptic feedback capability of the system.

To test this, a special phantom was prepared with a pork rib contained within the gelatin. A clinician trained in MR biopsy and ablation would operate the input actuator, while a needle was attached to the output actuator, placed in the MR bore with the pork phantom.

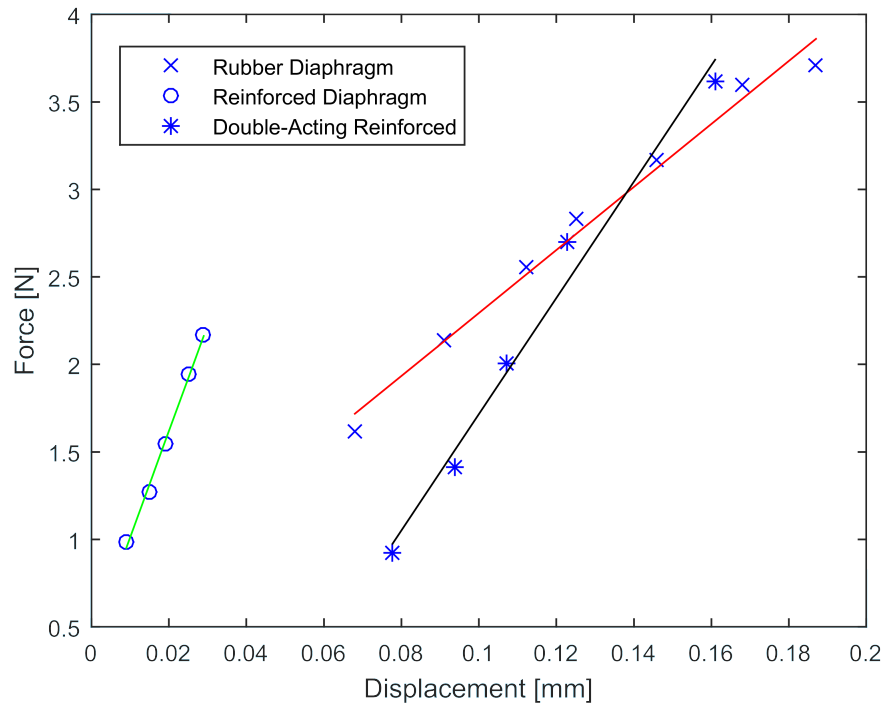


Figure 9.7: Stiffness Experiment Results, Double-Acting Diaphragm Actuator—First Iteration

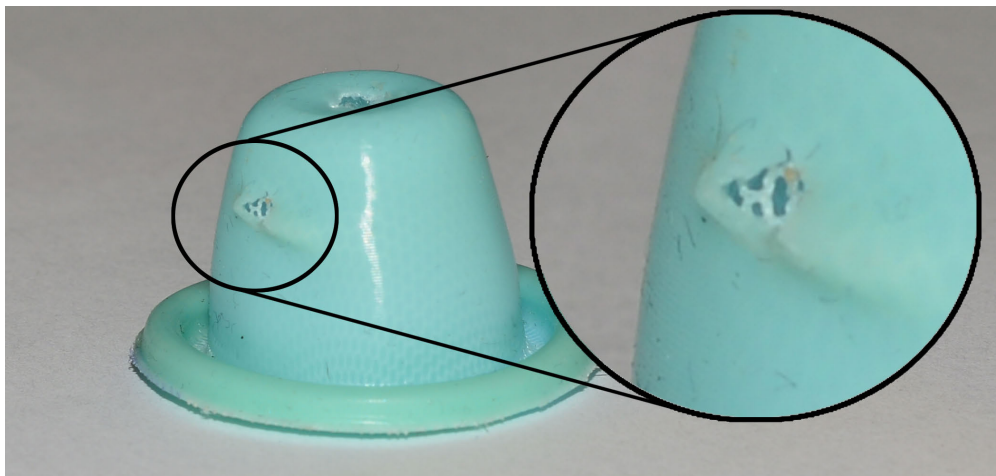


Figure 9.8: Failure Mode of Custom Reinforced Diaphragms

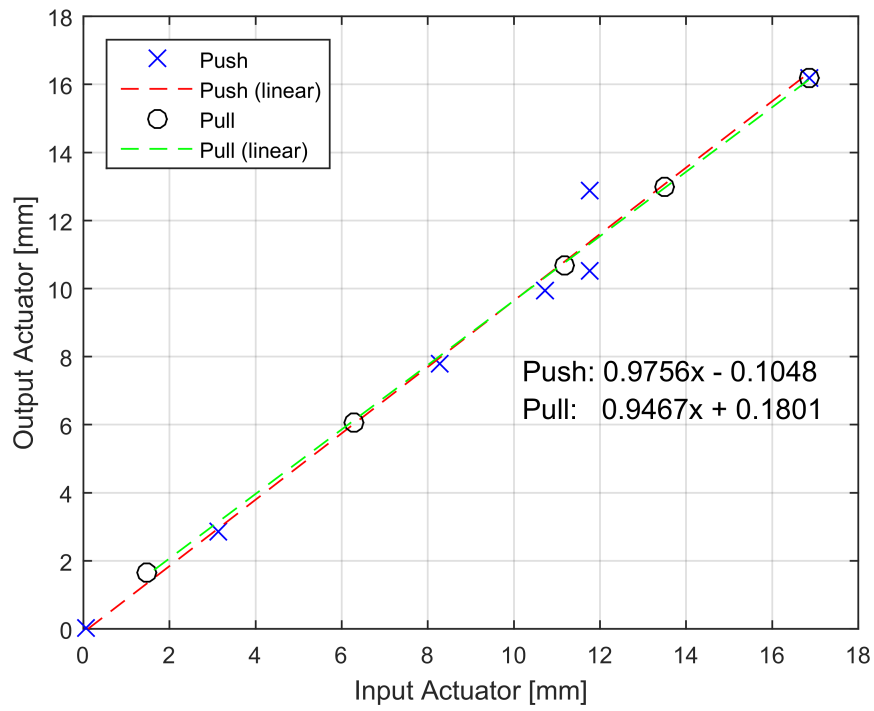


Figure 9.9: Input-Output Displacement, Double-Acting Diaphragm Actuator—First Iteration

When the clinician felt the needle transition from gelatin to pork meat (and later, pork meat to bone), he would alert the experimenters, who would confirm the needle tip position with real-time MR imagery. Unfortunately, the clinician could feel neither transition—a result he attributed to a large “start-up” (stiction) force when positioning the input actuator. This result, especially when combined with the previous theory that the lack of stiffness is attributable to leakage between the two chambers, led us to abandon this design, as it forced a tradeoff between two important goals: sealing and stiction. Any attempt to make the center journal have less friction would result in more leakage and thus, less stiffness. A new design, one without this tradeoff, was deemed necessary.

9.4 Double-Acting Diaphragm Actuator, Second Iteration

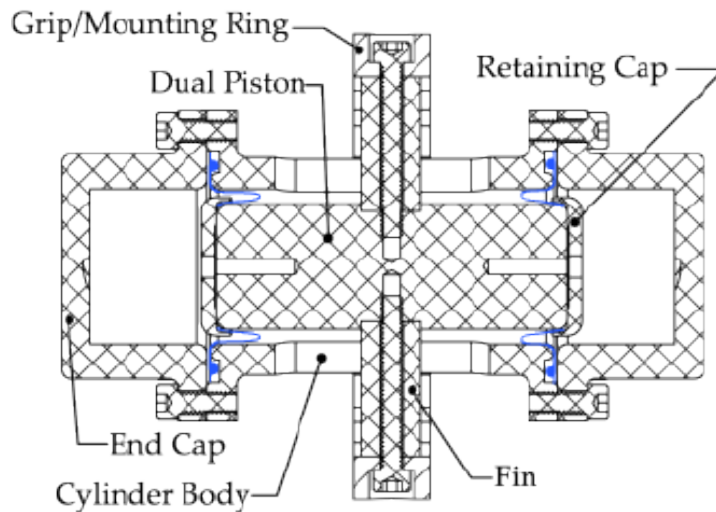


Figure 9.10: Double-Acting Diaphragm Actuator Design—Second Iteration, Section

After what we learned from the first iteration, priority in designing the second iteration went to eliminating the center journal section of the previous design. It had compromised the two largest advantages of the rolling diaphragm: low friction and complete seal throughout the stroke. This led to switching the cylinders from a “facing inward” configuration to a “facing outward” configuration, with the tandem pistons in the center. This allowed a complete at-all-times seal of the two cylinders without trading sliding friction. The two pistons were



Figure 9.11: Double-Acting Diaphragm Actuator Design—Second Iteration, as Manufactured

then combined into a single part, with piston-shaped ends and attachment points for four “fins” that would connect to an outer ring to transmit the motion and accept attachments. The fins also serve as linear bearings to counteract over-torquing of the diaphragm in all directions, keeping the stroke direction axial. A large amount of clearance was left between the fins and the slots they fit into, so that during normal operation, the piston rides on the diaphragm alone with minimal contact between the fins and their corresponding slots. However, the fins are rectangular with rounded edges, so the flat sections can resist excessive torquing and restrict the motion of the output ring to one degree of freedom. A sectioned view of this design is given in Figure 9.10 and a photo of the completed actuators is given in Figure 9.11.

The piston, fins, compression fittings, and ring are all made from Delrin for its excellent machinability and sliding friction. The Cylinder Body and both End Caps were made of Acrylic, both for its sliding friction properties (for the slots in the Cylinder Body) and for its transparency (both). The transparent actuator is helpful in diagnosing diaphragm-related

issues, eliminating air, and is aesthetically pleasing. After manufacturing was complete, the standard battery of tests was run and since the results were promising, several more experiments that were not run on the first generation models were performed.

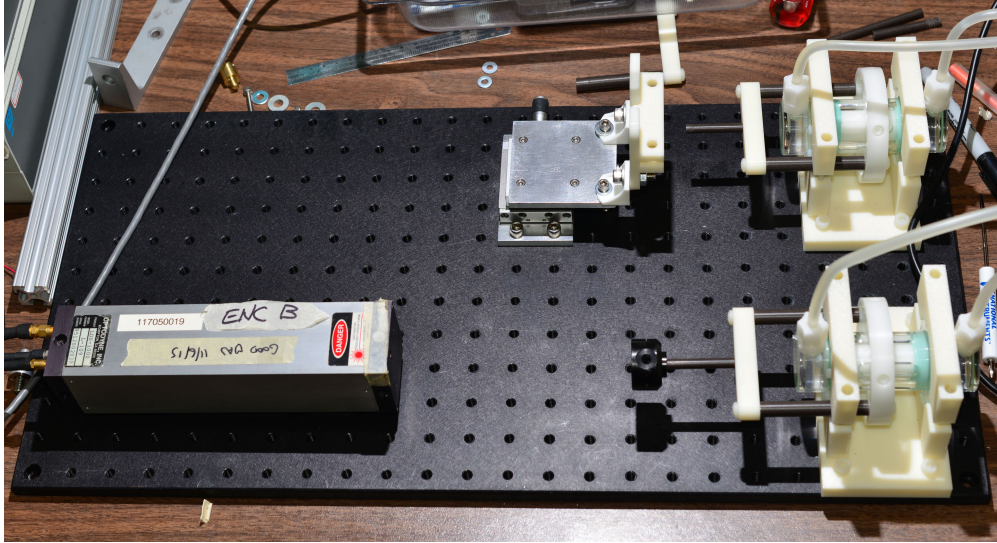


Figure 9.12: Characterization Experimental Setup

A general experimental setup was constructed, where the pair of actuators could be fitted with either a force transducer, a laser encoder retro-reflector, or both to perform several experiments in quick succession. Figure 9.12 illustrates the setup between experiments; a second laser encoder can be used in place of the linear stage upper right, and transducers can be attached to the axial output rods for force measurement. The actuators are held permanently in place, while different sensors can be attached as the experiment requires.

The stiffness experiment was repeated with this new pair of actuators, and results are given in Figure 9.13. A single laser encoder measured displacement at the input actuator, while the force imparted by the blocked output actuator was measured by a piezo-resistive force transducer. The stiffness of the system was found to be 10 kN/m, substantially softer than previous generations, and it is theorized that this is due to the compliance of the ring-fin-piston connection, which is held together with four long, plastic cap screws. A stiffer method for bonding the fins to the piston is in development, as the four fins and the piston would be a single, solid part but for assembly considerations.

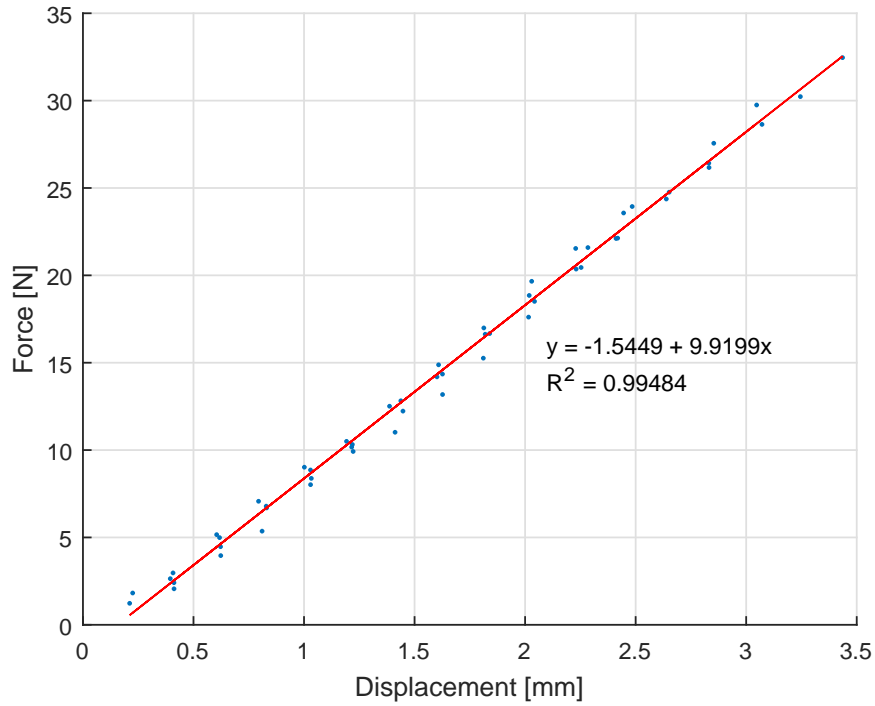


Figure 9.13: Stiffness Experiment Results, Double-Acting Diaphragm Actuator—Second Iteration

To show input-output linearity and one-to-one correspondence, a second laser encoder was added to the experimental setup and the output actuator was no longer blocked. The input actuator was moved through its range of motion, while gathering position data from both the input and output actuators, sampled at regular time intervals. The results of this experiment are given in Figure 9.14, which shows a one-to-one correspondence between input and output, and additionally very small spread, as evidenced by the goodness-of-fit coefficient from the linear fit. While random points are sufficient to prove one-to-one correspondence in steady-state, a cycle must be done to show hysteresis.

To experimentally determine the hysteresis curve of the system, the system was put through repeated cycles covering the range of motion, and position data was continuously sampled. One cycle consists of moving the input actuator from the lower limit of its range to the upper limit of its range, and then back. Data from this experiment is presented in Figure 9.15, and it is clear that the system does not have strong hysteresis.

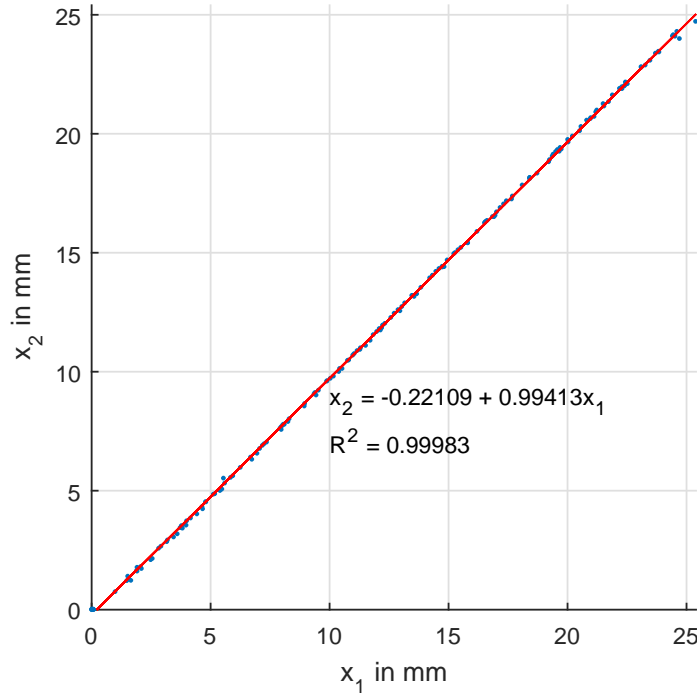


Figure 9.14: Input-Output Displacement, Double-Acting Diaphragm Actuator—Second Iteration

Another quantity of interest in characterizing this system is the delay between input and output actuator. To experimentally determine this, the input actuator and output actuator were continuously measured by the laser encoders while the input actuator was manipulated in a step-like fashion. Several trials were performed and the results averaged; one such trial is shown in Figure 9.16. The average delay between input and output (with our current fluid line length of two meters) was approximately 100 milliseconds. Further experiments are required to determine the effect of fluid line length and line preload pressure on this delay.

The final property of these actuators that was tested was the force transmission between input and output actuator; this is a predictor of haptic feedback capability. The experimental setup consisted of blocking one actuator's output through a piezoresistive force transducer, while applying force (through another force transducer) at the input side. The input and output forces are plotted against each other in Figure 9.17, which shows a linear—and more

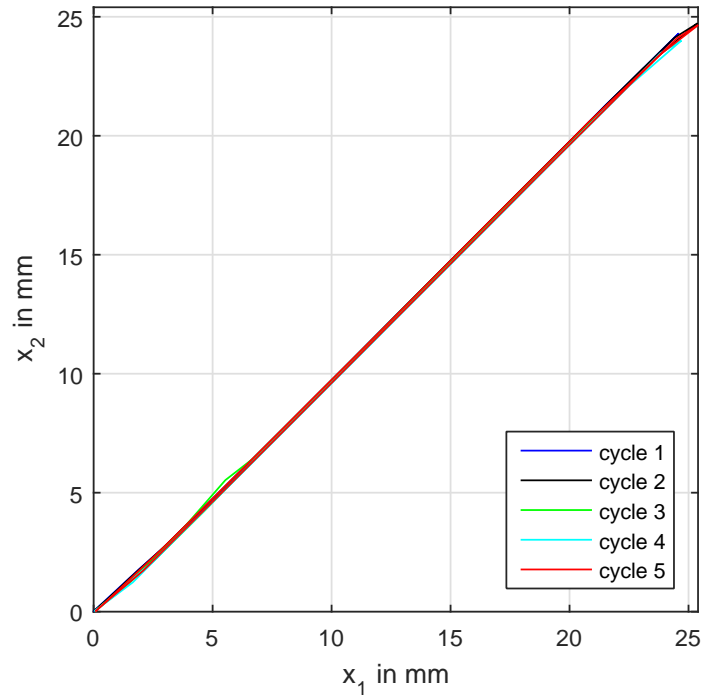


Figure 9.15: Hysteresis Loop, Double-Acting Diaphragm Actuator—Second Iteration

importantly, unitary—relationship between input and output force. We believe the spread in the points to be the result of hysteresis and sideload in the sensors.

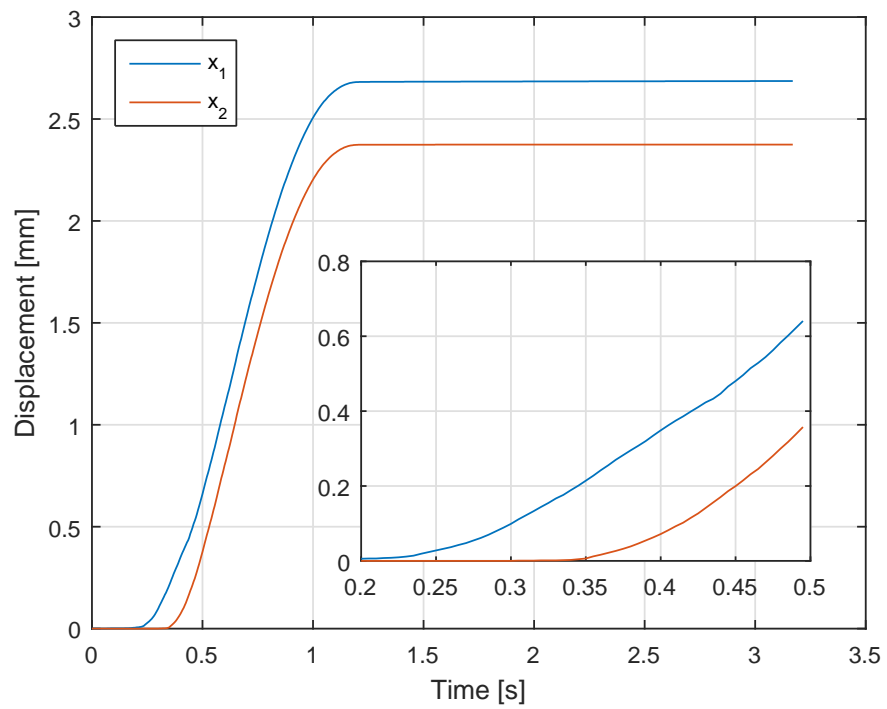


Figure 9.16: Input-Output Delay Estimate, Double-Acting Diaphragm Actuator—Second Iteration

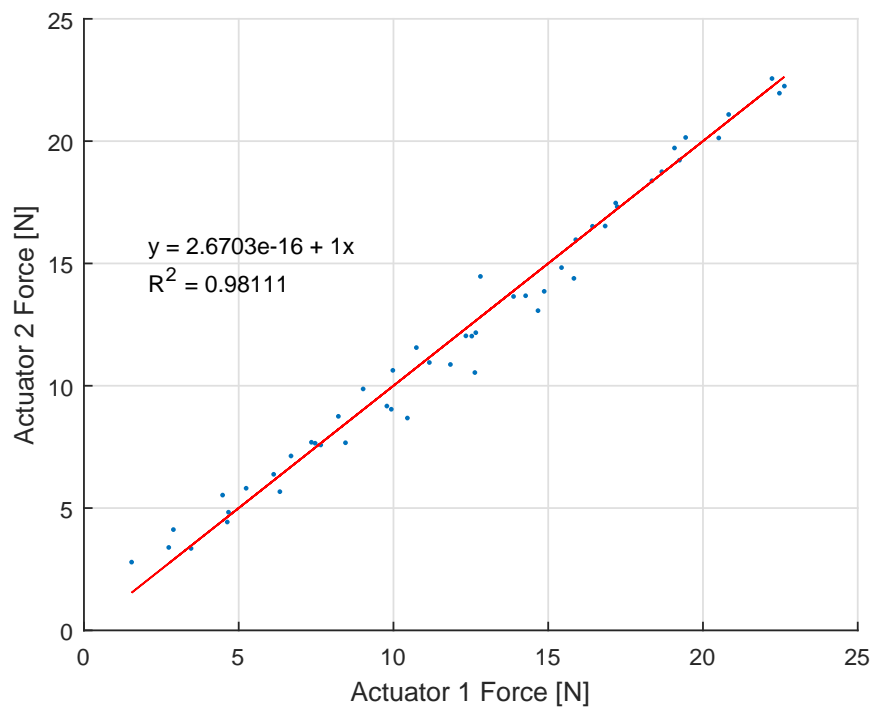


Figure 9.17: Force Transmission, Double-Acting Diaphragm Actuator—Second Iteration

CHAPTER 10

Application: An MR-Compatible Stage for Respiratory Motion Emulation

10.1 Introduction

Since MR-guided interventions are an area of active research, there is a need for physicians to refine their techniques and for MR scientists to create new sequences to provide the physicians with better imagery. To do this, it is necessary to simulate the conditions of the patient in both cases; phantoms simulating various body areas are available commercially, and it is common to use a “gel phantom” made of gelatin or agar to simulate flesh, but these are stationary. While it is possible to keep a patient virtually stationary by holding their breath, there is a time limit to this technique, and it is inherently not repeatable from trial to trial, or from patient to patient. When breathing normally, data collected from human subjects shows that internal structures can move in excess of 50 millimeters over the course of a breath. This presents issues for both the physician and the MR scientist—the physician must hit a moving target, and the MR scientist must contend with artifacts introduced into the image by the breathing motion. It is clear that simulation of the respiratory motion is necessary to proper development of MR imaging and interventional techniques.

A robotic system can provide three critical advantages over the traditional animal study: a robot is *repeatable*, so that the MR scientist can isolate changes in the motion as a variable and focus exclusively on the scan parameters; a robot is *configurable* so the physician can simulate patient-to-patient variability when necessary, but also have the freedom to exploit the repeatability of the system to hone the technique; and, a robot is *convenient*—a robot requires no additional personnel like a live-animal study, and has no ethical concerns or

oversight required.

However, the MR environment itself poses substantial challenges to the implementation of such systems. Due to the high magnetic fields present at all times in the scanner bore—between 1.5 and 3T—any ferromagnetic components, or electromagnetic actuators and sensors are prohibited due to safety concerns. In addition to the safety issues, they also introduce artifacts that degrade the imagery obtained from the scanner. These concerns alone eliminate the most common actuation/sensing modalities and engineering materials out-of-hand, complicating design of the robotic system. To resolve this, Drangova [DBP96] developed a remotely actuated MR-compatible motion phantom which can achieve not only bulk rotation and translation, but also axial and rotation shear motion. Sternberg [SHY10, SHZ12] designed a 5 DOF phantom mimicking the left ventricle using a similar extended structure reaching in the scanner. Cai [CCW11] used the same remote motor actuation concept to build a dynamic phantom simulating tumor motion and the body surface motion. Different dynamic phantoms are also commercially available: Modus Medical Devices [Mod16] has a wide variety of respiratory motion phantoms; Shelly Imaging Technologies [She16] develops a multi-modality respiratory tumour motion phantom; dynamic thorax phantom of CIRS [Com16] can be used for image acquisition, treatment planning, and dose delivery studies. It is noticed that the afore-mentioned work use stepper motors as the direct drive for their open-loop control precision and repeatability; however, there are several disadvantages with this approach: The motors need to be well shielded and secured at a safe distance; rigid connection for motion transmission will take up inflexible space and make the demand in component precision stricter; the phantom motion precision can also be compromised since the dynamics from the motor shaft input to the actual phantom motion output are totally neglected. Gullans [GOR09] proposed to use a motor driven hydraulic system as a dynamic heart phantom, wherein linear XYZ motion, rotation, and internal pressure of the phantom can be generated. Based on Gullans’ work, Kee [KLP10] modified the design and demonstrated the feasibility of the platform as a moving phantom by closing the position control loop of a 1 DOF prototype using fiber optic sensors. Nonetheless, the characterization of the actuator and the capability to reproduce the motion have not yet been reported.

Unlike currently-available systems, the device presented in this work was designed from the ground up to be strictly MR-compatible—that is, no ferrous materials or electromagnetic actuators present in the exam room. Our device makes use of a hydraulic transmission of force and displacement from a master actuator placed outside the exam room to a slave unit placed in the scanner bore. Because of this indirect transmission, we expect dynamics to arise from both the hydraulics and the mechanisms coupling them to the input and output stages. We will present three control schemes: inner-loop PI on the master side only, data-based feedforward dynamic inversion, and an Iterative Learning Control (ILC) scheme using the aforementioned dynamic inversion as its learning filter.

In this work, we present the following:

1. The design and verification of an MR-compatible device to emulate respiratory motion
2. Comparison of three control strategies to track respiratory motion recorded from a human subject
3. Preliminary results from a modified system to increase stroke

10.2 System Design

The system presented herein is comprised of three major mechanical subsystems: the actuators, the slave unit (Phantom Platform), and the master unit. The actuators are those presented in Chapter 9, with no major modifications made for this application, as they were already designed with it in mind. The slave unit will be placed in the MR bore, and is thus subject to all constraints of MR-compatibility. The master unit, however, will be placed in a room adjacent to the scanner room, so most of the design constraints (especially the ban on ferromagnetic materials) can be relaxed. A schematic of our system setup is given in 10.1.

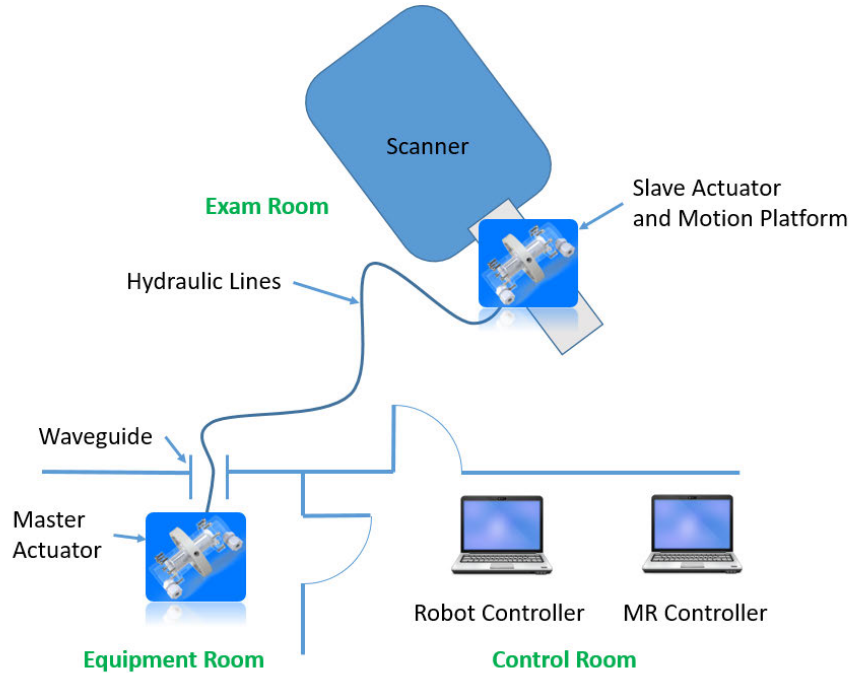


Figure 10.1: System Schematic

10.2.1 Slave Side— Phantom Platform

Two variations of the Phantom Platform will be presented in this work: the majority of the results are from the first prototype, which features a 1:1 transmission of motion from master to motion platform; later, preliminary results will be given from a later iteration adding a mechanical amplification scheme to increase the transmission to 2:1. Both versions use the same basic design, with the amplification method added later as a bolt-on system.

Practical considerations in mounting the actuator to a mechanism required that the strict omission of all metals followed in the actuator design be relaxed somewhat. However, plastic parts were chosen wherever possible to minimize the usage of metals, and no ferromagnetic materials were used. The base plate of the stage was designed to mate with the scanner bed through a set of slots that accept the same straps used to secure the body coil, allowing the stage to be mounted anywhere along the bed. An additional set of slots, rotated 90 degrees, allows the stage to be mounted with its axis of motion either parallel to the axis of the scanner or transverse. The slave actuator is fixtured to the base plate and attached to

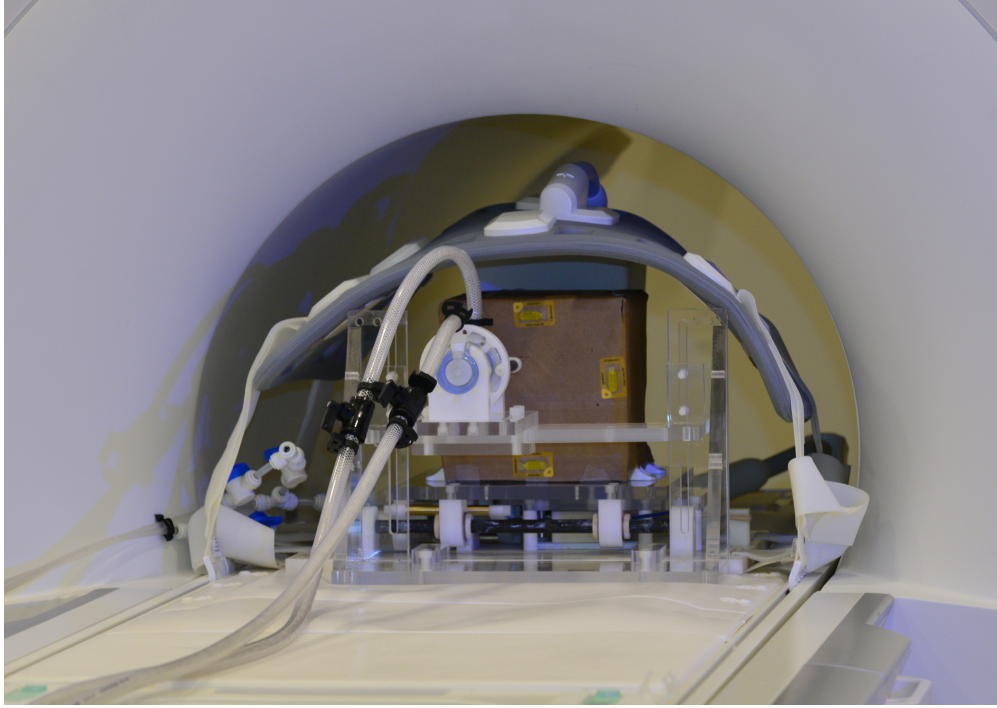


Figure 10.2: System participating in a Needle Targeting Experiment

a linear guide to serve as the external bearing. In the 1:1 design, the moving stage plate is directly attached to this slide; in the 2:1 design, it houses a pulley, and the stage is connected to the actuator through a cable.

The moving stage plate slides on a pair of carbon fiber rails through four linear guides, and features hard attachment points for the gel phantom. A custom gel phantom was created to mount to the stage, and features an adjustable target plate that can be sunk various depths into the gel. This provides a repeatable set of targets for imaging or interventional studies.

Examining the acquired profiles, it became clear that the actuator's design stroke of 25 mm would be insufficient. To increase the stroke of the device, a pulley mechanism was designed to mechanically amplify the stroke of the actuator by a factor of two with a minimum of backlash and friction. This involved fixing one end of the cable to the base plate, and the other to the moving stage plate. The cable passes around a pulley held in the linear slide attached to the actuator, and around two idlers to redirect the tension force to the horizontal center of the moving plate, as to avoid creating unnecessary torques and loads on the linear guides. Since a pulley system has an inherent directional preference, a return

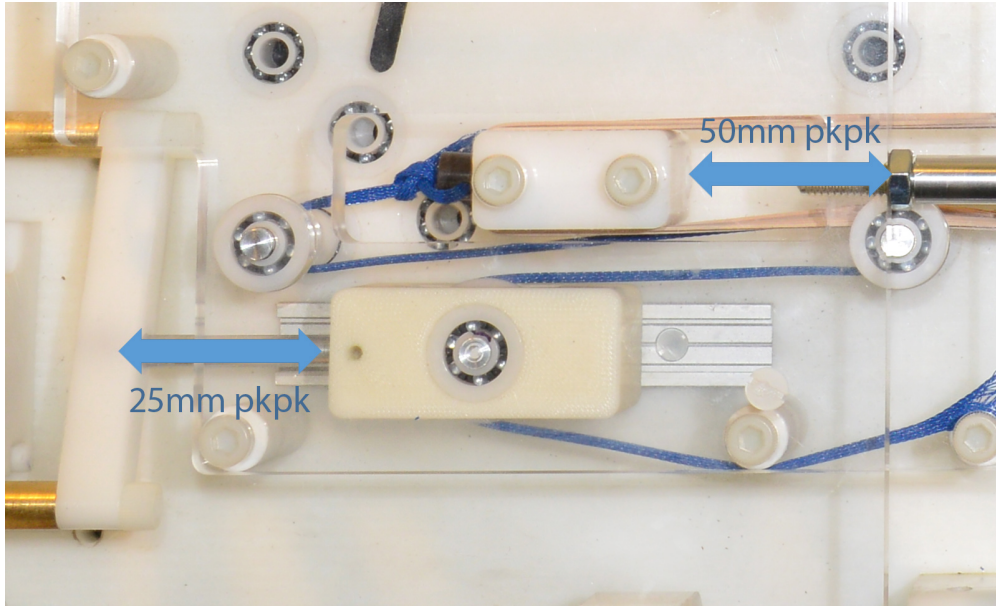


Figure 10.3: Bolt-on Mechanical Amplifier

mechanism must be added to provide force in the other direction. We elected to make use of elastic cord as a return spring, anchored to the base plate. The spring constant and preload distance were chosen so to balance the competing goals of keeping tension in the cable at one extreme, and not overtaxing the master-side drive motor's torque requirements at the other. Figure 10.3 describes the bolt-on amplification mechanism.

10.2.2 Master Side

Because it will be placed outside the exam room, the sole design requirement of the master unit is to drive the slave unit. Because the slave unit is preloaded, and it is planned to accommodate an additional payload, a high torque input is required. The selected motor has a gear ratio of 86:1, which can provide sufficient torque without requiring high duty cycle from the motor. As indicated in Figure 10.4, the torque output is transmitted through a rack and pinion mechanism to the master actuator. This mechanism was chosen for its simplicity and compactness. The moving part, where the linear rack is attached, is secured to a pair of linear guides, which can provide proper constraint of the motion with a minimum of friction. Note also that the linear guide is held by four struts so that the gear teeth are

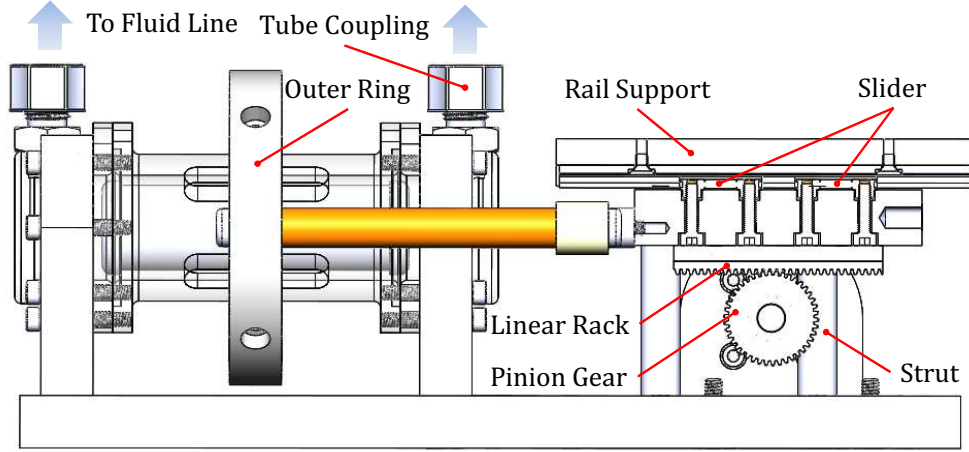


Figure 10.4: Master Unit Design Schematic

always in mesh regardless of torque output. The motion is then coupled to the outer ring of the master actuator by a pair of parallel rods as to serve as the required external linear bearing for the master unit.

10.3 Experimental Setup and Control Implementation

Different respiratory profiles recorded from a 3T MRI system (MAGNETOM Prisma, Siemens, Erlangen, Germany) will be deployed and the performance is evaluated on the slave unit. It is anticipated that a direct servo-loop on the master unit can only achieve limited performance because of the inherent time delay in the fluid network, and the non-smooth factors of the system, such as backlash and input deadzone. Therefore, a data-based feedforward filter and an iterative learning algorithm will also be introduced to genuinely replicate the motion.

The respiratory motion trajectory is extracted from real-time MR images using image-based tracking. On the upper abdominal MR images (Figure 10.5), we selected the interface between liver and diaphragm as the feature (white) to track and specified the tracking search range (blue). An intensity-based multi-resolution registration algorithm with a least-squares metric is applied to extract rigid-body motion of the feature throughout respiration [WGH13].

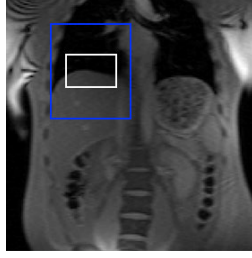


Figure 10.5: Sample Abdominal MR Image for Tracking

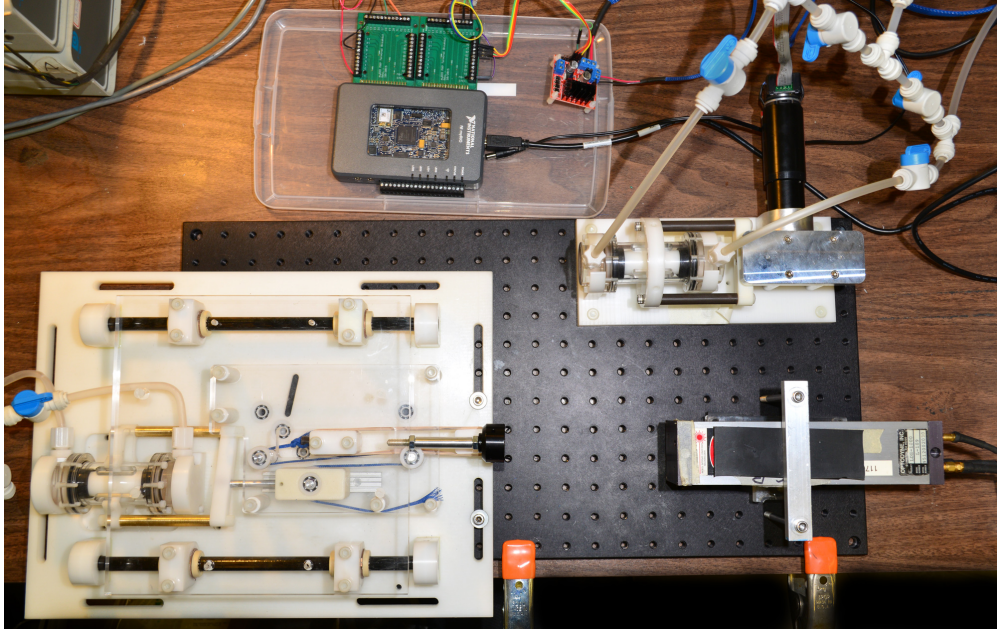


Figure 10.6: Tracking Experimental Setup

10.3.1 Experimental Setup

The experimental setup is depicted in Figure 10.6: both the master unit and the driving unit are mounted on an optical table. A retroreflector is attached to the slave unit and through which the displacement is measured by a laser encoder with $0.635 \mu\text{m}$ resolution. A real-time target (National Instruments myRIO) serves as the motion controller, and runs at a 200 Hz loop rate. This target was chosen for its low cost and I/O flexibility; our control schemes feature offline computation, and are thus unaffected by its relatively low specifications.

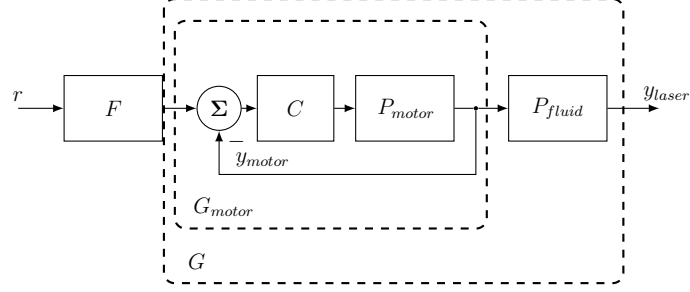


Figure 10.7: Feed-Forward Controller Structure

10.3.2 Control Implementation

10.3.2.1 Data-Based Feedforward Controller

In order to improve the tracking performance on the slave unit, a data-based feedforward filter is used to incorporate the dynamics of the fluid transmission as in Figure 10.7. The design method [CT16] is briefly reviewed as follows: Firstly, a reference model M , a zero-phase low-pass filter with d steps delay, is chosen to be an approximate of an ideal impulse function:

$$G(z)F(z) \cong M(z) \quad (10.1)$$

where $G(z)$ is the discretized overall dynamics of the pre-stabilized motor plant cascaded by the fluid transmission, and $F(z)$ being the plant inversion.

An impulse response $r(k)$ generated by the reference model $M(z)$ is then used for an iterative learning process, wherein a simple P-type or PD-type learning filter can be used. When the process achieves convergence, the product of $G(z)$ and converged control signal u_∞ approximates the reference model $M(z)$:

$$G(z)u_\infty(z) \cong r(z) = M(z) \quad (10.2)$$

and this implies a stable FIR inversion can be approximated by the converged u_∞ :

$$F(z) \cong u_\infty(z) \quad (10.3)$$

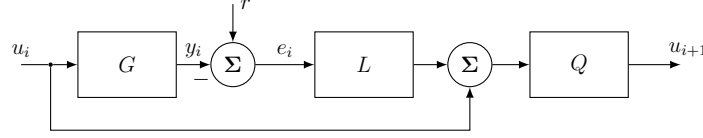


Figure 10.8: ILC Controller Structure

10.3.2.2 Inversion-Based Iterative Learning Control

Iterative learning control (ILC) has been known for its feasibility to perform repeated tasks. ILC can also tolerate a certain amount of time delay [Hid95, Hid96] and nonlinearities [XXL05] in the system. In this particular application, the feedforward nature of ILC lends more tractability since the system can completely be trained offline and no additional MR-compatible sensor is required on the end-effector.

A typical ILC block diagram is represented in Figure 10.8. As can be seen, the learning error e_i from the previous iteration i is fed through a learning filter L , and is then used as a correction term to generate the control command for the next iteration $i + 1$. A low-pass filter Q might be used together to suppress the high-frequency unmodeled dynamics. To summarize, the ILC learning law is as follows:

$$u_{i+1}(z) = Q(z)[u_i(z) + L(z)e_i(z)] \quad (10.4)$$

The stability condition of ILC algorithm can then be written in the following inequality [BTA06b]:

$$\|Q(z)[1 - L(z)G(z)]\|_\infty < 1 \quad (10.5)$$

where the left hand side of the inequality constitutes the convergence rate of the learning error.

It is noted that if the learning filter L well approximates the plant inversion of G , the convergence rate is nearly zero within the bandwidth of Q , which means the error settles to zero in one iteration. The fast convergence rate and a small learning error motivates the use of the plant inversion F as the learning filter.

In this work, the data-based inversion from the previous section can readily be used for the inversion-based ILC algorithm. Since the reference model has already incorporated a

low-pass filter, the update law 10.4 can be modified as the following:

$$u_{i+1}(z) = Q(z)u_i(z) + z^d F(z)e_i(z) \quad (10.6)$$

where d steps look-ahead are used to compensate for the group delay inherited from the reference model M . It is worth noticing that the offline computation eases the hardware requirements, and thus makes the use of the higher order data-based inversion more appealing.

10.4 Experimental Results

10.4.1 Actuator and System Verification

To verify the design goal of strict MR-compatibility, various benchmark phantoms were scanned on a 3T MRI system (MAGNETOM Prisma, Siemens, Erlangen, Germany) under the following three configurations: system removed, motion enabled, and motion disabled. Images from each scan are given in Figure 10.9, and a table of computed SNR and image distortion measurements is given in Table 10.1. We found no significant SNR effects or distortion introduced by either the stationary or moving system.

10.4.2 Tracking Results

With the system's MR-compatibility verified, all further testing was conducted on the benchtop. First, the naive master-side PI-only scheme was tested on a reference profile. Results are given in Figure 10.10. It can be observed that the tracking performance is poor, especially at the direction changes, and there is a large uncompensated group delay. It is clear that the hydraulic system has dynamics that must be accounted for. Next, the feed-forward dynamic inversion is applied (Figure 10.11). The group delay is compensated, but the tracking at the direction changes is not significantly improved over PI. We then applied ILC with the same dynamic inversion as the learning filter, which resulted in much improved tracking performance (Figure 10.12). The convergence plot for ILC is given in Figure 10.13. Results from these experiments are summarized in Table 10.2. System repeatability was verified by

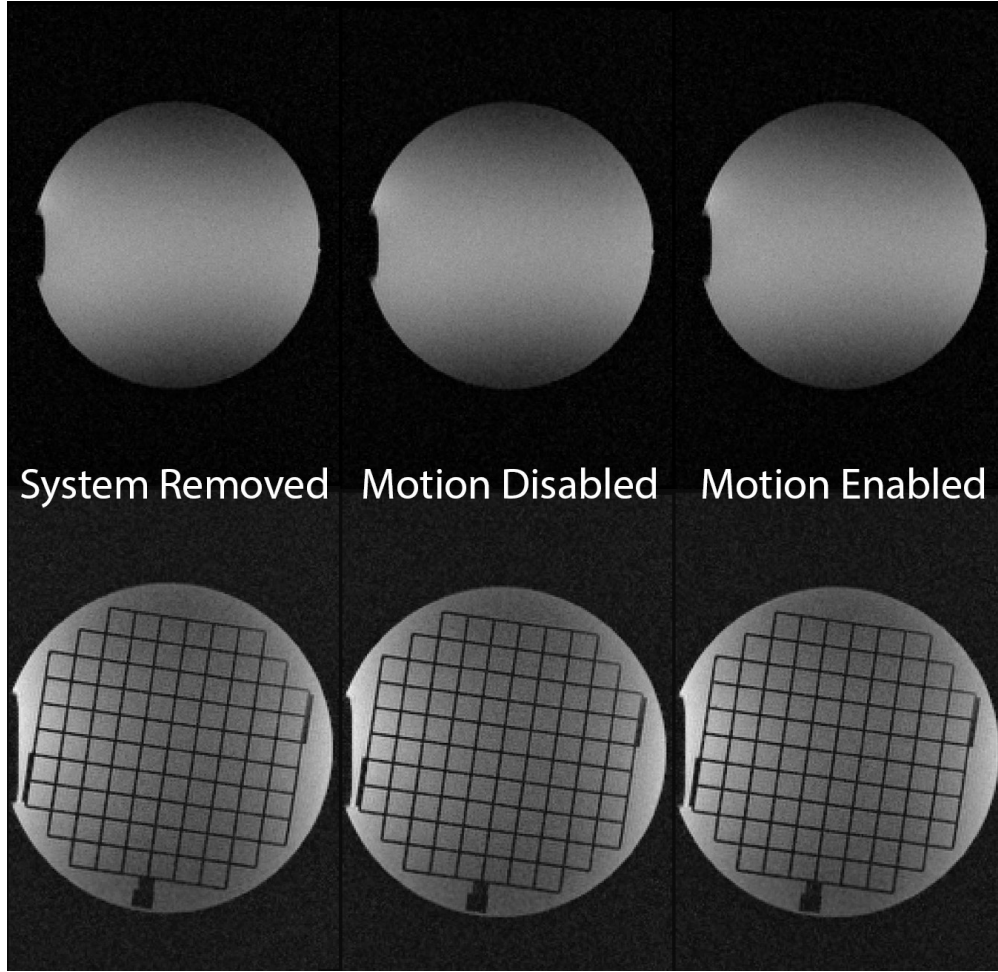


Figure 10.9: MR-compatibility of Bore-side System

running the learned feed-forward reference to the master’s inner PI loop various times over the course of a 24-hour period. For all tests attempted, the tracking performance was similar to the original result shown below in Figure 10.12.

With the promising results from the unamplified system, we began to experiment with the mechanically-amplified motion platform. A different, larger-amplitude profile was selected for training, and the results are shown in Figure 10.15. Having seen its superiority, we implemented only the inversion-based ILC controller on the amplified system. The preliminary results achieve sub-millimeter tracking, which is adequate for the application, but an examination of the spectrum of the error signal suggests that an inversion with higher bandwidth may be able to achieve performance comparable to the unamplified system.

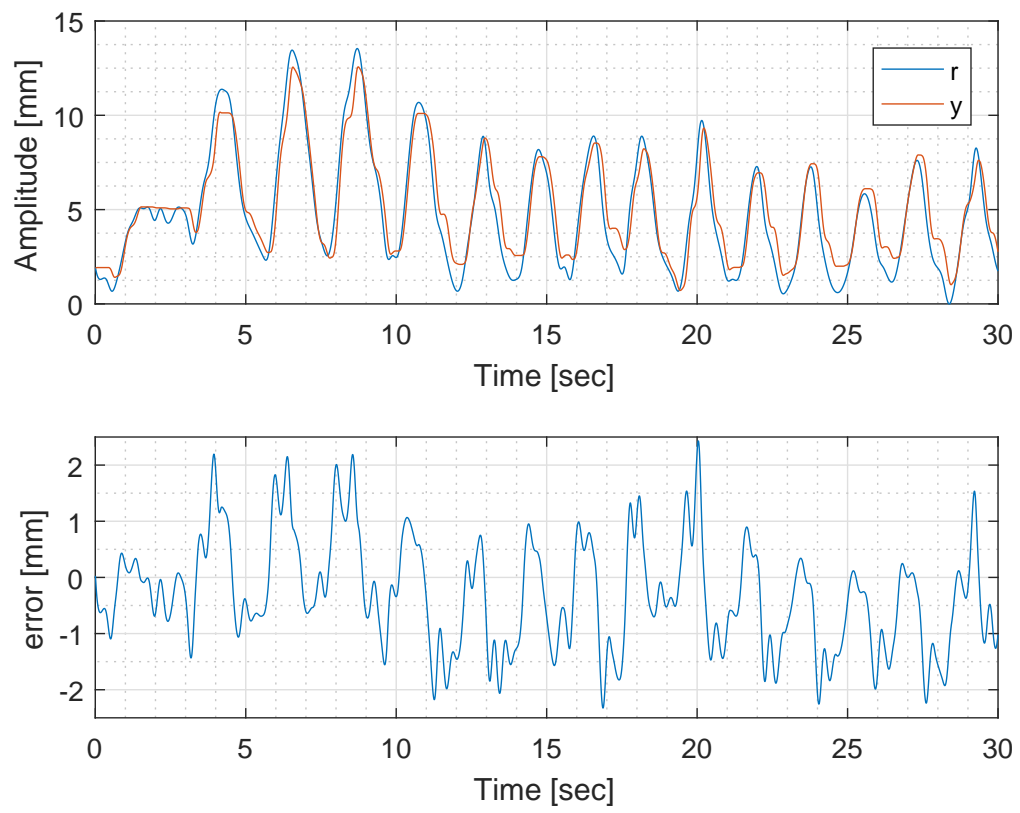


Figure 10.10: Master-side PI tracking Results

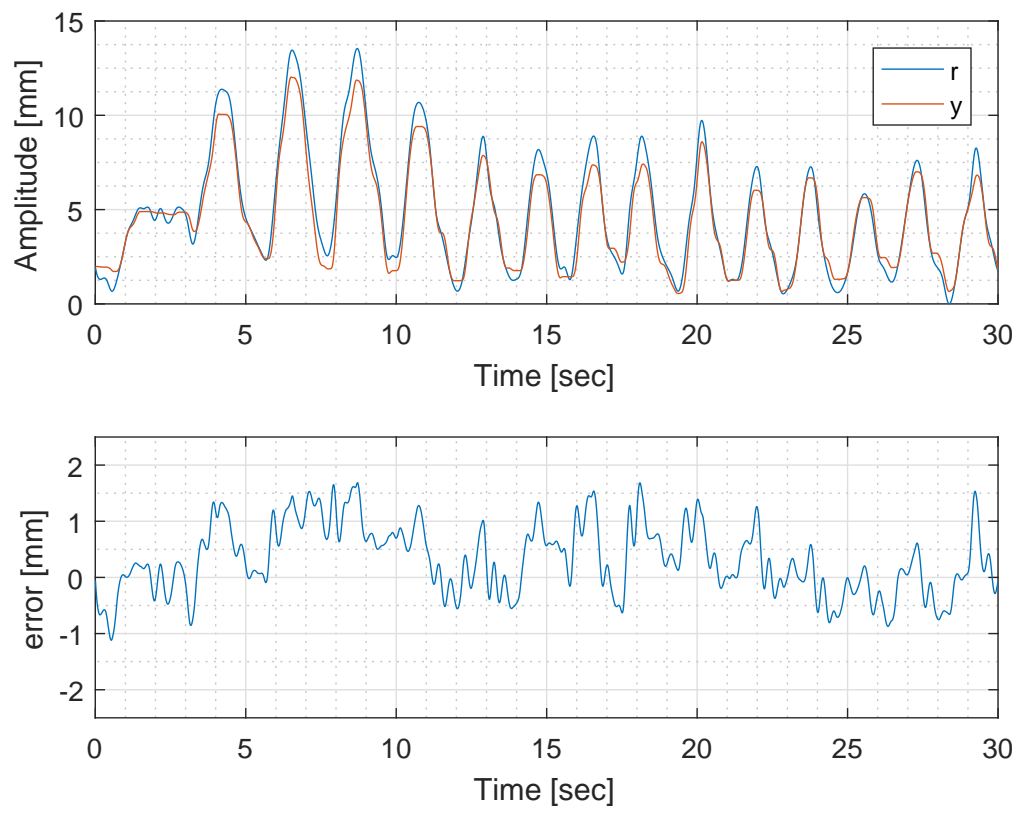


Figure 10.11: Feed-forward Inversion Tracking Results

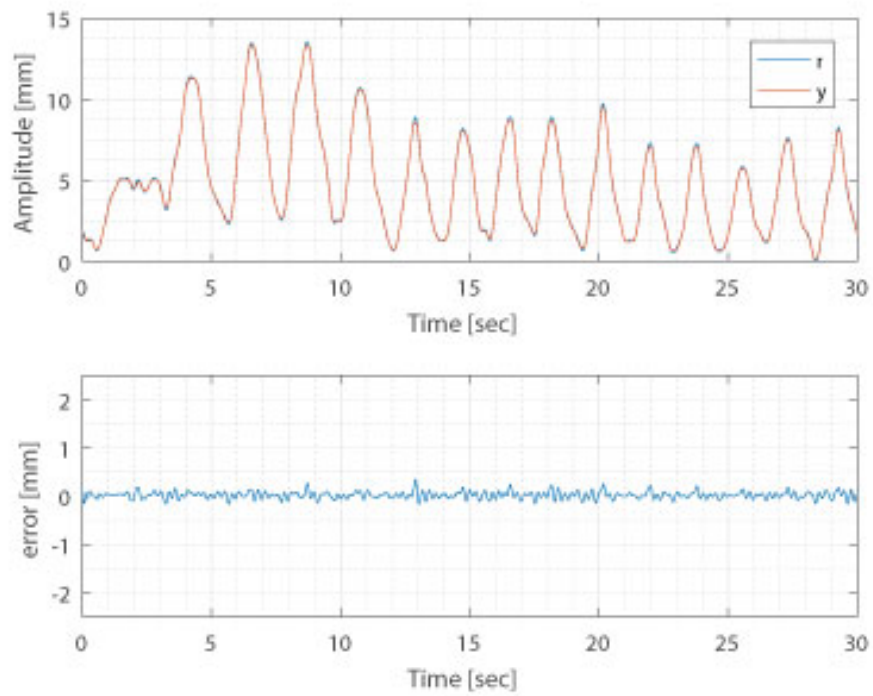


Figure 10.12: Inversion-based ILC Tracking Results

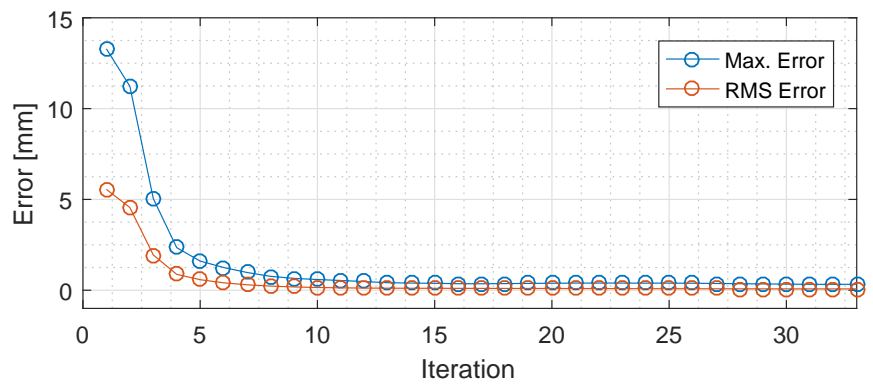


Figure 10.13: ILC Convergence Plot

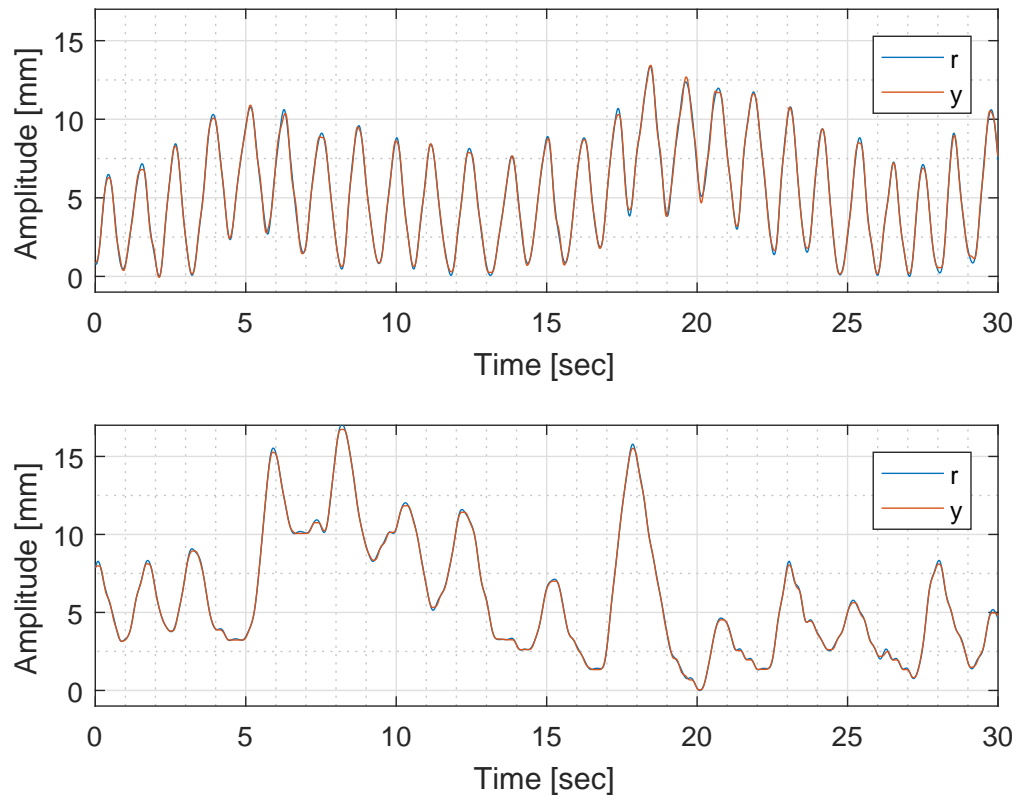


Figure 10.14: Additional Profiles Tracked

SNR

Configuration	Value	Change
System Removed	12.802	–
Motion Disabled	12.719	0.695%
Motion Enabled	12.713	0.648%

Distortion

Configuration		Value [cm]	Change
System Removed	Vertical	15.127	–
	Horizontal	15.170	–
Motion Disabled	Vertical	15.144	0.112%
	Horizontal	15.132	0.251%
Motion Enabled	Vertical	15.042	0.562%
	Horizontal	15.183	0.086%

Table 10.1: MR-compatibility of Finished System

Controller	RMS Error [mm]	Max. Error [mm]
PI Only	0.973	2.430
Feed-forward	0.652	1.687
ILC	0.072	0.328
ILC (amplified)	0.198	0.664

Table 10.2: Summary of Control Results

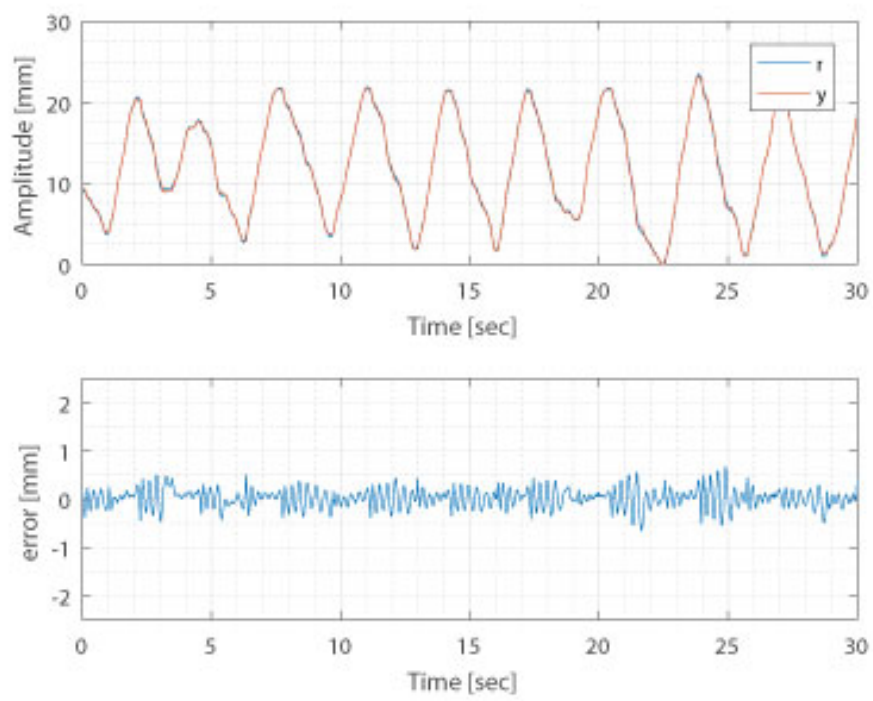


Figure 10.15: Preliminary ILC Results for Amplified System

10.5 Conclusions

In this work, we have developed and demonstrated a strictly MR-compatible system capable of tracking prerecorded respiratory motion trajectories. We present the following results:

- A fully MR-compatible, repeatable, mechatronic system capable of 25mm travel in one degree of freedom
- Experimental results from the implementation of three control strategies: master-side PI only, feed-forward dynamic inversion, and inversion-based Iterative Learning Control—the latter two demonstrating feasibility of feed-forward methods in this application
- Tracking results from additional profiles with varying bandwidth to demonstrate system flexibility
- Preliminary tracking results from a prototype system with mechanical stroke amplification, capable of 50mm travel

Future directions for this research include the refinement of the mechanically-amplified prototype and the exploration of in-bore applications for this device (e.g. manual or automated tracking and targeting of simulated lesions).

CHAPTER 11

Fluid Networks and Control

This section will first cover the general fluid network concept, then verify experimentally the system’s collaborative capability, and finally present work toward closed-loop operation with the MR images serving as position feedback.

11.1 Fluid Network Theory

To implement the co-robotic system described earlier, we have constructed a fluid actuator network— a variation on the master-slave configuration that features multiple master units. This architecture has many advantages, such as hardware blending of inputs, simultaneous haptic feedback capability between all units (each unit can “feel” the actions of all others), and an easy method of incorporating more units. Unlike pneumatic or hydrodynamic systems, there are no active components (pumps and valves) and the system is not required to run at high pressure. The basic equation governing the operation of this fluid network is

$$\sum_{k=0}^n d_k A_k + d_s A_s = 0 \quad (11.1)$$

where d_k denotes the linear displacement of each individual actuator k , d_s the displacement of the slave actuator, and A_k the piston cross-sectional area of each actuator. When multiple master units are actuated in tandem, many modes of co-robotic operation can be implemented. For example, consider the simple case of one master unit controlled by a human and sensed, one completely robotic master unit, and one slave unit. If the robotic unit follows the trajectory,

$$d_r = (1 - \alpha)d_h \quad (11.2)$$

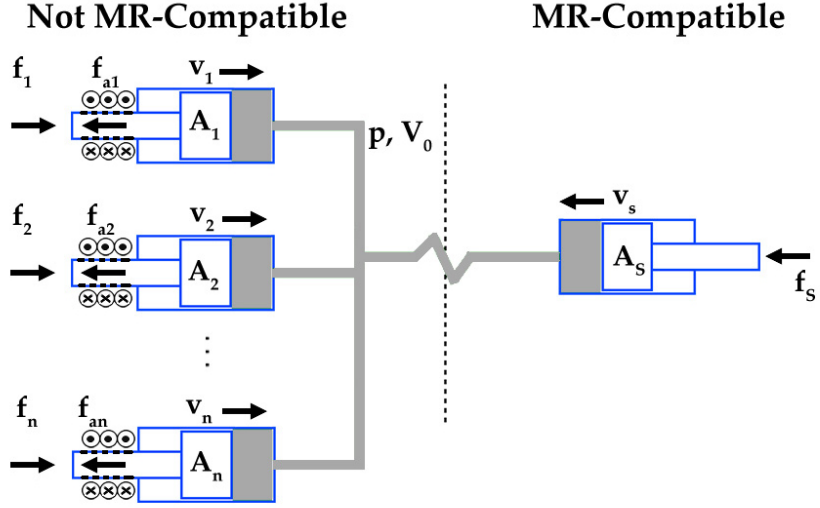


Figure 11.1: Fluid Network Concept

then the slave unit's output will be

$$d_s = \alpha d_h \quad (11.3)$$

This method can expand the precision available to beyond that which is usually seen in a manually-operated device by allowing the slave to perform fine manipulation from the human operator's gross manipulation.

Another mode of operation possible with the configuration above is a frequency crossover scheme, where the human unit is responsible for a certain frequency range of the desired signal, and the robot is responsible for the balance. This is implemented as

$$f_{a,h} = Qu(t), \quad f_{a,r} = (1 - Q)u(t) \quad (11.4)$$

where $u(t)$ is the desired total control input, and Q is a filter. This could be used to reduce hand tremors during manual operation, to task the robot with tracking of a moving target while still allowing the physician manual course correction, or to add a high-frequency vibration to the slave actuator's motion to aid in tissue penetration.

Another interesting mode of operation possible with this simple configuration is the virtual wall, where the human has full control until the output of the slave unit nears a restricted area (in the clinical application, an organ or bone). When this occurs, the robot

engages, negating any further human inputs that would drive the slave unit into the restricted area, effectively nulling the slave unit’s motion.

These three cases can be generalized to support more than two master units and arbitrary input strategies as follows:

$$f_{a,k} = Q_k u(t), \quad \sum_k Q_k = 1 \quad (11.5)$$

where each Q_k can be a constant, filter, or nonlinear function, as long as the individual Q_k sum to unity across the frequency band. Further, the filters Q_k can be dynamically adjusted during operation to alter the blending scheme, or to switch certain actuators on or off in software. This enables a software-configurable, modular system that can switch from open-loop, human control to fully autonomous closed-loop target tracking (or somewhere in between) instantly, with no hardware modification necessary.

This capability comes at the price of increased demands on the actuators’ performance, however. To achieve the promise of universal haptic feedback across all units, for example, the actuators must have low friction and stiction, lest the haptic force be drowned out by the frictional forces. Further, to use Equation 11.1 to estimate the position of the slave unit—which would be beneficial given the low framerate of the MR imagery—the system is required to be stiff, so system compliance contributes minimally to error in estimating the slave’s position. These requirements are in addition to the already-numerous constraints placed on the actuators by the MR environment, so it is clear that a custom-designed actuator is needed.

Ganesh, et al modeled a hydrodynamic actuator pair and found a strong dependence of first natural frequency of the system on line length, citing the hose material as the main source of compliance in the system [GGB04]. They analyzed line lengths ranging from 1m to 14m, and reported bandwidth ranging from 50Hz in the shorter lengths to approximately 2Hz at the long end of the range. These results show that our system should render acceptable bandwidth in our target range of 1m (bedside unit) to 10m (outside the scanner room).

11.2 Fluid Network Demonstration

To demonstrate the various modes of operation of our fluid network design, a one-degree-of-freedom testbed was constructed. This setup consists of three actuators: two master units, one human-controlled unit (“Human Master”) whose position is sensed only, and a robot-controlled unit (“Robot Master”) whose position is sensed and controlled through an inner loop; and a single slave unit whose position is sensed. The three basic blending schemes discussed in Section 11.1 are demonstrated here.

Figure 11.2 shows the system in Motion Scaling mode. The positions of the three actuators are plotted, and a fourth virtual trace showing the theoretical motion of the slave unit is provided for reference. The Human Master was actuated by hand to simulate a human clinician, and it can be seen that the system accurately scales the human-controlled unit’s motion. These results are from open-loop operation—the scaling is done by the fluid network, requiring sensing of only the master units’ positions. The scale factor shown here was chosen arbitrarily, and though the system is capable of changing scale factor on-the-fly, this was not done for clarity of presentation.

The second mode of operation, Frequency Crossover, is demonstrated in Figure 11.3. In this experiment, a 2-Hz dither signal was added to the output by the Robot Master, on top of manual actuation of the Human Master unit. The unevenness of the Human Master input is due to the effect of the system haptics from the Robot Master on the operator of the Human Master unit. As in the previous experiment, this was done completely open-loop, with the slave output sensed strictly for verification purposes.

The final collaborative mode of operation to be demonstrated is the Virtual Wall. In the experiment shown in Figure 11.4, the restricted zone was set to be the region where output is greater than 2mm. For this experiment, sensing of the slave unit’s position was necessary, though the signal was not used for feedback. This strategy minimizes excursions of the slave unit into the restricted zone by nullifying all human master inputs that would drive the slave unit into the restricted zone by actuating the robot master equally and opposite.

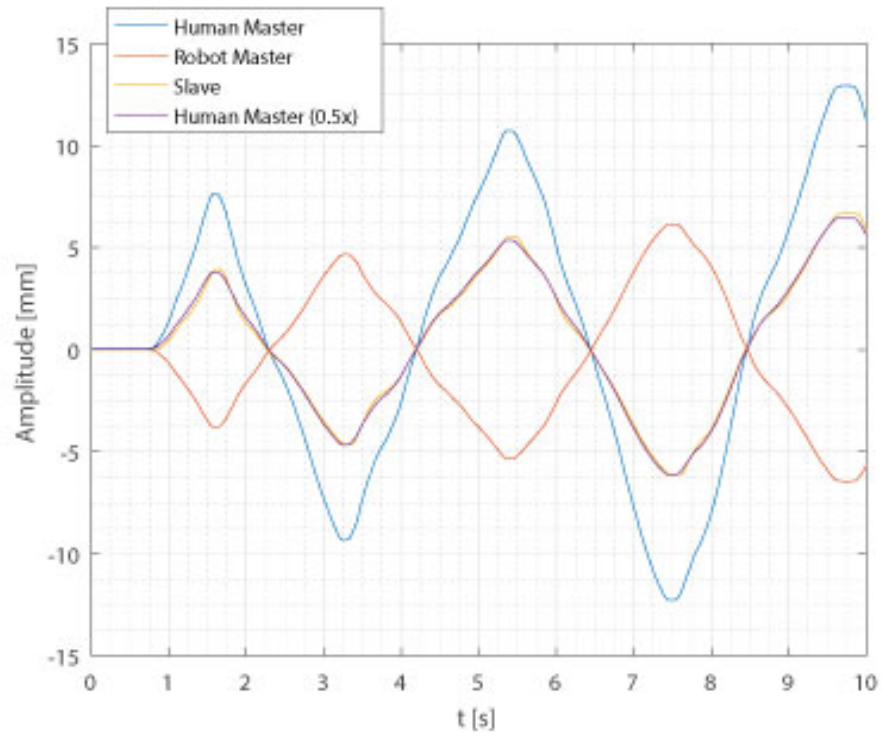


Figure 11.2: Motion Scaling Experimental Results

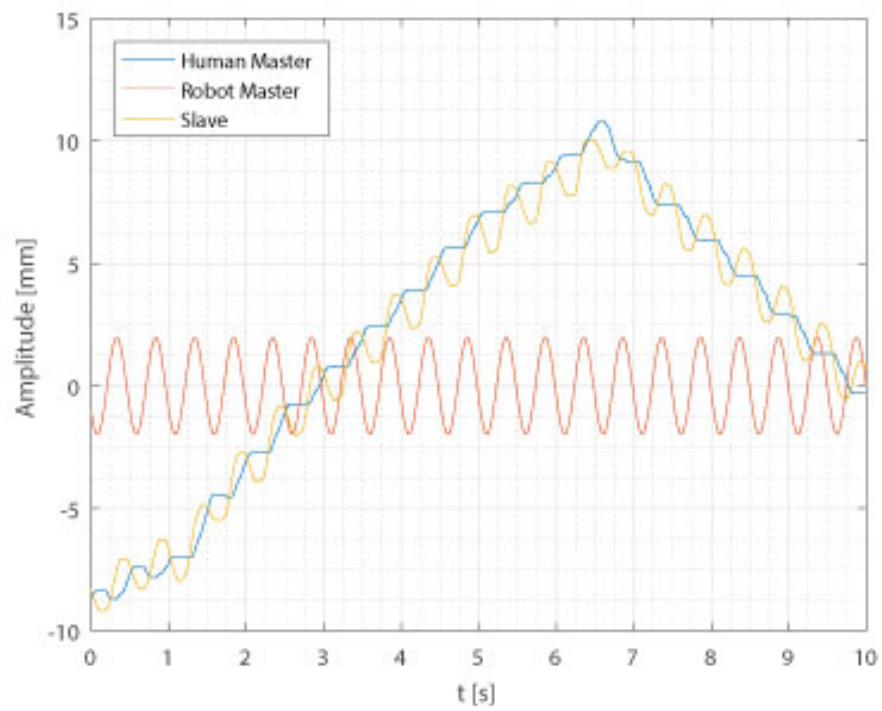


Figure 11.3: Frequency Crossover Experimental Results

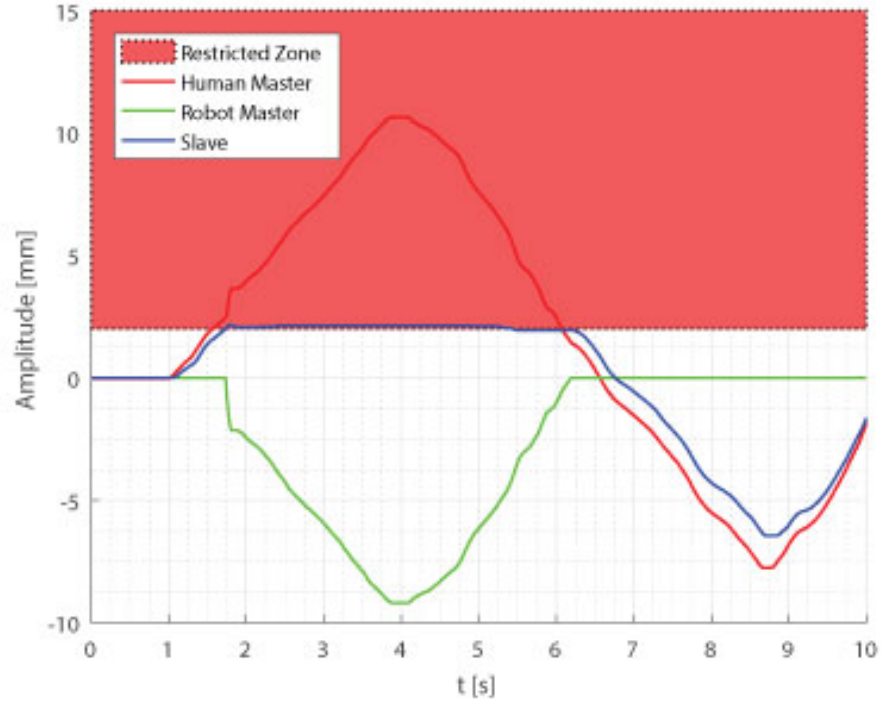


Figure 11.4: Virtual Wall Experimental Results

11.3 Fully-Autonomous Robotic Operation

In addition to co-robotic operation, fully-autonomous target tracking is also a desirable mode of operation. Using the real-time image feedback algorithm mentioned in Chapter 10, our collaborators are able to provide direct slave unit position feedback using the MR images, though with appreciable degradation of the true signal. The goal of this research is closed-loop control using this image-based feedback to autonomously drive a needle to a pre-identified target in the presence of respiratory motion; the remainder of this work is toward developing this closed-loop tracking demonstration.

The full system consists of three major subsystems: the Motion Phantom, the Robotic Manipulator, and the Scanner and image-processing infrastructure. A gelatin phantom is mounted on the Motion Phantom stage as it tracks a pre-recorded respiratory motion profile recorded from a live volunteer; this is our abdominal lesion analogue. The Robotic Manipulator is the system described herein, with the Human Master input disabled and

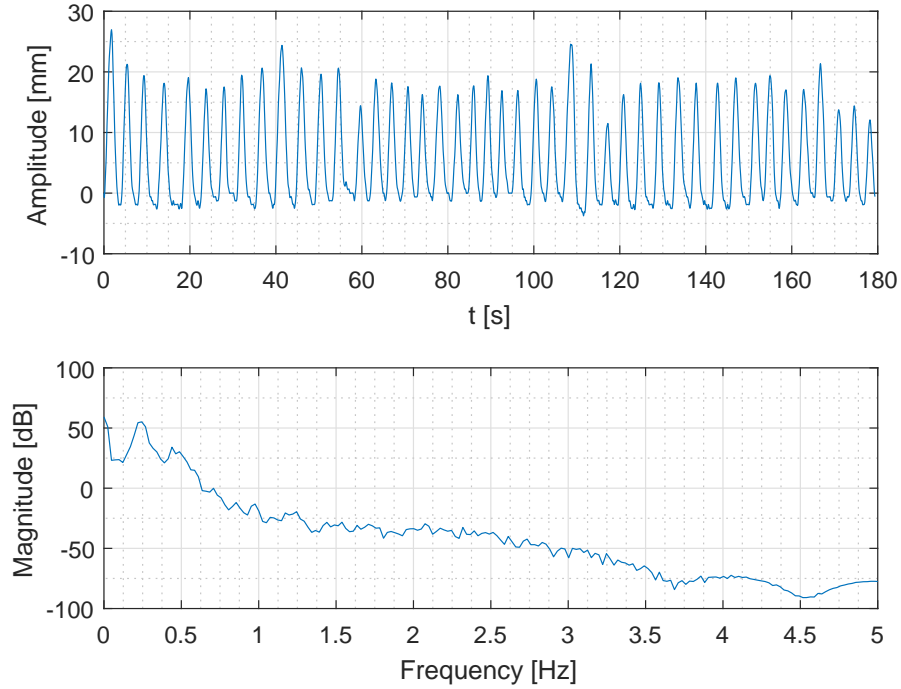


Figure 11.5: Example Recorded Breathing Trajectory

an MR-compatible biopsy needle attached to its output. The controller is implemented on a National Instruments PXI real-time target, which receives feedback data from the master-side encoders and from the image-processing algorithm through a serial link. Finally, the Scanner is a 3T MRI system (MAGNETOM Prisma, Siemens, Erlangen, Germany), connected through a custom imaging pipeline to our collaborators' image processing algorithm [LMS17, WGH13].

We will build up this system from blocks we have developed in this work; the Motion Phantom developed in Chapter 10 will be used as-is, so it only remains to design a controller that can use the MR image feedback effectively despite the limitations thereof: an appreciable delay, quantization, and low sample rate (relative to the loop rate of the inner-loop master-side controller, and to the motion profile itself).

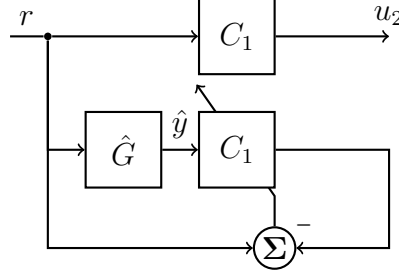


Figure 11.6: Adaptive Feed-Forward Controller Structure

11.3.1 Controller Design

An example of typical breathing motion is given in Figure 11.5. This data was recorded from a live human subject, and will serve as the reference trajectory for the tracking experiment in Section 11.3.2. This trajectory is roughly periodic, though the period is unknown *a priori* and varies breath-to-breath. Additionally, it does not have a repeatable shape that can be taken advantage of for prediction, even if the period were constant. The non-stationary reference suggests that Repetitive Control would perform poorly; this is shown in simulation by Teng, et al. [TCC12]. They propose instead an adaptive controller with feed-forward and feedback channels.

The feed-forward channel of the controller is based on Widrow’s adaptive inverse controller [WW95], and a block diagram is given in Figure 11.6. \hat{G} is the model of the pre-stabilized closed-loop plant G , C_2 is a finite impulse response (FIR) filter whose tap weights are determined by the Recursive Least Squares (RLS) algorithm to minimize the error in inverting the closed-loop model \hat{G} —model matching problem to minimize $\|(1 - F\hat{G})r\|_2$. As the adaptive controller is inverting the model of the closed-loop plant, rather than the plant itself, tracking performance will be determined by the accuracy of the model. To improve the performance when an exact model is unavailable, an adaptive feedback structure can be introduced [LT13].

The structure of the feedback controller is given in Figure 11.7. C_2 is a FIR filter, with filter weights determined using the Recursive Least Squares (RLS) algorithm to minimize $\|(1 - z^{-N_q}C_2\hat{G})x\|_2$, $x = e + xC_2Q\hat{G}$. Q is a linear-phase low-pass filter, of order N_q .


$$\min_{C_1} \|(1 - C_2 \hat{G})^{-1}(1 - C_2 \hat{G})e\|_2 \quad (11.6)$$

$$= \min_{C_1} \|e\|_2 \quad (11.7)$$

When these two channels are combined into a single controller, the structure of Figure 11.8 is created. The transfer function from reference (r), and disturbance (w) to the tracking error (e) can be shown to be

$$e = \frac{(1 - C_2 \hat{G})(1 - C_1 G)}{1 + C_2(G - \hat{G})}r - \frac{1 - C_2 \hat{G}}{1 + C_2(G - \hat{G})}w \quad (11.8)$$

93

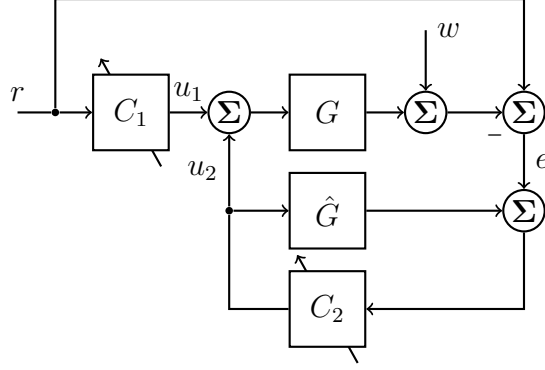


Figure 11.8: Adaptive Feedback/Feedforward Controller Structure

and reject disturbances.

11.3.2 Adaptive Controller Characterization

As the complete system poses significant challenges and is easily broken down into subsystems, testing of each subsystem was performed individually prior to full system assembly. To prove the Robotic Manipulator and adaptive control scheme, the benchtop setup from the previous section was used and the Human Master switched off. We will first study the performance of the controller under ideal conditions, then examine the effects of the three primary signal corruption sources in the MR Robotics application: quantization, delay, and low sample rate.

The experimental setup is shown in Figure 11.9, and consists of the following:

- a three-actuator setup with seven meters of tubing to replicate the run from outside the scanner room to the bore
- a laser encoder, which stands in for the MR system to provide real-time feedback
- a host PC to communicate with the real-time target and save data
- a real-time target, a National Instruments PXI chassis with a PXI-7833R multifunction data acquisition card installed. The system was sampled at 50Hz, unless otherwise specified

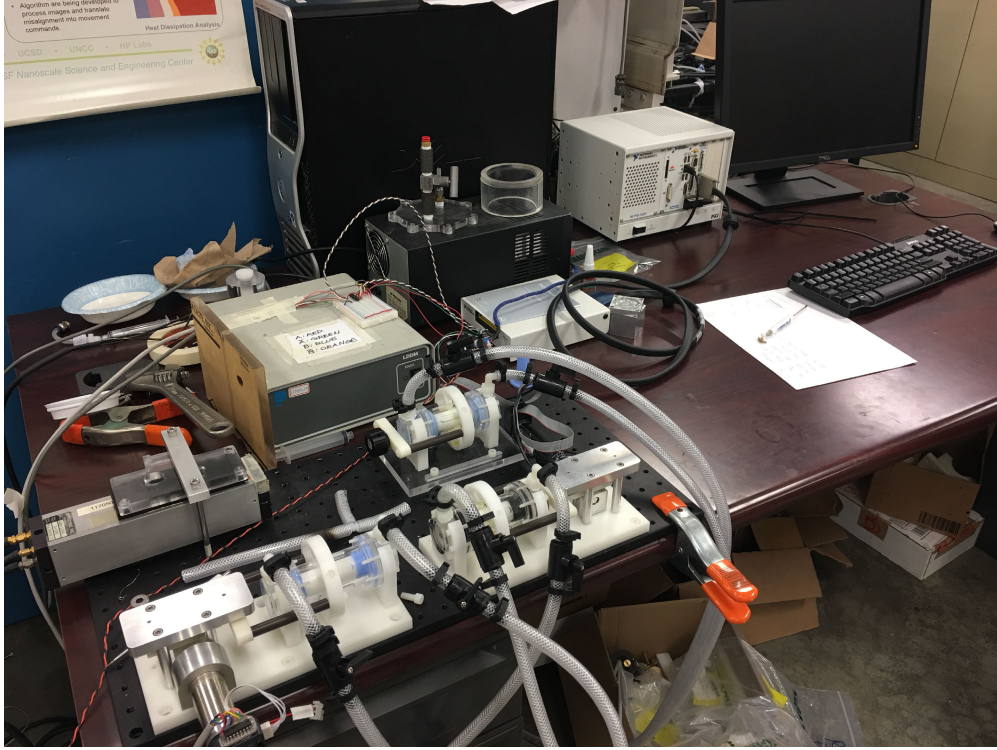


Figure 11.9: Experimental Setup, Closed-Loop Control Experiments

To identify a nominal system model, a frequency sweep from the reference to the inner-loop controller to the slave output was performed, and a discrete-time state space model was fit to the frequency response data obtained. Results from this experiment are given in Figure 11.10.

To simulate the experimental conditions, the reference for this experiment was identical to the breathing pattern tracked by the Motion Phantom. In order to decouple the control problem from the prediction and upsampling problem, perfect feedback was assumed for this section. The first set of test case experiments will study the effects of filter order on tracking performance. First, the feed-forward channel will be isolated, then the feedback channel, and finally, the combination controller will be tested. The adaptive filters implemented here are a variation on Jiang's unwindowed lattice filter [JG95] developed in the lab, but since in this work, we are only applying the filter, discussion will be limited to its performance.

The feed-forward channel reached the point of diminishing returns fastest, saturating at around order 5. For consistency, however, the feed-forward order was varied through the

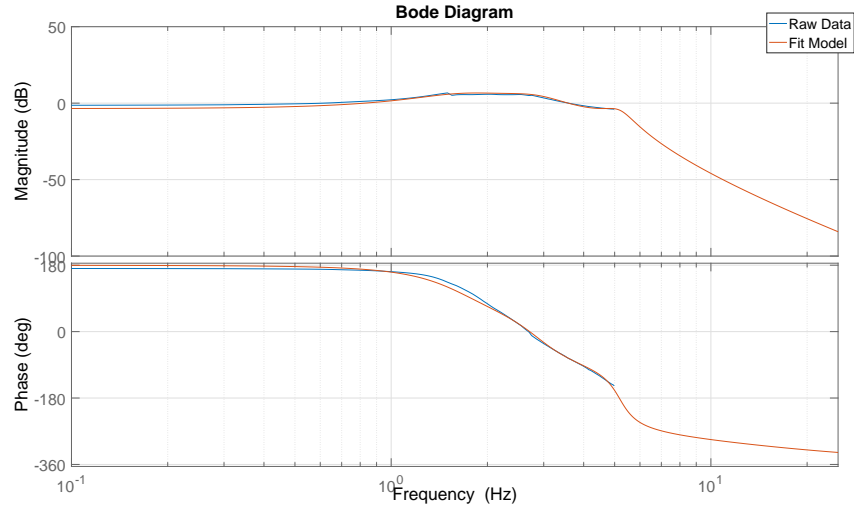


Figure 11.10: Robotic Manipulator System Identification

same range as the feedback channel, which had more interesting results at higher orders. The RMS error in tracking a reference profile is plotted against filter order in Figure 11.11, and the time trace of the run with the lowest error is given beneath.

The tracking performance is reasonably good, compared to both the feedback-only and combination results, but suffers from the common feed-forward issue with disturbance rejection. It is not uncommon to observe a noticeable DC error in the feed-forward only tracking results, as a result of system stiction or other disturbances. If this issue manifests itself on the benchtop, where control over the experimental setup and external disturbances should be at a maximum, feed-forward control alone is unsuited for the interventional environment.

The feedback channel is more interesting. While it is functional at a filter order of 5, maximum performance does not occur until somewhere between 20 and 30. Full results for this experiment are given in Figure 11.12, in a very similar fashion to the previous experiment. The discrepancy between the optimal order for the feedback and feed-forward channels is attributable to the fact that the feedback channel is operating on the mismatch between the nominal model \hat{G} and the actual plant, unlike the feed-forward channel which only sees \hat{G} . The Q filter is added to the feedback channel to limit high-frequency output of the filter, and for the purposes of this experiment was kept as a constant, linear-phase

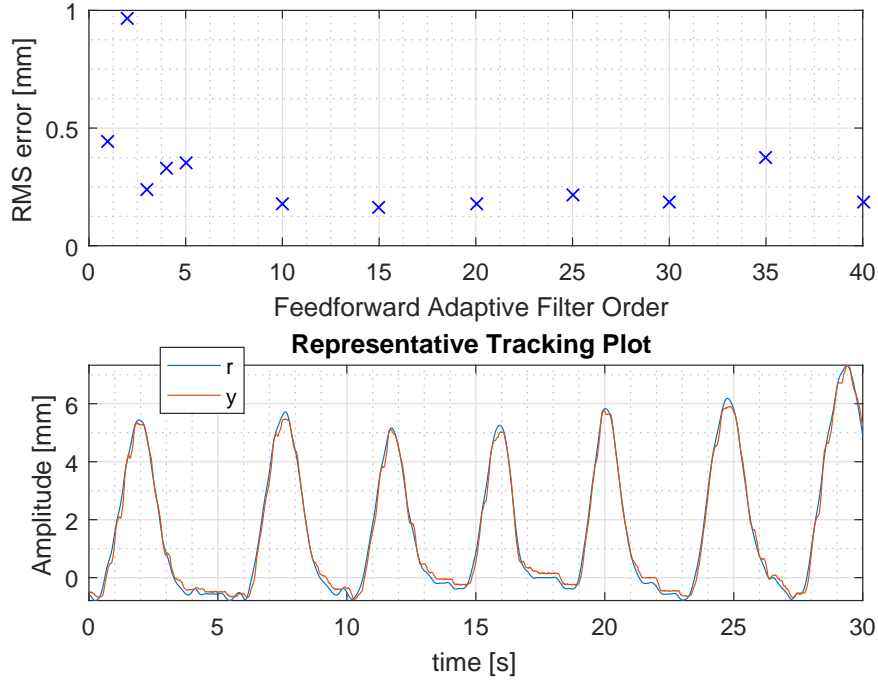


Figure 11.11: Effect of Filter Order on Feedforward Controller Performance

low-pass filter of order 10 (eq: 11.9, $N_q = 10$). The phase delay created by making this filter causal for implementation is compensated with a delay on the regressor side of the adaptive filter C_2 (see Figure 11.7).

Unlike the feed-forward channel, the feedback channel has shown an ability to overfit the data at higher orders, meaning there is a performance penalty (in addition to the computation penalty) for choosing a high order arbitrarily. While the feedback channel counters disturbances better than the feed-forward channel, it amplifies error at certain frequencies too close to the desired reference's spectrum to effectively attenuate with the Q filter.

$$Q = \left(\frac{z^{-1} + 2 + z}{4} \right)^{N_q} \quad (11.9)$$

The combination approach allows the two channels to work to each channel's strengths while allowing the other to compensate for weaknesses. The feed-forward channel has been shown to be weak with disturbances, but strong in tracking the higher-frequency components of the reference trajectory while avoiding any amplification of other signals. The feedback

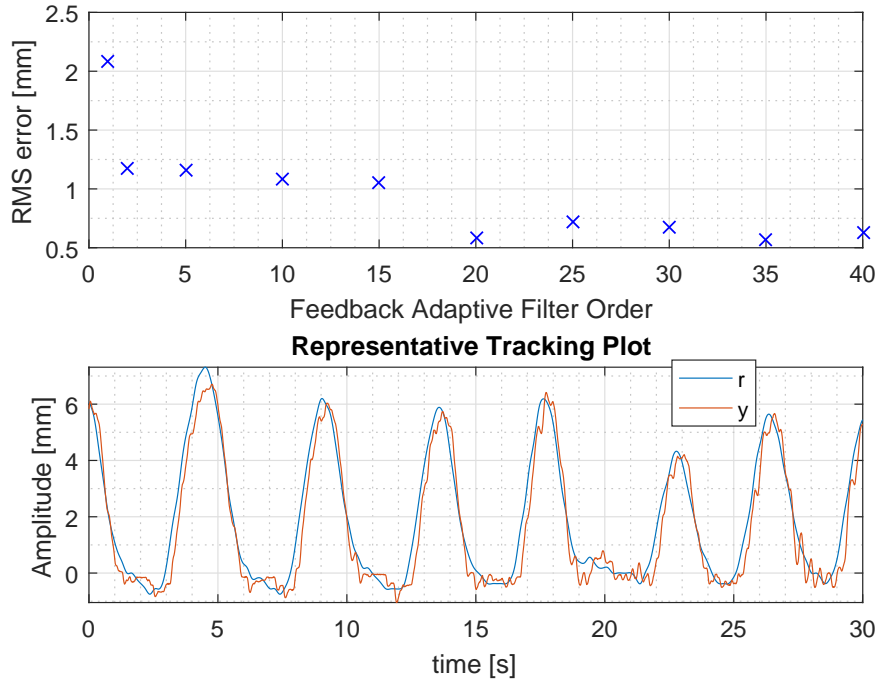


Figure 11.12: Effect of Filter Order on Feedback Controller Performance

channel, on the other hand, is strong at disturbance rejection, but suffers from amplification in the high frequency region. Combining these two controllers will allow the feedback channel to reject low-frequency disturbance and correct minor errors while the feed-forward channel does the bulk of the tracking. To do this, the Q filter of Equation 11.9 was replaced with a linear-phase FIR filter designed with a cutoff much lower than one could design if the feedback channel were solely responsible for tracking. The combination controller was then set, and the order of the two adaptive filters varied in tandem through a large range. Results from this experiment are given in Figure 11.13, and show that the optimal order for the combination controller on this system is between 30 and 40. It can also be seen that the combination controller can suffer from overfitting at higher orders.

With the filter order effects studied, an order of 30 for both filters was chosen. While this is high for the feed-forward channel, it is justified for two reasons: this controller has not been shown to suffer from excessive order, and intuition with the system suggests that while the higher order will not be helpful with clean signals, it will become more so when the

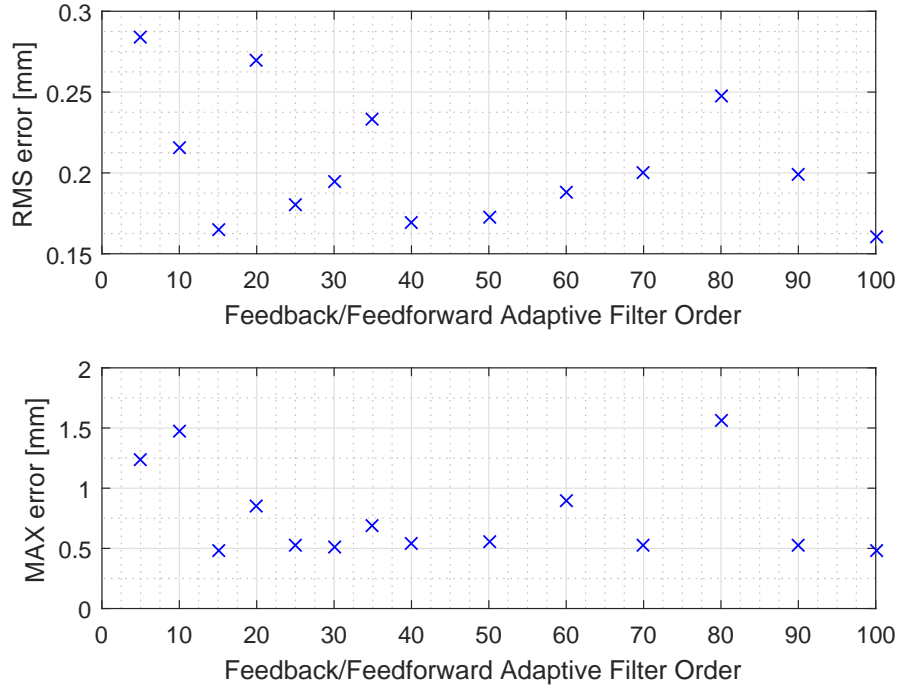


Figure 11.13: Effect of Filter Order on Combined Controller Performance

feedback and reference signals are corrupted in the next section. As shown in Figure 11.14, the system is capable of tracking the respiratory motion profile with an RMS error of approximately 150 μ m with the combination controller. To drive home the gains of the combination controller, Figure 11.15 gives an error spectrum comparing the feed-forward-only adaptive controller with the combination feed-forward/feed-back controller; the spectrum of the reference trajectory is plotted as well for convenience. Over the band where the reference trajectory has greatest power, the combination controller reduces error by approximately 60dB. It can be seen that the combination controller is not superior across the full band pictured, but achieves the greatest error reduction in the 0-1Hz band where the reference trajectory is strongest.

11.3.2.1 Effects of Signal Corruption on Adaptive Controller Performance

Now that the performance of the controller under ideal circumstances has been characterized, we will begin to examine the effects of the various imperfections in the feedback signal

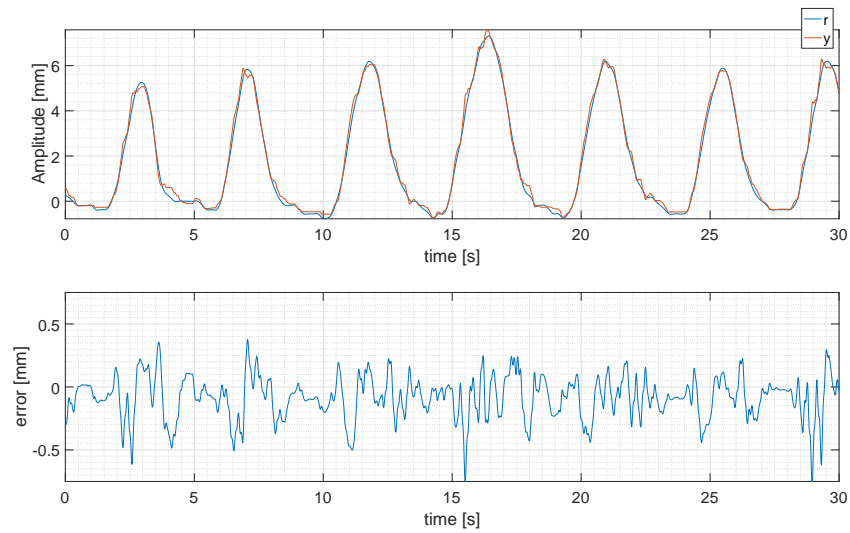


Figure 11.14: Benchtop Tracking Results

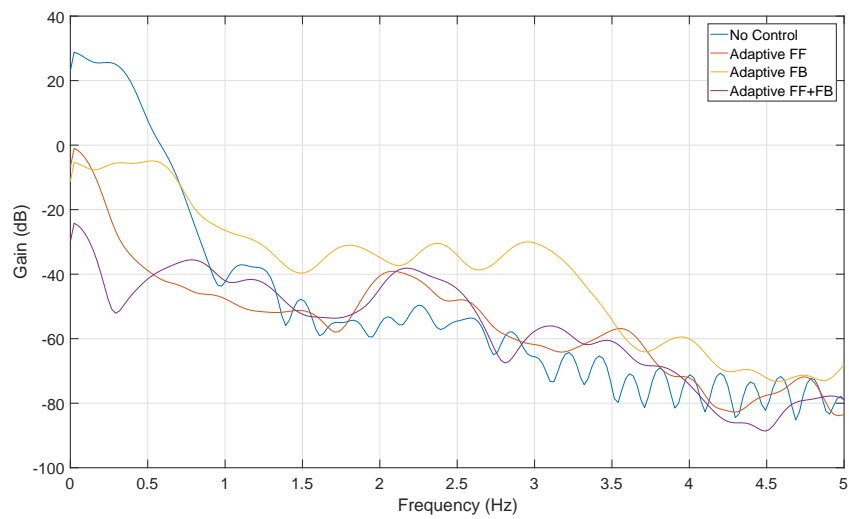


Figure 11.15: Benchtop Tracking Error Spectrum

introduced by the real-time image feedback algorithm. Without getting too deep into the workings of our collaborators' algorithm, we will explain on a high level its function. The MR data (still in frequency domain) is obtained from the scanner and processed into a set of 2D images. This data transfer and processing takes time, which introduces a delay to the signal. After an image is obtained, a region of interest (ROI) is gridded at a specified spacial resolution and objects in the ROI are tracked on this grid. This coarse gridding introduces a quantization to the signal. This tracking requires computation time, which limits the temporal resolution (sampling rate) achievable in real-time. It is possible to trade quantization for sampling rate, but without changes to the imaging pipeline, the acquisition delay is fixed. At time of writing, the values of these three parameters are thus: 800ms delay, 2-3mm quantization, and 2Hz sample rate.

These three values will serve as the starting point for a survey of the effects of various values of each on the tracking performance of the adaptive controller. To perform experiments for this survey, a hardware-in-the-loop (HIL) setup was constructed to be capable of emulating the feedback signal at various levels of corruption. The hardware setup is identical to the previous section, but we are capable of corrupting the output of the laser encoder to better emulate the feedback available from the image processing algorithm, or to isolate each parameter to study its effects independently. For the target-tracking application, both the target position (reference) and needle position (output) would be obtained from the image processing algorithm, so the feedback emulation was performed on both the output of the slave unit and a nominal respiratory motion profile from Chapter 10 which served as the reference for this experiment. The nominal sample rate for both the inner-loop master-side controller and the outer-loop adaptive controller is 50Hz, unless otherwise specified, and in all three studies, perfect feedback was included as a case for reference. In all cases, the uncorrupted reference and output were recorded and used to calculate the “real” error.

The first parameter of interest was quantization, which was varied from perfect feedback (0mm) to 3.5mm. This bound was chosen because many lesions are under 5mm in length, so decreasing spatial resolution beyond that would render the application moot. As expected, greater quantization leads to greater error, but since at the larger quantizer values, small

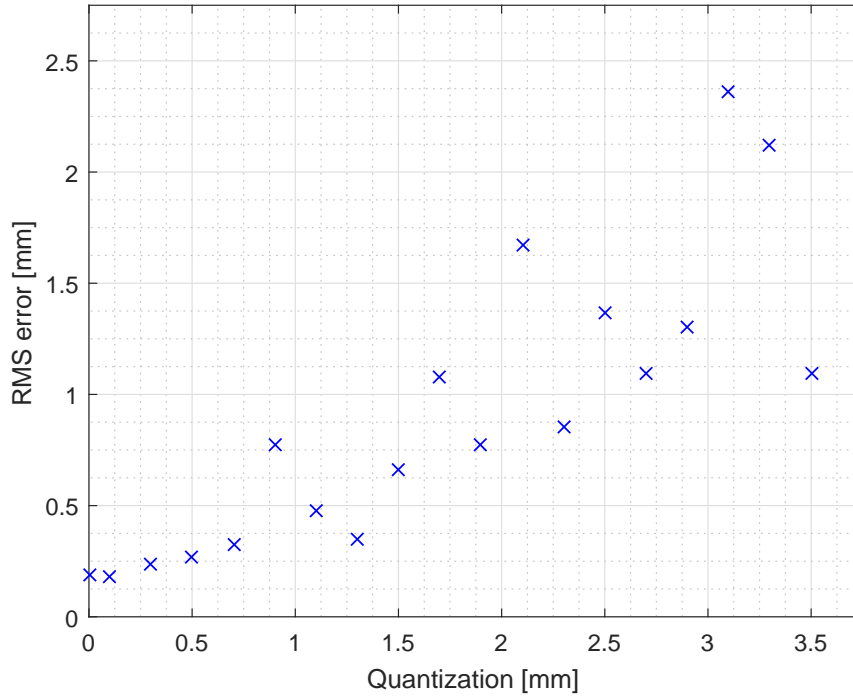


Figure 11.16: Benchtop Experiment Summary: Quantization

errors can be magnified, this also leads to greater variance run-to-run when the quantization value begins to exceed the RMS error. At the current amount of quantization in the real-world system, the adaptive controller gives just over 0.75mm RMS error, which is roughly five times worse than perfect feedback. Full results are given in Figure 11.16.

The next parameter to study was delay. To implement this, for each value, the plant model \hat{G} was updated to reflect the new system delay. All other parameters were held constant through the tests. At first, performance is relatively unaffected, reaching approximately 0.75mm RMS error at 15 delays (at 50Hz). However, after this point, the trend steepens, and by 25 delays, we are already past 2mm RMS, which is unacceptable performance. The 800ms delay in the nominal feedback system corresponds to 40 delays, at which point the performance is too poor to report. We conclude from this study that this controller needs either an improvement in the feedback system or an external predictor to (even partially) compensate the large plant delay. Full results are given in Figure 11.17.

The final parameter of interest was sampling rate. In the HIL setup, the variations in

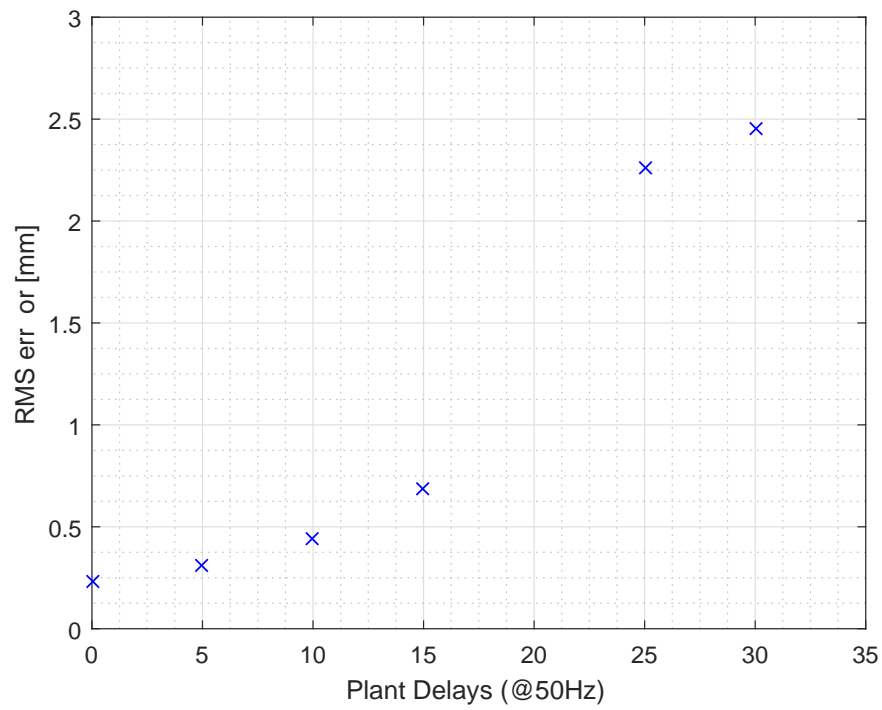


Figure 11.17: Benchtop Experiment Summary: Delay

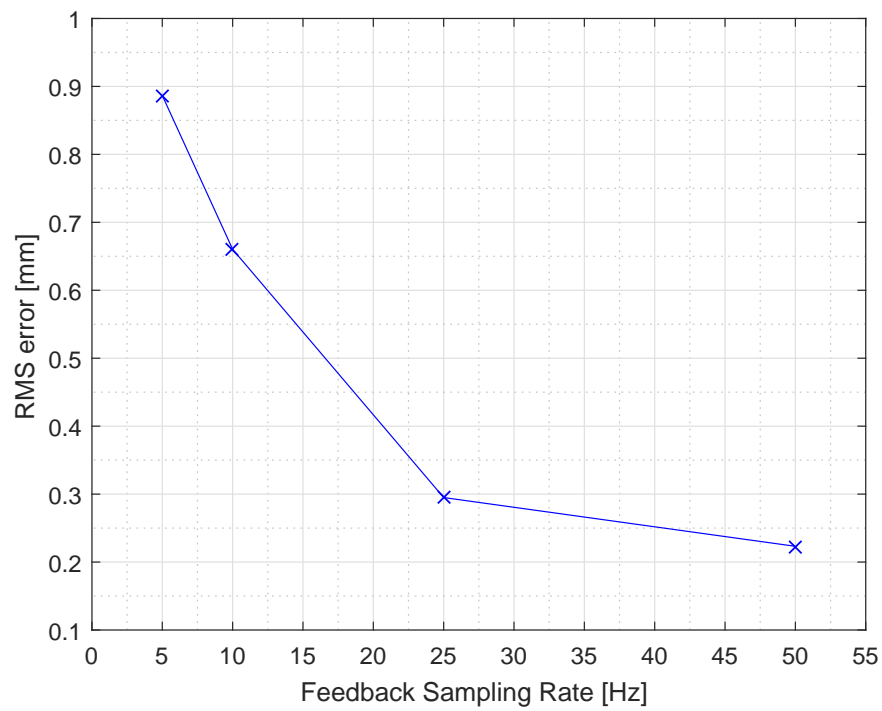


Figure 11.18: Benchtop Experiment Summary: Sampling Rate

sampling rate were implemented as a frequency divider, so the number of points is small as only factors of the base sampling rate (50Hz) could be tested. This was also a special case in that whereas in the other cases, the adaptive filter was run at the same sampling rate as the inner-loop controller, in this case, it was run at whatever sampling rate was being tested at the time and its output held at 50Hz for the inner-loop controller. The plant model \hat{G} and the low-pass filter Q were converted to the current sample rate in each case, but were in no other way modified from trial to trial. The results in Figure 11.18 show acceptable performance through 10Hz, but beyond that, the performance quickly degrades. While 2Hz was a possible rate for testing, the controller did not perform adequately and was thus not reported. We conclude that 2Hz is insufficient sample rate for this controller to perform properly, so either the feedback must be improved, or an external upsampler must be designed.

CHAPTER 12

Conclusions and Recommendations

In this research, we have developed techniques and tooling to create custom, fabric-reinforced injection-molded parts. We have quantified the performance of our custom parts and verified the necessity of the fabric reinforcement process to proper performance in our application. Common failure modes and design and manufacturing flaws in the process have been identified, and the design iterated to minimize the occurrence of these failures, leading to a fairly robust rapid prototyping-quality rolling diaphragm that has been serviceable in the pursuit and optimization of our diaphragm actuators. Further testing and optimization has shown the in-house rolling diaphragm to be superior to the commercial version in the transmission of haptic feedback.

We have developed a family of linear hydrostatic actuators, both single- and double-acting, and quantified the performance of each successive generation. We have developed a half-inch stroke single-acting actuator, a one-inch stroke single-acting actuator, and two generations of one-inch stroke, double-acting actuators. We have shown that the next-generation double-acting device has many desirable properties, including one-to-one correspondence between input and output actuators— so extrapolation of slave position from master position is feasible, and good force transmission and haptic feedback capability— so the force felt at the needle tip can be interpreted and used by either the robotic system or its human operator. We have shown that the next-generation actuator system has negligible hysteresis and estimated the transport delay from the hydraulic lines for one line length.

We have then integrated these actuators into an MR-compatible robotic system (“Motion Phantom”) to emulate respiratory motion, and begun work on a robotic system based on these actuators to position and drive a biopsy needle. The Motion Phantom device has

been shown to emulate the desired motion with acceptable error to be considered “truth data” for the development and furtherance of MR image processing algorithms. Toward the development of a closed-loop robotic system for needle placement and driving, a 1DOF test setup was constructed and an adaptive controller designed, implemented, and studied.

From the results of this study, the following recommendations can be made going forward:

1. In the absence of improvement in the processing time, the controller would benefit immensely from an accurate external predictor to compensate for some or all of the plant delay; the adaptive controller does have some prediction capability, but performance suffers before reaching the current nominal delay of the system.
2. Some effort could be invested in improving the quantization of the image feedback algorithm, but of the three corruption parameters, the adaptive controller handles this the best. It may be worthwhile to trade some quantization for higher sample rate in the next iteration of the image processing algorithm.
3. The feedback sampling rate must be improved, be it by improvement of the image processing algorithm, or by the addition of an upsampling scheme to the predictor mentioned earlier, but benchtop testing has shown a practical minimum of between 10 and 25Hz for acceptable performance.

REFERENCES

- [ADB00] H.J.M.T.S. Adriaens, W. De Koning, and R. Banning. “Modeling piezoelectric actuators.” *Mechatronics, IEEE/ASME Transactions on*, **5**(4):331–341, 2000.
- [BTA06a] Douglas A Bristow, Marina Tharayil, and Andrew G Alleyne. “A survey of iterative learning control.” *Control Systems, IEEE*, **26**(3):96–114, 2006.
- [BTA06b] Douglas A Bristow, Marina Tharayil, and Andrew G Alleyne. “A survey of iterative learning control.” *IEEE Control Systems*, **26**(3):96–114, 2006.
- [BZJ08] Ivan Bricault, Nabil Zemiti, Emilie Jouniaux, Céline Fouard, Elise Taillant, Frédéric Dorandeu, and Philippe Cinquin. “Light puncture robot for CT and MRI interventions.” *IEEE Engineering in Medicine and Biology Magazine*, **27**(3):42–50, 2008.
- [CCW11] Jing Cai, Zheng Chang, Zhiheng Wang, William Paul Segars, and Fang-Fang Yin. “Four-dimensional magnetic resonance imaging (4D-MRI) using image-based respiratory surrogate: A feasibility study.” *Medical physics*, **38**(12):6384–6394, 2011.
- [CK03] Marc Crudele and Thomas R Kurfess. “Implementation of a fast tool servo with repetitive control for diamond turning.” *Mechatronics*, **13**(3):243–257, 2003.
- [CMS99] James F Cuttino, Arthur C Miller Jr, and Dale E Schinstock. “Performance optimization of a fast tool servo for single-point diamond turning machines.” *Mechatronics, IEEE/ASME Transactions on*, **4**(2):169–179, 1999.
- [Com16] “Computerized Imaging Reference Systems Inc.” <http://www.cirsinc.com/>, 2016.
- [Cse03] Tibor Cselle. “Piezoelectric adjusting mechanism.”, July 1 2003. US Patent 6,586,862.
- [CT16] Cheng-Wei Chen and Tsu-Chin Tsao. “Data-based feedforward controller reconstruction from iterative learning control algorithm.” In *Advanced Intelligent Mechatronics (AIM), 2016 IEEE International Conference on*, pp. 683–688. IEEE, 2016.
- [DBP96] Maria Drangova, Brett Bowman, and Norbert J Pelc. “Physiologic motion phantom for MRI applications.” *Journal of Magnetic Resonance Imaging*, **6**(3):513–518, 1996.
- [Di 82] Mario Di Giovanni. *Flat and corrugated diaphragm design handbook*, volume 11. CRC Press, 1982.

- [ETH08] Haytham Elhawary, Zion Tsz Ho Tse, Abbi Hamed, Marc Rea, Brian L Davies, and Michael U Lamperth. “The case for MR-compatible robotics: a review of the state of the art.” *The international journal of medical robotics and computer assisted surgery*, **4**(2):105–113, 2008.
- [EZR08] Haytham Elhawary, Aleksandar Zivanovic, Marc Rea, Brian L Davies, Collin Besant, I Young, and MU Lamperth. “A modular approach to MRI-compatible robotics.” *IEEE Engineering in medicine and biology magazine*, **27**(3):35–41, 2008.
- [GGB04] G Ganesh, Roger Gassert, Etienne Burdet, and Hannes Bleuler. “Dynamics and control of an MRI compatible master-slave system with hydrostatic transmission.” In *Robotics and Automation, 2004. Proceedings. ICRA’04. 2004 IEEE International Conference on*, volume 2, pp. 1288–1294. IEEE, 2004.
- [GMB06] Roger Gassert, Roland Moser, Etienne Burdet, and Hannes Bleuler. “MRI/fMRI-compatible robotic system with force feedback for interaction with human motion.” *IEEE/ASME transactions on mechatronics*, **11**(2):216–224, 2006.
- [GOR09] Ed Gullans, Erica Ollinick, Scott Rein, Christopher Saffos, Jay Shilling, Karen Chang Yan, James J Pilla, and Chun Xu. “Design of a dynamic heart phantom for magnetic resonance imaging.” In *2009 IEEE 35th Annual Northeast Bioengineering Conference*, pp. 1–2. IEEE, 2009.
- [GYC06] Roger Gassert, Akio Yamamoto, Dominique Chapuis, Ludovic Dovat, Hannes Bleuler, and Etienne Burdet. “Actuation methods for applications in MR environments.” *Concepts in Magnetic Resonance Part B: Magnetic Resonance Engineering*, **29**(4):191–209, 2006.
- [Hid95] Laszlo M Hideg. “Time delays in iterative learning control schemes.” In *Intelligent Control, 1995., Proceedings of the 1995 IEEE International Symposium on*, pp. 215–220. IEEE, 1995.
- [Hid96] Laszlo M Hideg. “Stability and convergence issues in iterative learning control. II.” In *Intelligent Control, 1996., Proceedings of the 1996 IEEE International Symposium on*, pp. 480–485. IEEE, 1996.
- [JG95] Shyh-Biau Jiang and S Gibson. “An unwindowed multichannel lattice filter with orthogonal channels.” *IEEE Transactions on Signal Processing*, **43**(12):2831–2842, 1995.
- [KGM15] Elena A Kaye, Kristin L Granlund, Elizabeth A Morris, Majid Maybody, and Stephen B Solomon. “Closed-Bore Interventional MRI: Percutaneous Biopsies and Ablations.” *American Journal of Roentgenology*, **205**(4):W400–W410, 2015.
- [KLP10] Samantha Kee, Eric Larsen, Kamila Paluch, Ryan Sinke, Karen Chang Yan, James J Pilla, and Chun Xu. “Development of a dynamic heart phantom prototype for Magnetic Resonance Imaging.” In *Proceedings of the 2010 IEEE 36th Annual Northeast Bioengineering Conference (NEBEC)*, pp. 1–2. IEEE, 2010.

- [KSC13] Axel Krieger, Sang-Eun Song, Nathan Bongjoon Cho, Iulian I Iordachita, Peter Guion, Gabor Fichtinger, and Louis L Whitcomb. “Development and evaluation of an actuated MRI-compatible robotic system for MRI-guided prostate intervention.” *IEEE/ASME Transactions on Mechatronics*, **18**(1):273–284, 2013.
- [LMS17] Xinzhou Li, Samantha Mikael, James Simonelli, Tsu-Chin Lee, Yu-Hsiu and Tsao, and Holden H. Wu. “Real-Time Motion Prediction for Feedback Control of MRI-Guided Interventions.” In *International Society for Magnetic Resonance in Medicine*, 2017.
- [LT13] Chi-Ying Lin and Tsu-Chin Tsao. “Adaptive Control With Internal Model for High-Performance Precision Motion Control and Its Application to a Fast-Acting Piezoelectric Actuator.” *Journal of Dynamic Systems, Measurement, and Control*, **135**(6):061012, 2013.
- [MGR08] Andreas Melzer, Bernd Gutmann, Thomas Remmele, Renate Wolf, Andreas Lukoscheck, Michael Bock, Hubert Bardenheuer, and Harald Fischer. “In-motion for percutaneous image-guided interventions.” *IEEE Engineering in Medicine and Biology Magazine*, **27**(3):66–73, 2008.
- [Mod16] “Modus Medical Devices Inc.” <http://modusqa.com/>, 2016.
- [MYR15] Samantha Mikael, Rashid Yasin, Samuel Ross, MW Wahi-Anwar, James Simonelli, David Lu, Kyung Sung, Tsu-Chin Tsao, and Holden Wu. “Imaging Assessment and Feasibility of a Hydrostatically Actuated Robotic System for Real-Time MRI-Guided Interventions.” In *International Society for Magnetic Resonance in Medicine*, 2015.
- [RCS16] Sandeep Rai, Grant Cavalier, James Simonelli, and Tsu-Chin Tsao. “MIMO Repetitive Control of an Active Magnetic Bearing Spindle.” *IFAC-PapersOnLine*, **49**(21):192–199, 2016.
- [She16] “Shelly Medical Imaging Technologies.” <http://http://www.simutec.com/>, 2016.
- [SHY10] Nicholas von Sternberg, Yousef Hedayati, Erol Yeniaras, Eftychios Christoforou, and Nikolaos V Tsekos. “Design of an actuated phantom to mimic the motion of cardiac landmarks for the study of image-guided intracardiac interventions.” In *Robotics and Biomimetics (ROBIO)*, 2010 *IEEE International Conference on*, pp. 856–861. IEEE, 2010.
- [SHZ12] Nicholas C von Sternberg, Yousef S Hedayati, Habib M Zaid, Erol Yeniaras, Eftychios Christoforou, and Nikolaos V Tsekos. “An actuated phantom for developing and studying MRI-guided interventions in dynamic environments.” In *2012 4th IEEE RAS & EMBS International Conference on Biomedical Robotics and Biomechatronics (BioRob)*, pp. 1669–1674. IEEE, 2012.

- [SPP07] Dan Stoianovici, Alexandru Patriciu, Doru Petrisor, Dumitru Mazilu, and Louis Kavoussi. “A new type of motor: pneumatic step motor.” *IEEE/ASME Transactions On Mechatronics*, **12**(1):98–106, 2007.
- [SZC11] Hao Su, Michael Zervas, Gregory A Cole, Cosme Furlong, and Gregory S Fischer. “Real-time MRI-guided needle placement robot with integrated fiber optic force sensing.” In *Robotics and Automation (ICRA), 2011 IEEE International Conference on*, pp. 1583–1588. IEEE, 2011.
- [TCC12] Kuo-Tai Teng, Kai-Hsiang Chang, Yung-Yaw Chen, and Tsu-Chin Tsao. “Respiration induced liver motion tracking control for high intensity focused ultrasound treatment.” In *2012 IEEE/ASME International Conference on Advanced Intelligent Mechatronics (AIM)*, pp. 57–62. IEEE, 2012.
- [TCO08] Nikolaos V Tsekos, Eftychios Christoforou, and Alpay Ozcan. “A general-purpose MR-compatible robotic system.” *IEEE Engineering in Medicine and Biology magazine*, **27**(3):51–58, 2008.
- [TL07] David L Trumper and Xiaodong Lu. “Fast tool servos: advances in precision, acceleration, and bandwidth.” In *Towards Synthesis of Micro-/Nano-systems*, pp. 11–19. Springer, 2007.
- [Tom87] Masayoshi Tomizuka. “Zero phase error tracking algorithm for digital control.” *Journal of Dynamic Systems, Measurement, and Control*, **109**(1):65–68, 1987.
- [TOM94] Hisataka Tanaka, Fumio Obata, Tomio Matsubara, and Hiroshi Mizumoto. “Active chatter suppression of slender boring bar using piezoelectric actuators.” *JSME international journal. Ser. C, Dynamics, control, robotics, design and manufacturing*, **37**(3):601–606, 1994.
- [TTC89] Masayoshi Tomizuka, Tsu-Chin Tsao, and Kok-Kia Chew. “Analysis and synthesis of discrete-time repetitive controllers.” *Journal of Dynamic Systems, Measurement, and Control*, **111**(3):353–358, 1989.
- [WGB14] John P Whitney, Matthew F Glisson, Eric L Brockmeyer, and Jessica K Hodgins. “A low-friction passive fluid transmission and fluid-tendon soft actuator.” In *Intelligent Robots and Systems (IROS 2014), 2014 IEEE/RSJ International Conference on*, pp. 2801–2808. IEEE, 2014.
- [WGH13] Holden H Wu, Paul T Gurney, Bob S Hu, Dwight G Nishimura, and Michael V McConnell. “Free-breathing multiphase whole-heart coronary MR angiography using image-based navigators and three-dimensional cones imaging.” *Magnetic resonance in medicine*, **69**(4):1083–1093, 2013.
- [WN08] Adrian Wills and Brett Ninness. “On gradient-based search for multivariable system estimates.” *Automatic Control, IEEE Transactions on*, **53**(1):298–306, 2008.

- [WW95] Bernard Widrow and Eugene Walach. *Adaptive Inverse Control*. Prentice-Hall, Upper Saddle River, NJ, 1995.
- [XXL05] Jian-Xin Xu, Jing Xu, and Tong Heng Lee. “Iterative learning control for systems with input deadzone.” *IEEE transactions on automatic control*, **50**(9):1455–1459, 2005.
- [Yas14] Rashid Muhammed Yasin. “*Design, Modeling, and Control of a Hydrostatic Actuator for MRI*.”. Master’s thesis, University of California, Los Angeles, 2014.
- [YHB08] Ningbo Yu, Christoph Hollnagel, Armin Blickenstorfer, Spyros S Kollias, and Robert Riener. “Comparison of MRI-compatible mechatronic systems with hydrodynamic and pneumatic actuation.” *IEEE/ASME transactions on mechatronics*, **13**(3):268–277, 2008.
- [YMS14] Rashid Yasin, Samantha Mikaiel, Kyung Sung, David Lu, Holden Wu, and Tsu-Chin Tsao. “A Hydrostatically Actuated Robotic System for Real-time MRI-guided Interventions.” In *Interventional MRI Symposium*, 2014.
- [YTM11] Bo Yang, U-Xuan Tan, Alan B McMillan, Rao Gullapalli, and Jaydev P Desai. “Design and control of a 1-DOF MRI-compatible pneumatically actuated robot with long transmission lines.” *IEEE/ASME transactions on mechatronics*, **16**(6):1040–1048, 2011.